Species Chemistry and Electrochemical Separation in Molten Fluoride Salt

Yafei Wang

Dissertation submitted to the faculty of the Virginia Polytechnic Institute and State University in partial fulfillment of the requirements for the degree of

Doctor of Philosophy
In
Nuclear Engineering

Jinsuo Zhang, Chair
Mark Pierson
Yang Liu
Xianming Bai

Aug 8th, 2019
Blacksburg, VA

Keywords: FHR; electrochemical separation; bismuth; thermodynamic properties; fission products; MOOSE

Species Chemistry and Electrochemical Separation in Molten Fluoride Salt

Yafei Wang

ABSTRACT

Fluoride salt-cooled high-temperature reactor (FHR) is a safer and potentially less expensive alternative to light water reactor due to the low pressure of primary system, passive decay heat cooling system, chemically inert coolant salt, and high-temperature power cycle. However, one challenge presented by this reactor is that fission products may leak into the primary system from its TRISO particle fuel during normal operation. Consequently, the circulating fission products within the primary coolant would be a potential radioactive source. On the other hand, the containment material of the molten salt such as nickel-based alloys may be corroded, and its species may stay in the salt. Thus, the installment of the primary coolant clean-up system and the study on the contaminant species' chemistry and separation are necessarily needed.

Electrochemical separation technique has been proposed as the online coolant clean-up method for FHR for removing some impurities from the salt such as lanthanides and corrosion products. The present research focuses on the electrochemical separations of fission products and corrosion products in molten FLiNaK salt (46.5LiF-11.5NaF-42KF mol%) which is the surrogate of the primary coolant candidate FLiBe (67LiF-33BeF_2, mol%) for FHR. The main objective is to investigate the electrochemical behaviors of fission products and corrosion products in molten FLiNaK salt to achieve its separations, and provide fundamental properties to instruct the conditions needed to be applied for a desired electrochemical separation.

La and Ce are two main elements concerned in this study since they are major lanthanide fission products. Electrochemical behavior of LaF_3 in molten FLiNaK salt was studied on both W and Mo inert working electrodes. Although the standard reduction potential of La (III) is more cathodic than that of the primary salt melt constituents K (I) and Na (I), the electrochemical separation of La from molten FLiNaK salt was achieved by merely using inert working electrode because of the formed LaF_6^{3-} when KF or NaF exists as the salt constituents. Fundamental properties of La in molten FLiNaK salt were also studied at various situations by electroanalytical methods including cyclic voltammetry (CV), chronopotentiometry (CP), and potentiodynamic polarization scan (PS). Ce is another fission product to be separated out from molten FLiNaK salt. Both inert (W) and reactive working electrodes (Cu and Ni) were utilized to realize the extraction of Ce. The electrochemical behaviors of Ce observed on inert W electrode are similar to the ones obtained in FLiNaK-LaF_3 system. Reactive electrodes Cu and Ni were used to precede the electrochemical deposition potential of Ce by forming intermetallic compounds. It turned out only Ni electrode was feasible for preceding the deposition potential and the intermetallic compound was identified as $CeNi_5$.

The dissolution of chromium metal in the form of chromium fluoride into molten FLiNaK salt is the main concern of alloy corrosion in FHR. To understand the alloy corrosion and removal of the corrosion products from the FHR salt coolant, the electrochemical behavior

and fundamental properties of Cr in molten FLiNaK salt were investigated in the present study as well. A new analysis method for the Cr two-step electrochemical reaction in the salt was developed. The method can be applied to other two-step reactions as well.

Liquid bismuth was proposed to be the extraction media for liquid/liquid multistage separation of fission products in molten salt reactor. It also can be used as the cathode to extract the fission product of which the electrodeposition potential is close to or more negative than that of the main constituents of molten salt. Activity and activity coefficient are essential factors for assessing the extraction behavior and viability of bismuth in separating fission products. Hence, in the present study, the activity and activity coefficient of fission products and alkali metals (Li and K) at different concentrations and temperatures were determined by experiment and simulation methods respectively.

To conduct the parametric study for the electrochemical reaction process and predict fundamental properties, an electrochemical model including single-step reversible, irreversible, and quasi-reversible reactions, multiple-reaction, and two-step consecutive charge transfer reaction was developed based on MOOSE. Although the model was not applied to analyze the experimental data in the present study, this model provides an efficient and easy way to understand the effect of various parameters on electrochemical reaction process.

The present study supplied a comprehensive study on the electrochemical separation of fission products and corrosion products in molten FLiNaK salt and will contribute greatly to the development of FHR.

Species Chemistry and Electrochemical Separation in Molten Fluoride Salt

Yafei Wang

GENEARAL AUDIENCE ABSTRACT

There is a significant increased demand for the generation of electricity with the fast development of modern society and economy. For well over 100 years, the dominant energy sources for producing electricity in the industrialized world are fossil fuels, notably coal, oil, and natural gas. The generation of electricity from fossil fuels is a major and growing contributor to the emission of greenhouse gases that contribute significantly to global warming. As clean and efficient energy, the nuclear power source has been an attractive alternative to traditional fossil fuels.

The fluoride salt cooled high temperature reactor (FHR) is a promising Generation-IV advanced nuclear reactor. FHR is a salt-cooled reactor in which the core contains a solid fuel and liquid salt coolant. It combines attractive attributes from previously developed reactors and has the advantages of, for example, low-pressure operation, high temperature power cycle, and passive decay heat rejection. However, the primary salt coolant can unavoidably acquire fission products from the fuel particles and corrosion products from structural material corrosion. Therefore, it is necessary to have a primary coolant clean-up system installed in the FHR to mitigate the contamination and ensure the continued operation of the reactor.

Electrochemical separation technique has been proposed as the online coolant clean-up method for FHR. Electrochemical separation can be typically done in a three-electrode cell system (working, counter, and reference electrodes). Through applying a proper electrical potential or a current, the target metal ions in the molten salt will be deposited on the working electrode. In that way, the contaminants, including fission products and corrosion products, can be taken out with a working electrode from the molten salt coolant. In this study, the fundamental behaviors of separation of La, Ce (represent lanthanide fission products) and Cr (represents corrosion products) in FLINAK were investigated. To achieve their separations, the present dissertation provided a comprehensive study about the electrochemical behaviors of La, Ce, and Cr species in molten FLiNaK salt at various situations, and relevant fundamental properties for guiding the conditions needed to be applied for the desired electrochemical separation. Considering the use of liquid bismuth as the extraction media for liquid/liquid separation and the electrode for electrochemical separation of fission products the fundamental properties of fission products and alkali metals in liquid bismuth are also determined in the present study to evaluate the separation behavior and viability. Finally, an electrochemical model for understanding the electrochemical process in the FHR salt coolant clean-up was developed. Overall, the work performed in this study will contribute greatly to facilitate the FHR development.

Acknowledgements

I am very thankful to my advisor, Jinsuo Zhang, for his full support, expert guidance, and constant help during my PhD study. I also would like to express my deepest gratitude to my committee members: Dr. Mark Pierson, Dr.Yang Liu, and Dr. Xianming Bai for their instructions and guidance.

I would like to thank my family and my fiancé for their endless love, encouragement and support. Because of which, I can pursue my dream freely.

Special thanks to Dr. Shaoqiang Guo, Dr.Jianbang Ge, Mr.Weiqian Zhuo, Ms. Amanda Leong, and Ms. Qiufeng Yang for their help on the experiment setup, SEM analyses, and XRD tests.

Finally, the present research is finically supported by DOE NEUP Award Number DE-NE0008306 for experiments and DE-NE0008756 for modeling. These funding supports from U.S. Department of Energy are highly appreciated.

Table of Contents

List of Figures

List of Tables

1. Introduction

1.1. History of molten salt reactor and its importance

Molten salt reactors (MSRs) were first proposed by Oak Ridge National Laboratory (ORNL) during the post-World War II to design a nuclear-powered aircraft in the United States [1,2,3]. Due to its great attraction of molten salt such as high boiling point, excellent stability, and passive decay heat cooling system, a program aimed at such an aircraft reactor was developed at ORNL from about 1950 to 1956 [4,5]. In 1954, this aircraft reactor was operated successfully for 100 h at an outlet temperature up to 860 ℃ and at power up to 2.5 MWt [6]. The motivation to using MSR for military ended at the end of the 1950s [1]. However, based on the promising results obtained during the aircraft reactor program, the development for MSRs technology was oriented to the civilian power application and continued in the names of Molten Salt Reactor Experiment (MSRE) in 1960s and Molten Salt Breeder Reactor (MSBR) in the end of 1960s and beginning of 1970s [2].

Despite the success of MSRs, this program was shut down in the early 1970s and the research interest was oriented to the liquid metal fast-breeder reactor. The modest MSRs program was restarted in the early 1980s by ORNL on design and materials development, fuel chemistry, and processing [4]. During this period, another MSRs design, the Denatured Molten Salt Reactor (DMSR) was also proposed. However, little advancement was made due to lack of research funding over the next 20 years after the 1980s and only a few scientists kept interest active for MSRs [7,8,9].

Interest in MSRs has increased significantly in recent years [10,11] and MSRs have been selected as one of the six Generation IV reactors. Given the diversity of the MSRs concepts, “fluoride salt-cooled high-temperature reactor” (FHR) was adopted in 2010 to distinguish fluoride salt-cooled MSRs from other MSRs. Since 2010, the Office of Nuclear Energy of Department of Energy (DOE-NE) started to support FHR development through the national laboratories and university research programs.

1.2. Design of FHR

The FHR design is based on the concept of advanced high temperature reactor (AHTR). As shown in Figure 1-1, the developed FHR inherits desirable attributes from other thermal power plants and has been treated as a promising advanced reactor concept because of the various advantages associated with it. For example, it will be operated at higher temperatures which leads to increased efficiency in generating electricity. In addition, the low operating pressure can reduce the risk of a large pipe break and loss of coolant. Figure 1-2 shows the designed schematic diagram of the FHR which consists of primary loops, intermediate loops, direct reactor auxiliary cooling system (DRACS) loops, and one power conversion loop. Because of the most favorable nuclear properties such as negative void coefficient [12] and low neutron absorption cross-section [13], FLiBe (67LiF-33BeF_2, mol%) is selected as the primary coolant. FLiNaK (46.5LiF-11.5NaF-42KF, mol%) and KF-ZrF_4 (58 KF-42 ZrF_4, mol%) are the two suggested coolants for the intermediate loop

due to their excellent performance on heat transfer, melting temperature and cost [14]. The DRACS has not yet been investigated thoroughly, the same salt as used for intermediate loop (i.e., FLiNaK or KF-ZrF_4) was chosen as the coolant candidate.

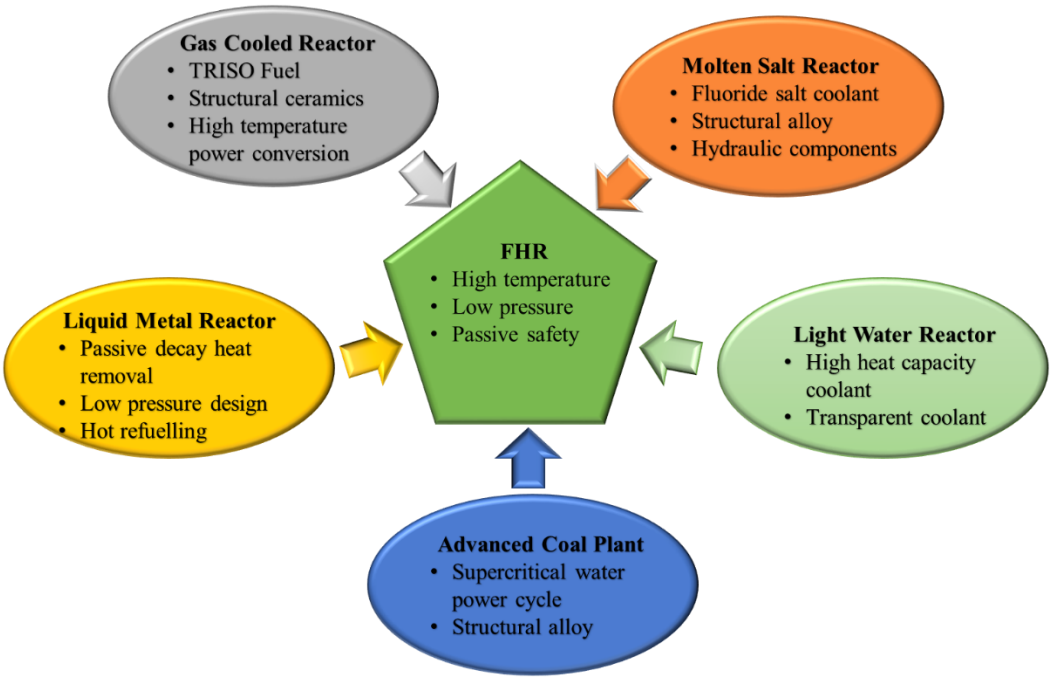

Figure 1-1. FHR attribute inheritance from earlier designed nuclear reactors [12].

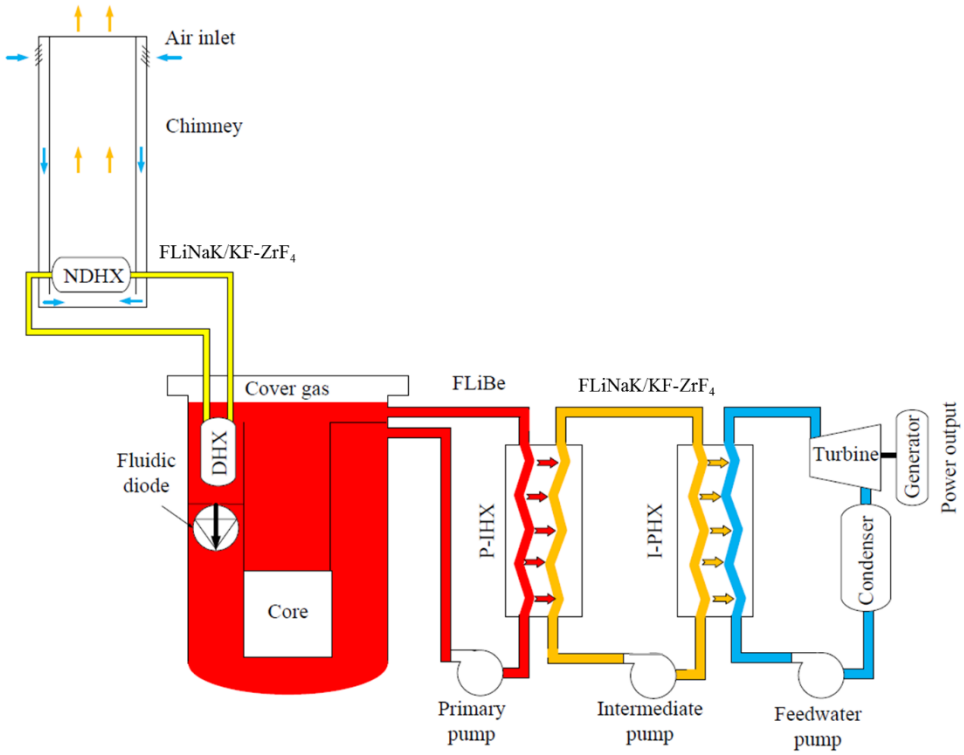

Figure 1-2. The designed schematic diagram of the FHR [15].

The primary coolant enters the reactor vessel through three segmented downcomer sections, flows down to the lower plenum, and then flows upward from the lower plenum to cool the fuel assemblies. The inlet temperature of the reactor primary coolant is designed for 650 ℃ and a primary coolant flow rate of 28500 kg/s is guaranteed to maintain the 50 ℃ temperature increase across the core at full power. There are 252 hexagonal fuel assemblies in the active core surrounded by graphite reflector blocks. Each fuel assembly is composed of 18 fuel plates suspended from a central Y-shaped support structure and enclosed in a hexagonal carbon-carbon fuel channel box, as shown in Figure 1-3. The central Y-shaped support structure is made of carbon-carbon composite material and a control blade with molybdenum hafnium carbide structure is inserted at the central region.

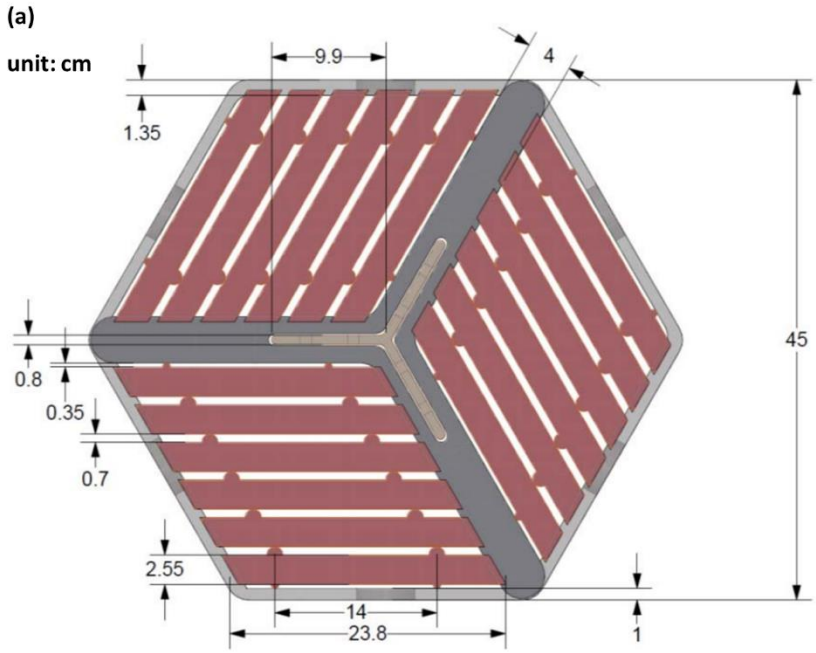

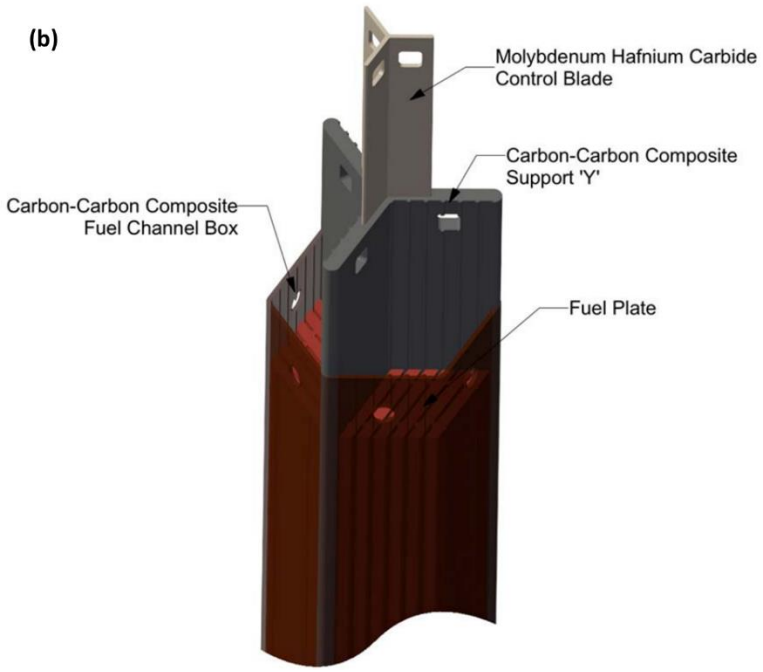

Figure 1-3. (a) Top view of the FHR fuel assembly. (b) View of the FHR fuel assembly, control blade, and supporting structure [12].

Figure 1-4 shows the cross section of a fuel plate in the FHR fuel assembly. The fuel plate is fabricated with carbon. The black strips represent graphite matrix regions which are filled with TRISO fuel particles. Individual TRISO fuel particle, less than 1 mm in diameter, consists of a fuel kernel with 9 wt% enriched U-235, buffer layer, a layer of pyrolytic graphite, a silicon carbide cladding layer, and another layer of pyrolytic graphite. Some small Eu_2O_3 (Eu-151 and Eu-153) spheres are also embedded within the graphite matrix to act as burnable absorbers. At the outer surface of the fuel plate, spacers are formed to maintain the coolant gap between adjacent plates, central support sections, and the channel box for coolant flow.

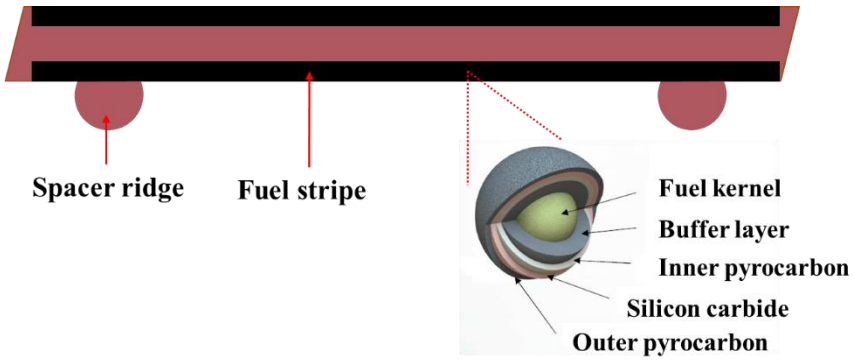

Figure 1-4. Cross section of a fuel plate.

1.3. Impurities in FHR molten salt coolant

There are some challenges with FHR reactor concept to make it a reality. For instance, the primary salt coolant in FHR can acquire actinides, fission products and other impurities, such as corrosion products, oxide, moisture, etc. from a series of routes. These impurities will pollute the salt coolant and harshly affect the neutronics, heat transfer, and material compatibility during the normal operation of FHR [16]. Based on the current available knowledge and operation experience in previous MSRs, the impurities in the primary salt coolant can be categorized into five groups: 1) fission products and actinides from fuel leakage; 2) corrosion products from structural material corrosion; 3) products from nuclear reactions such as nuclear transmutation and nuclear decay; 4) impurities from operating environments such as water and oxygen by air ingression; and 5) impurities from the coolant itself such as HF. The present work mainly focuses on the removal of impurities in the first two categories. Therefore, this section will discuss the contamination mechanisms, transports in molten salt, and impacts on the reactor normal operation of these fission products and corrosion products.

1.3.1. Fission products

FHR unavoidably contain some imperfect fuel particles, and some may have contamination or larger-than-anticipated amounts of defective fuel [17]. The resultant fission products can enter salt coolant from the leakage of fuel particles. The fission products in the form of Fp_xO_y (for oxide fuel) can form stable fluorides in the primary coolant by

$$Fp_xO_y + 2yF^- \overset{k}{\leftrightarrow} xFpF_{2y/x} + yO^{2-} \quad (1\text{-}1)$$

The concentration of formed $FpF_{2y/x}$ depends on the concentration of O^{2-} and equilibrium constant k of the above reaction. Due to the extremely low concentration of O^{2-} in primary coolant, fission product fluorides are likely to be formed, which has been demonstrated by the E-pO_2 diagrams for fluoride salt in previous studies [18]. Most fission product fluorides are very stable and some of them are even more stable than the primary salt coolant constituents. As a result, most fission products will not deposit on structural surfaces through the displacement reactions between fission product fluorides and structural material. However, in addition to reaction (1-1), the fission products may deposit out from the primary salt coolant in the form of compounds such as LaOF during the dissolution process of fission product oxides by F^- [19].

Due to the stability of fission product fluorides, the impacts on the material corrosion and radioactive risk should be minimal during the reactor normal operation. However, the stable fission product fluorides may affect the primary salt physical properties such as density and melting temperature. With aging, the accumulation of fission product fluorides may exceed the solubilities and then lead to their compound formation, which probably result in blockage of the flow path as well as a local higher temperature due to the decay heat. On the other hand, the neutronic property of the primary salt coolant will also be affected because of the large neutron cross-sections for most of the rare earth fission products.

1.3.2. Corrosion products

Corrosion of structural materials in the salt coolant is another concern for FHR since the salt impurities such as HF, oxygen, and some fission product species can dissolve the structural alloys. The dissolved alloy components such as Cr, Fe, and Ni will exist in the forms of their fluorides. Unlike the transport of fission product fluorides in salt coolant, corrosion products dissolve into the salt at one location (the location is not necessarily at the highest temperature) and precipitate out from the salt coolant at some other locations (the location is not necessarily at the lowest temperature) since the primary loop is a non-isothermal and closed loop [20]. Such phenomenon has been identified in the previous corrosion experiments [21].

The structural material corrosion may bring serious consequences to the normal operation of FHR. Some corrosion products can be the oxidizer of other metals. For example, the corrosion product NiF_2 is the oxidizer of Cr through the reaction:

$$Cr + NiF_2 \rightarrow CrF_2 + Ni \qquad (1\text{-}2)$$

In this way, the Cr can be corroded [22]. In addition, the precipitation of corrosion products may lead to fouling at the heat exchanger and affect its heat transfer performance. On the other hand, structural material degradation will be caused by the continuous corrosion. Moreover, some radioactive nuclides such as Cr-51 and Fe-59 can be produced when the corrosion products pass through the reactor core, and these nuclides can be radioactive source terms.

1.4. Available separation methods for salt coolant contaminants removal

Based on previous discussion, it is necessary to have a primary coolant cleanup system installed in FHR to mitigate the contamination and ensure the continued operation of reactor. As an ionic fluid, molten salt can realize its purification through various chemical or electrochemical methods. Among these methods, the liquid lithium-activate bismuth metal contacting system (liquid/liquid extraction) and electrochemical separation by applying a proper electrical potential or current are thought as the two best technologies for the removal of contaminants in the FHR primary coolant system.

1.4.1. Bi-Li extraction

Due to the low melting point, capability of dissolving actinides, fission products, and corrosion products, and immiscibility with molten salts, liquid bismuth can be applied in the nuclear field for the separations of actinides, fission products, and corrosion products from molten salts. Bi-Li/salt liquid-liquid extraction is a key purification method for molten salt and the extraction reaction without the formation of metallic compounds is expressed by [16]

$$M^{n+}\ (in\ salt) + nLi\ (in\ Bi) \leftrightarrow M\ (in\ Bi) + nLi^{+}\ (in\ salt) \qquad (1\text{-}3)$$

The schematic diagram for the Bi-Li extraction process in molten salt can be systemic shown in Figure 1-5.

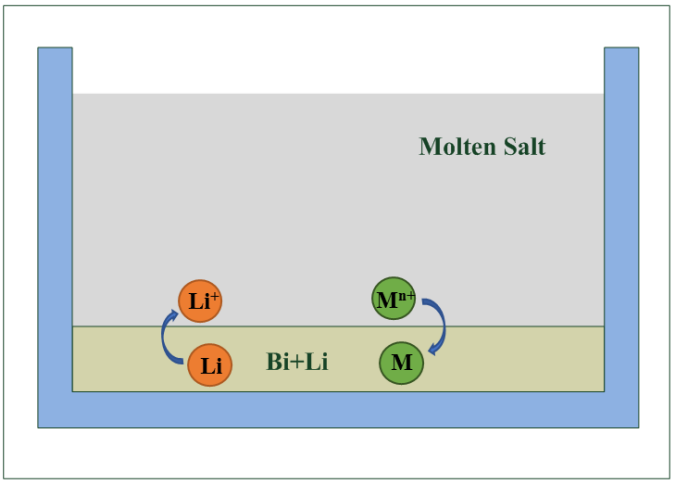

Figure 1-5. Schematic diagram of Bi-Li extraction in molten salt.

Reductive extraction in a salt/Bi-Li system was first proposed to process MSBR fuel salt [23,24]. This type of extraction has been studied extensively for many years at ORNL for the selective reduction of uranium, protactinium, and the rare earths from the thorium-containing molten salt fuel into liquid bismuth [25,26,27,28]. The extracted actinides in the bismuth pool can be later recovered back to the cleaned molten fluorides by electrochemical processing and sent back to the reactor core, while the rare earths in the bismuth is back-extracted to the molten chloride medium by electrochemical processing for disposal [29]. Molten salt/Bi-Li extraction is also treated as an ideal method in the pyroprocessing of spent nuclear fuel. It was first developed at Argonne National Laboratory as a part of the Integrated Fast Reactor Program [30,31] in which they developed a countercurrent pyrocontactor. Molten salt is intensively mixed with liquid Bi in the countercurrent procontactor for the effective chemical reactions between solute in molten salt and liquid Bi [32]. There can be multiple stages within a pyrocontacotr, and which will help to increase the separation efficiency.

Based on the great advantages of the Bi-Li extraction process, this technology is also being considered for the clean-up of the primary coolant salt for FHR [33,34]. In support of the development of the Bi-Li extraction process for FHR primary salt coolant clean-up, equilibrium distributions of lanthanide and actinide elements between bismuth and FLiBe or FLiNaK molten salt need to be determined. At a given temperature, if only species M^{n+} exist in the LiF-containing molten salt, the distribution of the element M between LiF-containing salt and liquid bismuth phase can be expressed by a general reaction:

$$MF_{n(salt)} + nLi_{(Bi)} \leftrightarrow M_{(Bi)} + nLiF_{(salt)} \qquad (1\text{-}4)$$

The equilibrium constant for equation (1-4) can be expressed by

$$K = \frac{\alpha_M \alpha_{LiF}^n}{\alpha_{MF_n} \alpha_{Li}^n} = \frac{X_M \gamma_M X_{LiF}^n \gamma_{LiF}^n}{X_{MF_n} \gamma_{MF_n} X_{Li}^n \gamma_{Li}^n} \quad (1\text{-}5)$$

where α is the activity, X is the mole fraction, and γ is the activity coefficient. Considering the element M and Li in liquid bismuth phase are present at low concentration in the application of Bi-Li extraction for FHR primary salt coolant clean-up, the values of γ_M and γ_{Li} can be assumed to be constant. In the salt phase, MF_n is present at low concentration since it exists as salt impurity while LiF is a major constituent of the salt. Consequently, the values of γ_{MF_n} and γ_{LiF} will also be nearly constant. Thus, equation (1-5) can be rewritten as

$$K' = \frac{X_M X_{LiF}^n}{X_{MF_n} X_{Li}^n} \quad (1\text{-}6)$$

The distribution coefficients are defined as

$$D_M = \frac{X_M}{X_{MF_n}} \quad (1\text{-}7)$$

$$D_{Li} = \frac{X_{Li}}{X_{LiF}} \quad (1\text{-}8)$$

Then equation (1-6) can be written as

$$D_M = (D_{Li})^n K' \quad (1\text{-}9)$$

or, in logarithmic form,

$$\log D_M = n \log D_{Li} + \log K' \quad (1\text{-}10)$$

The extraction behaviors of lanthanide and actinide elements in the Bi-Li extraction process is determined by their distribution coefficients. As a result, lots of studies have been performed to investigate the distribution coefficients of lanthanides and actinides in the binary phase systems of FLiBe and liquid bismuth. The available data for binary phase system FLiBe (67LiF-33BeF_2, mol%)/Bi-Li in the previous studies are reviewed and summarized in Table 1-1.

Table 1-1. Parameters obtained from equilibrium distributions of lanthanide and actinide elements between FLiBe (67LiF-33BeF_2, mol%) and bismuth.

Element (n)	T (K)	$\log D_M = n \log D_{Li} + \log K'$	Ref.
La (3)	873	$\log D_{La} = 3 \log D_{Li} + 7.33$	[35]
	873	$\log D_{La} = 3 \log D_{Li} + 6.92$	[36]
	973	$\log D_{La} = 3 \log D_{Li} + 6.36$	[36]
	1073	$\log D_{La} = 3 \log D_{Li} + 5.62$	[35]
Ce (3)	873	$\log D_{Ce} = 3 \log D_{Li} + 7.67$	[35]
	1073	$\log D_{Ce} = 3 \log D_{Li} + 5.98$	[35]

Nd (3)	873	$\log D_{Nd} = 3\log D_{Li} + 7.81$	[36]
Sm (2)	873	$\log D_{Sm} = 2\log D_{Li} + 4.74$	[36]
	873	$\log D_{Sm} = 2\log D_{Li} + 4.29$	[37]
Eu (2)	873	$\log D_{Eu} = 2\log D_{Li} + 3.86$	[36,38]
	873	$\log D_{Eu} = 2\log D_{Li} + 3.56$	[37]
Gd (3)	873	$\log D_{Gd} = 3\log D_{Li} + 6.22$	[36]
Dy (3)	873	$\log D_{Dy} = 3\log D_{Li} + 5.66$	[36]
Th (4)	873	$\log D_{Th} = 4\log D_{Li} + 10.20$	[39]
	873	$\log D_{Th} = 4\log D_{Li} + 9.73$	[36]
	973	$\log D_{Th} = 4\log D_{Li} + 8.70$	[36]
Pa (4)	873	$\log D_{Pa} = 4\log D_{Li} + 13.09$	[35]
	873	$\log D_{Pa} = 4\log D_{Li} + 13.30$	[36]
	1073	$\log D_{Pa} = 4\log D_{Li} + 10.19$	[35]
U (3)	873	$\log D_{U} = 3\log D_{Li} + 12.20$	[36]
Np (3)	873	$\log D_{Np} = 3\log D_{Li} + 10.52$	[36]
Pu (3)	873	$\log D_{Pu} = 3\log D_{Li} + 11.27$	[36]
Am (3)	873	$\log D_{Am} = 3\log D_{Li} + 11.44$	[36]
Cm (3)	873	$\log D_{Cm} = 3\log D_{Li} + 10.47$	[36]
Cf (3)	873	$\log D_{Cf} = 3\log D_{Li} + 11.47$	[36]

1.4.2. Electrochemical extraction

Electrochemical separation plays an important role in many modern technologies. In the nuclear industry, it is proposed to recover fissionable uranium and plutonium from spent nuclear fuel [40,41] and online clean molten salt fuels for MSR [42,43]. Therefore, it is also treated as a potential method for the primary salt coolant clean-up in FHR. For metal cations, the common electrochemical separation/deposition reaction is

$$M^{n+} + ne \rightarrow M \qquad (1\text{-}11)$$

Electrochemical separation can be typically done in an electrochemical cell system. As shown in Figure 1-6, through applying a proper electrical potential or a current, the target metal ions in the electrolyte will be deposited on the cathode. While on the anode, the anion in the solution will be oxidized. F^- is the primary anion in the solution when performing salt coolant clean-up for FHR. To avoid the oxidation of F^- and the generation of F_2, a type of sacrificial anode, Li dissolved in liquid Bi, can be utilized (Figure 1-7). By using this sacrificial anode, the Li in Bi-Li mixture will be driven into molten salt instead of generating F_2.

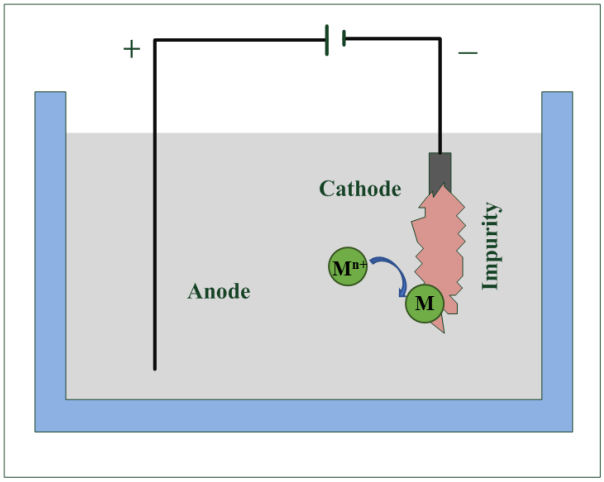

Figure 1-6. Schematic of the electrochemical separation/deposition.

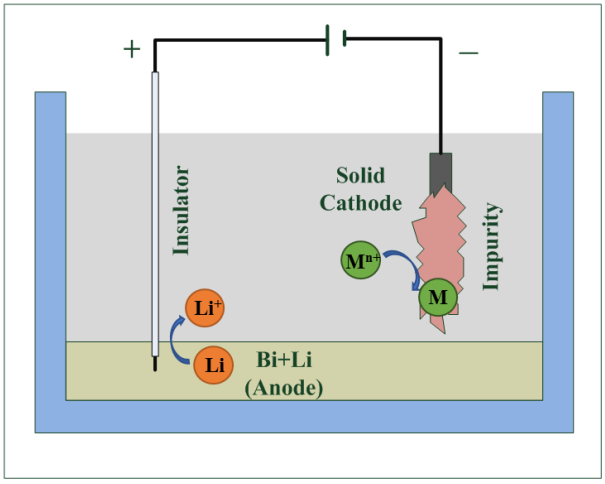

Figure 1-7. Schematic of the electrochemical separation/deposition with sacrificial anode.

The electrochemical deposition is carried out at a potential which is more negative than the equilibrium potential of the target metal ion. The equilibrium potential of a metal ion can be expressed by:

$$E_{M^{n+}/M} = E^{0}_{M^{n+}/M} + \frac{RT}{nF} ln\alpha_{M^{n+}} \qquad (1\text{-}12)$$

where $E^{0}_{M^{n+}/M}$ is the standard potential, R is the gas constant, T is the temperature in Kelvin, n is the electron transfer number, F is Faraday constant, and $\alpha_{M^{n+}}$ is the activity of M^{n+} in solution (molten salt in this study). For metal ions whose equilibrium potential for deposition is more positive than the major cations in molten salt (e.g., Li^{+} and Be^{2+} in FLiBe, Li^{+}, Na^{+}, and K^{+} in FLiNaK), a simple inert working electrode can be applied to deposit the target metals using electrochemical method.

In FHR primary salt coolant clean-up process, the acquaintance of the equilibrium potential is the prerequisite for determining whether the impurities can be deposited and separated

out from the molten salt. Based on Equation (1-12), the equilibrium potential depends on both the standard potential and the activity of element in the salt. The investigation of the activity of element in FLiBe and FLiNaK molten salts is very limited because of the lack of a stable function reference electrode. Standard potential can be obtained from thermodynamic calculation directly. Considering the standard potential can give rough information for instructing the electrochemical separation of impurities from molten salt when the activity is unknown, the standard potentials of some fission product fluorides and the major cations of FLiBe and FLiNaK molten salts are calculated and shown in Figure 1-8 based on the database in Outotec HSC Chemistry 6.0 [44] and thermodynamic calculation method reported before [45]. If only taking into account of standard potential, it is indicated that most of the lanthanide fission products cannot be separated out from FLiBe and FLiNaK molten salts. The standard potentials of corrosion products in molten fluoride salts are calculated in the previous study [45] in which it is reported all the corrosion products could be deposited out prior to the major cations in FLiBe and FLiNaK molten salts.

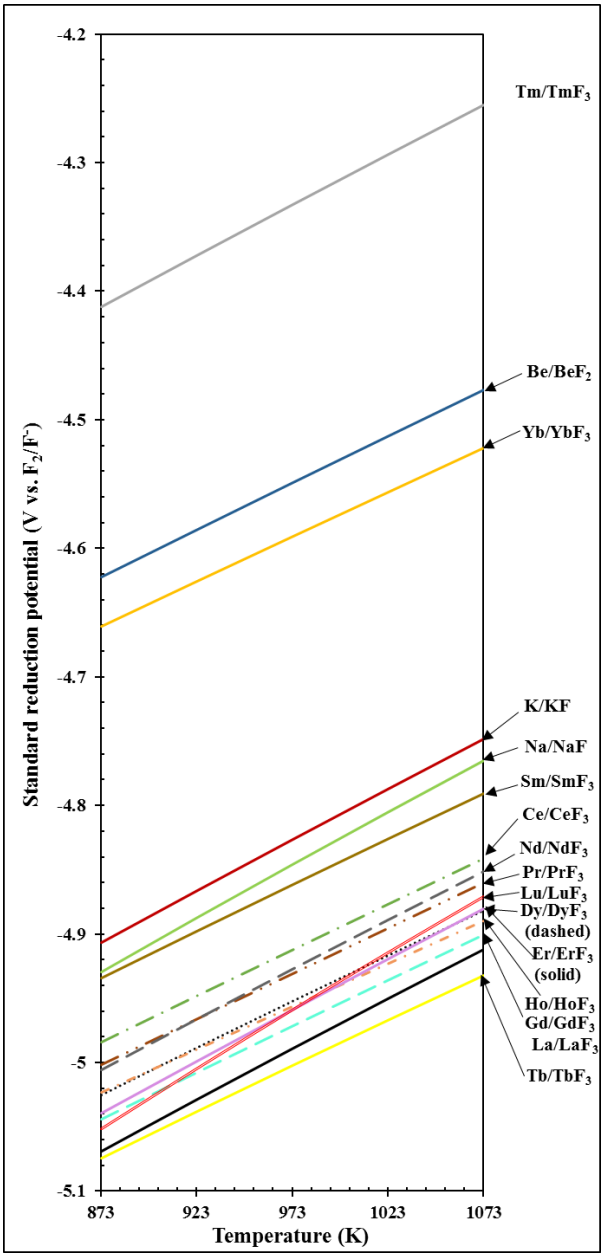

Figure 1-8. Standard potentials of fission product fluorides and major cations of FLiBe and FLiNaK molten salts at the temperature range of 873 to 1073 K based on the database in Outotec HSC Chemistry 6.0 [44].

1.4.2.1.Electrochemical extraction by solid reactive electrode

For impurity ion whose equilibrium potential is more negative than the major cations of FLiBe or FLiNaK molten salt, the molten salt major cation such as K^+ or Be^{2+} will preferentially deposit out over the impurity during the electrochemical separation process. To shift the equilibrium potential of impurity to a more positive value, one of the most frequent methods is to use a reactive electrode [46]. When using a solid reactive electrode, B, the electrochemical deposition reaction of M^{n+} on it can be written as

$$xM^{n+} + nxe^{-} + yB \leftrightarrow M_xB_y \quad (1\text{-}13)$$

where M_xB_y is the formed intermetallic compound between target metal *M* and reactive electrode *B*. Then the equilibrium potential of M^{n+}/M_xB_y is

$$E_{M^{n+}/M_xB_y} = E_{M^{n+}/M} - \frac{1}{x}\frac{\Delta G(M_xB_y)}{nF} \quad (1\text{-}14)$$

where $E_{M^{n+}/M}$ is the equilibrium potential when pure *M* is deposited on an inert electrode, $\Delta G(M_xB_y)$ is the Gibbs free energy of formation of compound M_xB_y. The value of E_{M^{n+}/M_xB_y} will be more positive than $E_{M^{n+}/M}$ if the value of $\Delta G(M_xB_y)$ is negative and the electrodeposition of M^{n+} will happen at a more positive potential. Through this method, the electrochemical separations of some stubborn fission products from both molten chloride salts and fluoride salts have been achieved successfully, for instance, the separations of Sm from molten chloride salt by Al and Zn reactive electrodes [47,48], Eu from molten fluoride salt by Cu reactive electrode [49], and Gd from molten fluoride salt by Ni reactive electrode [50].

Ni and Cu are the two most popular solid reactive electrodes for the electrochemical separations of stubborn fission products in molten fluoride salts. The information about the potential shift when using solid reactive electrode is very important for guiding the electrochemical separations of fission products in the FHR primary salt clean-up process. Therefore, the intermetallic compounds formed between fission products and these two reactive electrodes, the Gibbs free energy of formation of the formed intermetallic compounds, and the potential shift brought are summarized in Table 1-2 and Table 1-3. From which it is shown that a great positive potential shift can be obtained when using Ni and Cu as the solid reactive electrodes to separate fission products from molten salts.

Table 1-2. The Gibbs free energy of formation of the formed intermetallic compounds and the corresponded potential shift when using Ni reactive electrode to separate fission products at 973 K.

Element	Intermetallic compound	G_f (J/mol)	Electron transfer number	Potential shift (V)
La [51]	La_3Ni	-61592	3	0.071
	La_7N_{i3}	-179074		0.088
	LaNi	-51444		0.178
	La_2Ni_3	-124781		0.216
	La_7Ni_{16}	-550090		0.271
	$LaNi_3$	-92725		0.320
	La_2Ni_7_α	-203522		0.352
	La_2Ni_7_β	-202944		0.351
	$LaNi_5$	-124879		0.431
Ce [52]	Ce_7Ni_3	-219846	3	0.109

	CeNi	-66022		0.228
	$CeNi_3$	-133040		0.460
	Ce_2Ni_7	-290625		0.502
	$CeNi_5$	-173488		0.599
Pr [53]	$PrNi_5$	-89265	3	0.308
	Pr_2Ni_7	-151230		0.261
	$PrNi_3$	-70456		0.243
	$PrNi_2$	-59318		0.205
	PrNi	-40994		0.142
	Pr_7Ni_3	-144139		0.071
	Pr_3Ni	-49360		0.057
Nd [54]	Nd_3Ni	-81364	3	0.094
	Nd_7Ni_3	-234801		0.116
	NdNi	-70280		0.243
	$NdNi_2$	-97158		0.336
	$NdNi_3$	-114230		0.395
	Nd_2Ni_7_ α	-243333		0.420
	Nd_2Ni_7_ β	-240378		0.415
	$NdNi_5$	-139605		0.482
	Nd_2Ni_{17}	-278595		0.481
Sm [55]	Sm_3Ni	-70852	2	0.122
	SmNi	-64748		0.336
	$SmNi_2$	-98001		0.508
	$SmNi_3$	-126753		0.657
	Sm_2Ni_7	-279046		0.723
	Sm_5Ni_{19}	-734447		0.761
	$SmNi_5$	-171742		0.890
	Sm_2Ni_{17}	-365829		0.948
Eu [56]	Eu_2Ni_{17}	-197728	2	0.512
	$EuNi_5$	-94879		0.492
	$EuNi_2$	-54563		0.283
	EuNi	-35898		0.186
Dy [57]	Dy_3Ni	-93969	3	0.108
	Dy_3Ni_2	-178528		0.206
	DyNi	-84455		0.292
	$DyNi_2$	-129214		0.446
	$DyNi_3$	-149343		0.516
	Dy_2Ni_7	-314274		0.543
	$DyNi_4$	-163121		0.564
	Dy_4Ni_{17}	-661146		0.571
	$DyNi_5$	-170533		0.589
	Dy_2Ni_{17}	-351233		0.607
Ho [58]	Ho_3Ni	-88601	3	0.102
	Ho_3Ni_2_LT	-172106		0.198

	Ho_3Ni_2_HT	-212570		0.245
	HoNi	-83109		0.287
	$HoNi_2$	-118082		0.408
	$HoNi_3$	-144992		0.501
	Ho_2Ni_7	-313093		0.541
	Ho_2Ni_5	-209757		0.362
	Ho_2Ni_{17}	-364981		0.630
Er [53]	Er_3Ni	-65552	3	0.075
	Er_3Ni_2	-123035		0.142
	ErNi	-58054		0.201
	$ErNi_2$	-90303		0.312
	$ErNi_3$	-116660		0.403
	Er_2Ni_7	-241747		0.418
	$ErNi_4$	-124074		0.429
	Er_4Ni_{17}	-500978		0.433
	Er_5Ni_{22}	-629359		0.435
	$ErNi_5$	-128049		0.442
	Er_2Ni_{17}	-264378		0.457
Yb [56]	Yb_2Ni_{17}	-234983	3	0.406
	$YbNi_5$	-109848		0.379
	YbN_{i3}	-76860		0.266
	$YbNi_2$	-53904		0.186
	YbNi_LT	-28616		0.099

Table 1-3. The Gibbs free energy of formation of the formed intermetallic compounds and their corresponded potential shift when using Cu reactive electrode to separate fission products at 973K.

Element	Intermetallic compound	G_f (J/mol)	Electron transfer number	Potential shift (V)
La [59]	La_3Cu_{37}	-196991	3	0.227
	$LaCu_6$_α	-65142		0.225
	$LaCu_6$_β	-69665		0.241
	$LaCu_5$	-65059		0.225
	$LaCu_4$	-58755		0.203
	$LaCu_2$	-45055		0.156
	LaCu	-21894		0.076
Ce [60]	$CeCu_6$	-78147	3	0.270
	$CeCu_5$	-71827		0.248
	$CeCu_4$	-64779		0.224
	$CeCu_2$	-50010		0.173
	CeCu	-26564		0.092
Pr [60]	$PrCu_6$	-88615	3	0.306
	$PrCu_5$	-81888		0.283
	$PrCu_4$	-74711		0.258
	$PrCu_2$	-58448		0.202

	PrCu	-33227		0.115
Nd [60]	$NdCu_6$	-91949	3	0.318
	$NdCu_5$	-85082		0.294
	$NdCu_4$	-77568		0.268
	$NdCu_2$	-60414		0.209
	NdCu	-35210		0.122
Sm [60]	$SmCu_6$	-94780	2	0.491
	$SmCu_5$	-89222		0.462
	$SmCu_4$	-81822		0.424
	$SmCu_2$	-62634		0.325
	SmCu	-41185		0.213
Eu [61]	$EuCu_5$	-33403	2	0.173
	$EuCu_2$	-17219		0.089
	EuCu	-10058		0.052
	Eu_2Cu	-8525		0.022
Gd [62]	$GdCu_6$	-95568	3	0.330
	$GdCu_5$_LM	-95109		0.329
	$GdCu_5$_HM	-95113		0.329
	Gd_2Cu_9	-190244		0.329
	Gd_2Cu_7	-157396		0.272
	$GdCu_2$	-65521		0.226
	GdCu	-42895		0.148
Dy [63]	DyCu7	-97449	3	0.337
	$DyCu_5$_LM	-98376		0.340
	$DyCu_5$_HM	-98279		0.340
	Dy_2Cu_9	-192781		0.333
	Dy_2Cu_7	-164140		0.284
	$DyCu_2$	-70520		0.244
	DyCu	-50781		0.175
Ho [64]	$HoCu_5$_α	-97337	3	0.336
	$HoCu_5$_β	-97110		0.335
	Ho_2Cu_9	-189539		0.327
	Ho_2Cu_7	-155549		0.269
	$HoCu_2$	-65446		0.226
	HoCu	-47488		0.164
Er [65]	$ErCu_5$	-96874	3	0.335
	Er_2Cu_9	-187114		0.323
	Er_2Cu_7	-159349		0.275
	$ErCu_2$	-64001		0.221
	ErCu	-48313		0.167
Tm [66]	$TmCu_5$	-82641	3	0.286
	Tm_2Cu_9	-157495		0.272
	Tm_2Cu_7	-126720		0.219
	$TmCu_2$	-53236		0.184
	TmCu	-38163		0.132

Yb [61]	$YbCu_5$	-79179	3	0.274
	Yb_2Cu_9	-157268		0.272
	Yb_2Cu_7	-138683		0.240
	$YbCu_2$	-36534		0.126
	YbCu	-32377		0.112

1.4.2.2. Electrochemical extraction by liquid metal electrode

The use of liquid metal electrode is another good method to shift the equilibrium potential of impurity ion to a more positive value. For a liquid metal electrode, the electrochemical deposition reaction on it can be expressed by

$$M^{n+} + ne^- \leftrightarrow M \text{ (in liquid electrode)} \quad (1\text{-}15)$$

Then the electrochemical deposition potential becomes

$$E_{\text{eq(in liquid electrode)}} = E_{M^{n+}/M} - \frac{RT}{nF}\ln(\alpha_M(\text{in liquid electrode})) \quad (1\text{-}16)$$

where α_M is the activity of M in liquid metal electrode and can be expressed by $\alpha_M = X_M\gamma_M$ with γ_M the activity coefficient and X_M the concentration in mole fraction. Comparing with common inert electrodes, a liquid metal electrode makes the electrodeposition of the target metal ions proceed at a more positive potential, especially when the activity of the target element in liquid metal is extremely small. For example, with a liquid bismuth electrode in which the activity of barium metal is only 3.7×10^{-15}, barium ions have been successfully separated from $BaCl_2$-LiCl-$CaCl_2$-NaCl molten salt at 773-973 K [67].

Liquid bismuth is being considered for the primary salt coolant clean-up to separate the fission products resulting from fuel leakage in fluoride salt cooled high temperature reactor (FHR) [68]. When using liquid bismuth as electrode to perform the electrochemical separation, the activity and activity coefficient are essential knowledge for assessing the viability of bismuth in separating fission products species from molten salts. Consequently, massive studies have been conducted to study the activity coefficients of fission products in liquid bismuth. In these studies, most of them (if not all) investigated the activity coefficients in the infinite dilutions or were based on the assumption of the infinite dilutions in which the activity coefficient is independent of concentration. Table 1-4 summarizes the activity coefficients of fission products in liquid bismuth and the potential shift calculated from equation (1-16) based on the assumption of $X_M = 0.5$ mol%.

Table 1-4. Activity coefficients of fission products in liquid bismuth and the potential shift calculated from equation (1-16) based on the assumption of X_M=0.5mol% at the temperature of 973 K.

Element	Activity coefficient	Electron transfer number	Potential shift (V)	Studies
La	3.80×10^{-11}	3	0.819	[69]

	2.95×10^{-11}		0.826	[70]
	5.25×10^{-11}		0.810	[71]
	4.27×10^{-11}		0.815	[72]
	3.98×10^{-11}		0.817	[73]
Nd	2.45×10^{-11}	3	0.831	[74]
	3.31×10^{-10}		0.758	[75]
	2.57×10^{-10}		0.765	[76]
Sm	4.46×10^{-11}	2	1.221	[73]
Eu	3.73×10^{-8}	2	0.939	[73]
Gd	1.20×10^{-9}	3	0.722	[77]
	1.15×10^{-9}		0.723	[69]
	6.76×10^{-10}		0.738	[76]
	1.26×10^{-9}		0.721	[78]
	1.91×10^{-9}		0.709	[72]
	1.17×10^{-9}		0.723	[73]
Tb	1.91×10^{-9}	3	0.709	[69]
Dy	1.86×10^{-9}	3	0.710	[79]
	1.10×10^{-9}		0.725	[69]
Ho	2.88×10^{-9}	3	0.698	[80]
	4.07×10^{-9}		0.688	[81]
Er	8.32×10^{-9}	3	0.668	[69]
	4.27×10^{-9}		0.687	[70]

1.5. Research methods

1.5.1. Experiment measurement setup and techniques

All experiments and sample preparations were carried out under argon atmosphere in a glovebox (Inert Technology) as shown in Figure 1-9 where the moisture and oxygen levels were maintained under 0.5 ppm and 5 ppm, respectively. For the electrochemical experiment, an electrochemical test cell was designed based on a muffle furnace (Thermofisher Scientific FB1315M) for which the temperature can be maintained within $\pm$1℃ and a customized lid that allows the electrodes to pass through (Figure 1-10). The electrochemical techniques utilized in electrochemical tests are the methods measuring the response of current or potential when a potential or current is applied with certain patterns, respectively. The available electrochemical techniques mainly include cyclic voltammetry (CV), chronopotentiometry (CP), potentiodynamic polarization scan (PS), square wave voltammetry (SWV), chronoamperometry (CA), linear scan voltammetry (LSV) and normal pulse voltammetry (NPV). Among them, CV, CP, and PS are principally applied in the present study.

Figure 1-9. Glovebox system.

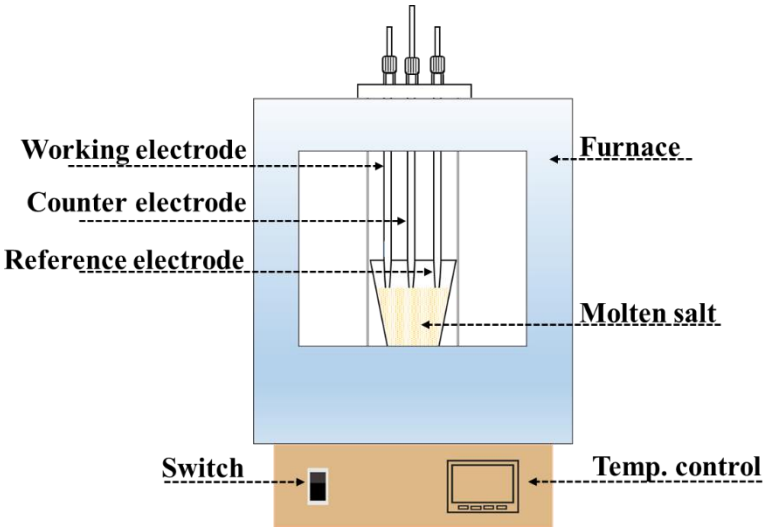

Figure 1-10. Electrochemical test cell.

1.5.1.1. Cyclic voltammetry

CV is an electrochemical technique which can measure the current response when a potential is applied. During the CV test, the potential is ramped linearly versus time on the working electrode in one direction and then ramped back in the opposite direction to the initial point once the set potential is reached (Figure 1-11 (a)). The corresponding current is recorded and plotted against the potential to give the cyclic voltammogram as shown in Figure 1-11 (b). In the CV test, a reduction reaction happens and current starts to flow when the electrode potential is scanned to the vicinity of equilibrium reduction potential. As the potential continues to grow more negative, the surface concentration of the cation must drop. Hence, the flux to the surface and the current increases as shown in Figure 1-11 (b). When the potential moves past equilibrium reduction potential, the surface concentration drops nearly to zero, the mass transfer and current reach its maximum value, it corresponds to the peak current in Figure 1-11 (b). The oxidation reaction happens when the potential is scanned back, and the same principle is applied as the reduction process.

In a CV experiment, current peaks versus applied voltage will show up when the redox reaction happens. Hence, it is a good way to study the electrochemical behaviors of contaminants in FLiNaK melt. In addition, the peak currents in CV can be used to study the diffusion coefficient based on the derived Delahay equation [82] and Berzins equation [83]. On the other hand, the information of apparent potential which is used for instructing the electrochemical separation can be obtained from the potential location of peak current. Depending on the potential locations of peak current and half peak current, the electron transfer number of an electrochemical reaction can also be identified. In more recent research, CV is used to determine the exchange current density, which makes CV an even more attractive method for electroanalytical research [84].

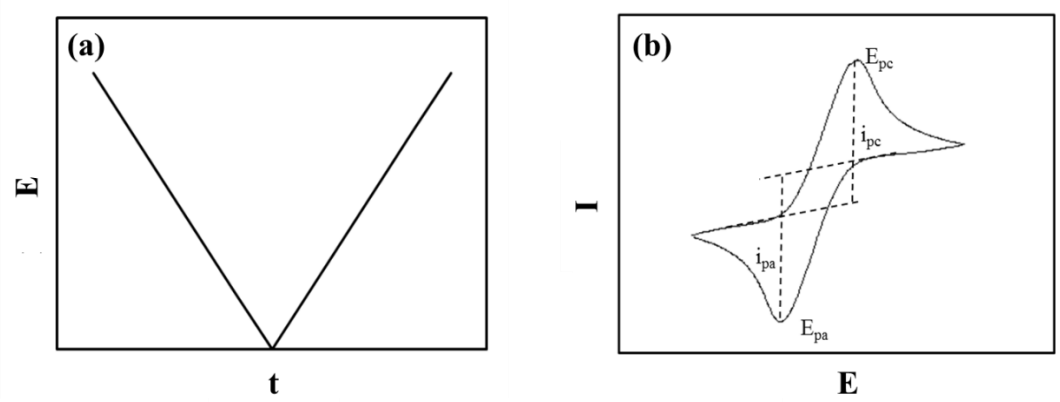

Figure 1-11. Pattern of applied potential and typical current response in CV.

1.5.1.2.Chronopotentiometry

For the CP method, the potential change on the working electrode is monitored after a constant current i_d is applied, as shown in Figure 1-12 (a). The applied current causes the noblest element to be reduced first at a constant rate. Correspondingly, the potential of the electrode moves to values characteristic of that redox couple and varies with time as the redox couple concentration ratio changes at the electrode surface, as shown in Figure 1-12 (b). After the concentration of the noblest element at the electrode surface drops to zero, the potential will then rapidly shift toward more negative values until a new, second reduction process can start. The time after application of the constant current when this potential transition occurs is called the transition time, τ, which is related to the concentration by Sand's equation [85] and can be used to get information about the diffusion coefficient.

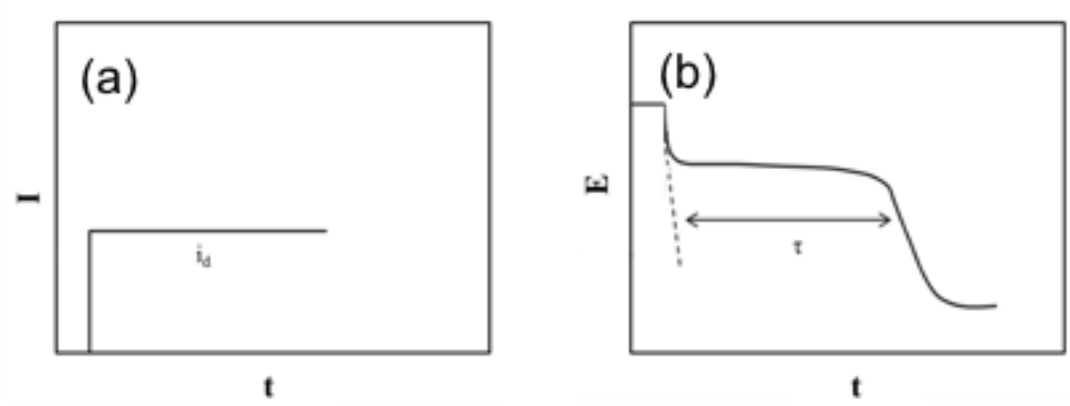

Figure 1-12. Pattern of applied current and typical potential response in CP.

1.5.1.3. Potentiodynamic polarization scan

For the PS method, the potential is swept slowly from the negative overpotential to the anodic direction. The corresponding current is plotted in log scale absolute value form versus applied potential. In the PS test, the current decreases rapidly to zero when the swept potential approaches the equilibrium potential and then rises back quickly as the potential is swept away from its equilibrium potential. In the cathodic section where the swept potential is more negative than the equilibrium potential, the noblest element has a reduction reaction and forms a layer on the working electrode. While in the anodic section where the swept potential is more positive than the equilibrium potential, the anodic reaction occurs, and the dissolution of the formed layer predominates. The non-simplified electrode kinetic equation [86,87] can be used to describe the PS curve through which some kinetic parameters such as charge transfer coefficient, standard reaction rate, and exchange current density can be obtained.

1.5.2. Calculation of phase diagram (CALPHAD) model

CALPHAD method is the process to seek a stable or metastable phases and phase boundaries. Proposed by Kaufman and Bernstein [88] in the early 1970s, the CALPHAD method has been applied widely in the material research fields [89]. This method is based on the theory that the equilibrium states under a given condition have the minimum Gibbs free energy and the coexisting states have the same chemical potential. Therefore, the stable phases can be found by minimizing the Gibbs free energy of the system and the phase boundaries can be plotted by seeking the same chemical potential. In the CALPHAD method, all the phases in the phase diagram can be described through Gibbs free energy by applying a mathematical model containing adjustable parameters. One can collect and assess all the available experimental data on phase equilibria and thermodynamic properties in a system. Then the adjustable parameters can be evaluated by optimizing the mathematical model to all the collected data. In that way, the phase diagram can be extended to the whole composition range beyond the experiments and some other unknown properties such as enthalpy of formation, entropy of formation, enthalpy of mixing, heat capacity, and activity coefficient can also be derived from the optimized mathematical model.

1.5.3. MOOSE model

MOOSE (Multiphysics Object Oriented Simulation Environment) is a software developed by Idaho National Lab to solve systems of coupled non-linear partial differential equations based on finite element method. The foundation of MOOSE is formed by the mathematical principle of Jacobian-free Newton-Krylov (JFNK) [90] in which the partial differential equations (PDE) need to be solved will be written in their weak forms. Based on the implementation of JFNK in MOOSE requires only residual evaluation of the discrete system, MOOSE uses a modular architecture to provide a convenient way to add and couple various physics together with material properties and boundary conditions [91]. Residing underneath the physics layer, MOOSE provides a set of core functionality necessary for residual and Jacobian evaluation [91]. Moreover, MOOSE employs the interfaces in libMesh through which diverse large-scale parallel computing resources can be utilized.

To develop a practical calculation in MOOSE, three important modules: kernels, boundary conditions, and materials need to be set. Physics expressions are modularized into kernels and each kernel must supply a residual but may provide a Jacobian optionally [91]. In MOOSE itself, a library of kernels describing the commonly used solid mechanics, phase field models, etc., is supplied and can be used directly. During the running of MOOSE, the input kernels are combined into complete residuals describing the problem to be solved. Boundary Conditions, representing constraints of variables with residuals and Jacobians being evaluated on boundaries, need to be developed by the user during the practical calculation. However, several typical boundary conditions such as Dirichlet and Neumann type boundary conditions are already included in MOOSE itself which can be used by user straightly [91]. The material system in MOOSE is used for the creating of material objects which can calculate the material properties before the residuals computation by kernels.

1.6. Research motivation

As discussed in the previous sections, FHR primary coolant can acquire contaminants, including fission products and corrosion products from fuel failure and structural material corrosion. Electrochemical separation and Bi-Li extraction are proposed as the two best methods for the FHR primary coolant on-line clean-up. As the secondary coolant and the surrogate of FLiBe molten salt, FLiNaK is mainly focused on in the present study. The investigation about the FLiBe molten salt is not performed in this study because of high toxicity of beryllium.

The electrochemical behaviors of lanthanide fission products in FLiNaK molten salt are rarely investigated in the previous studies. Considering the relatively negative standard reduction potentials of lanthanide fission products (as shown in Figure 1-8), the electrochemical behaviors of lanthanide fission products in molten FLiNaK salt are urgent to be known to determine the feasibility of their electrochemical separations. At the same time, to predict the separation performance and efficiency, the fundamental properties, such as diffusion coefficient, of lanthanide fission products and corrosion products in molten FLiNaK salt are also needed to be understood. For the stubborn lanthanide fission

products which have more negative equilibrium potentials than the main cations of molten FLiNaK salt (i.e., Li^+, Na^+, and K^+), solid reactive electrode and liquid metal electrode will be attempted to achieve the separations. However, considering the shortcomings existing in the electrochemical separation assisted by solid reactive electrode and liquid metal electrode such as the isolation of the reactive electrode due to the formation of compound and the ability to maintain a low activity value of active metal in liquid electrode, an innovative method will be developed to separate the stubborn lanthanide fission products but also overcomes the shortcomings.

Based on the broad applications of bismuth for the separations of fission products from molten salt. The knowledge of activity coefficient is an essential requirement for the coolant clean-up in the FHR. Plenty of studies have been conducted to study the activity coefficients of fission products in liquid bismuth. However, most of them investigated the activity coefficients in the infinite dilutions which is far enough from the practical applications. Therefore, it is necessary to study the activity coefficients of fission products in liquid bismuth at different concentrations rather than limiting to the dilution situation. As the main constituents of FLiNaK molten salt, the equilibrium potentials of K and Li will also be affected by their activity coefficients in liquid bismuth when liquid bismuth electrode is used for the electrochemical separations of fission products. As a result, the activity coefficients of K and Li in liquid bismuth at different concentrations will also be studied for identifying whether the target fission products can be preferentially electrodeposited over K and Li.

Although the present work mainly focuses on FLiNaK, not FLiBe molten salt, the research performed and the results obtained are still meaningful for the development of FHR. For example, the electrochemical behaviors and separations of species in molten FLiNaK salt are extremely useful for the secondary coolant clean-up when the pipe break happens in the primary-to-intermediate heat exchanger (P-IHX as shown in Figure 1-2). In addition, considering the similar properties of FLiNaK and FLiBe molten salts, the electrochemical behaviors and fundamental properties obtained for fission products and corrosion products here will be an important reference towards guiding future relevant studies in FLiBe molten salt. Moreover, no matter what kind of salt coolant is used, the data reported about the activity of lanthanide fission products and alkali metals in liquid bismuth will not be affected. Therefore, the obtained knowledge of these activities is still crucial to assess the extraction behavior and viability of bismuth in separating fission products from FLiBe primary salt coolant. The models developed based on MOOSE are for different kinds of general electrochemical reaction processes. It does not change because of the electrolyte and will also be significant for the electrochemical separation study in FLiBe molten salt.

2. Electrochemical behaviors and separations of lanthanum and cerium in molten FLiNaK salt

2.1. Introduction

Lanthanum and cerium are two typical lanthanide fission products in nuclear reactors [92] and the ions of which dissolved in the molten salt are commonly taken as model systems for electrochemical separation study of lanthanide fission products in molten salt. For LaF_3 in FLiNaK molten salt, Qiao et al [93] performed the electrochemical investigation and found there was no cathodic /anodic peak related to lanthanum redox reaction shown up in their cyclic voltammetry test when using inert Mo working electrode. Chesser et al [94] recently also did cyclic voltammetry tests in pure FLiNaK and FLiNaK-LaF_3 systems using inert tungsten working electrode, respectively. An additional pair of redox peaks was found to show up when LaF_3 was added into molten FLiNaK salt, which is different from the result reported by Qiao et al [93]. The electrochemical study of CeF_3 in FLiNaK molten salt has not been studied by other investigators.

It is usually claimed that the electrochemical separations of LaF_3 and CeF_3 in FLiNaK molten salt cannot be realized since the standard reduction potentials of La (III) and Ce (III) lay in a more cathodic area than the decomposition of FLiNaK melt. Figure 2-1 shows the calculated standard reduction potentials for the elements in FLiNaK-LaF_3 and FLiNK-CeF_3 systems based on the database in Outotec HSC Chemistry 6.0 [95]. The figure shows that the standard reduction potentials of La (III) and Ce (III) indeed are more cathodic than that of the basic salt melt constituents: K (I) and Na (I). Therefore, theoretically it is hard to extract lanthanum and cerium from FLiNaK molten salt by merely using inert working electrode.

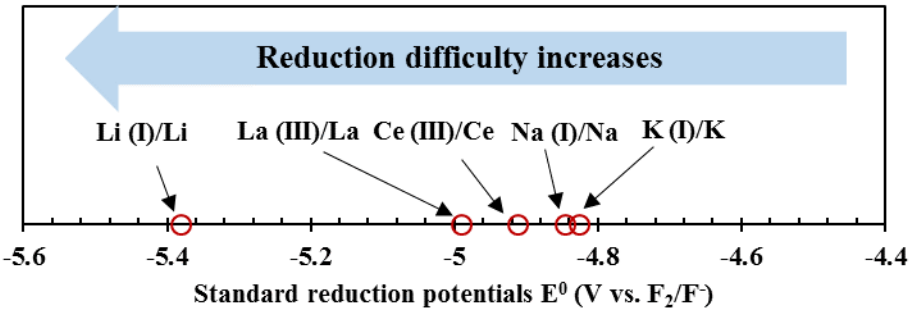

Figure 2-1.Standard reduction potentials of La (III)/La, Ce (III)/Ce, Li (I) /Li, Na (I)/Na, and K (I)/K at 973 K.

Considering the contrary results reported on electrochemical study of LaF_3 in FLiNaK molten salt by Qiao et al [93] and Chesser et al [94], the present chapter studied the electrochemical behavior of LaF_3 in FLiNaK molten salt through the combination of electrochemical and material characteristic methods. The feasibility of the separation of lanthanum from FLiNaK molten salt by inert working electrode was confirmed, which is conflict with the theoretical calculation shown in Figure 2-1. To figure out the reason for

this phenomenon, a series of experiments were performed, and the explanations were given. Electrochemical studies of CeF_3 in FLiNaK molten salt were also carried out at the temperature of 973 K using W inert working electrode, a similar phenomenon was also observed as the ones obtained in FLiNaK-LaF_3 system. In addition to W inert working electrode, reactive electrodes Cu and Ni were used to proceed the electrochemical deposition potential of Ce by forming intermetallic compounds. It turned out only the Ni electrode was feasible for proceeding the deposition potential and the intermetallic compound was identified as $CeNi_5$. The investigation on the electrochemical behaviors and separations of lanthanum and cerium in FLiNaK molten salt will greatly facilitate the development of lanthanide fission product clean-up in FHR salt coolant.

2.2. Experimental

Sample preparation and experiments were performed in a glove box (PureLab HE, Innovative Technologies) which was filled with argon gas. The moisture and oxygen level inside the glovebox were both maintained under 5 ppm. Reagents used for this work includes lithium fluoride (>99.0% purity, Sigma Aldrich), sodium fluoride (>99.0% purity, Sigma Aldrich), potassium fluoride (>99.5% purity, Sigma Aldrich), lanthanum fluoride (99.99% purity, Sigma Aldrich), and cerium fluoride (99.99% purity, Sigma Aldrich). The salts are weighed by a precision balance with an accuracy of 0.0001 g (MS 105DU Mettler Toledo). The weighed salt was mixed well before transferred to a nickel crucible (Sigma Aldrich) and placed in a muffle furnace (Thermofisher Scientific FB1315M) for which the temperature can be maintained within ± 1℃ during the experiment. The salt mixture was dehydrated at 473 K for 24 hours before heating to the target temperature.

The electrochemical experiments were carried out using a Gamry Interface 1000 Potentiostat and a standard three-electrode setup. The working electrodes used are 1.0 mm diameter tungsten rod (Midwest Tungsten Service, >99.5% purity), 3.17 mm diameter molybdenum rod (99.95 % purity, Alfa Aesar), 2.9 mm diameter copper rod (Surepure Chemetals,99.99% purity), and 3.2 mm diameter nickel rod (Fisher Scientific, 99% purity). The surface area of the working electrode was measured according to the length of the electrode exposed to the salt melt. The inert counter electrode used was a 3.05 mm diameter graphite rod (99.9995% purity, Alfa Aesar). The reference electrode utilized was a 0.81 mm diameter platinum wire (Surepure Chemetals) with potential associated to $Pt/PtO_x/O^{2-}$ [96]. It has been proved to be a reliable quasi-reference electrode in molten salts [96,97]. The surface area of the working electrode was measured according to its depth after being dipped into the salt melt. Open circuit potential (OCP) was performed before any electrochemical tests to confirm the stabilization of the system. IR compensation that was programmed in Gamry Framework software was selected during the electrochemical experiment [98].

To get the cathode deposition for XRD analysis, electrolysis was performed on a nickel foil (0.1 mm thick, 99.5% purity, Alfa Aesar). The XRD sample was sealed in a Kapton tape to avoid exposure to air during the XRD test. The cathode depositions were also characterized using scanning electron microscopy (SEM, FEI Quantan 600) to examine its composition and morphology.

2.3. Electrochemical separation study of LaF_3 in molten FLiNaK salt by inert working electrode

The electrochemical behavior of lanthanum in FLiNaK molten salt was studied by cyclic voltammetry and chronopotentiometry test. Figure 2-2 (a) shows the obtained cyclic voltammograms in pure FLiNaK and FLiNaK-LaF_3 systems, respectively. The cathodic/anodic limits at the left of the electrochemical window C1 and A1 correspond to the redox reaction of K (I)/K and this has been verified by Qiao et al [99] through the potential measurements of Li^+/Li, Na^+/Na, and K^+/K using alkali-metal electrodes in the FLiNaK melt. Different from the cyclic voltammogram obtained in pure FLiNaK molten salt, there is an extra pair of redox peaks C2 and A2 show up when LaF_3 was added into FLiNaK molten salt. A plateau P1 also appeared in the obtained chronopotentiogram (Figure 2-2 (b)) after LaF_3 was dissolved in. Thus, both cyclic voltammetry and chronopotentiometry tests show there is a redox reaction that occurs prior to the redox reaction of K (I)/K in FLiNaK-LaF_3 molten salt system.

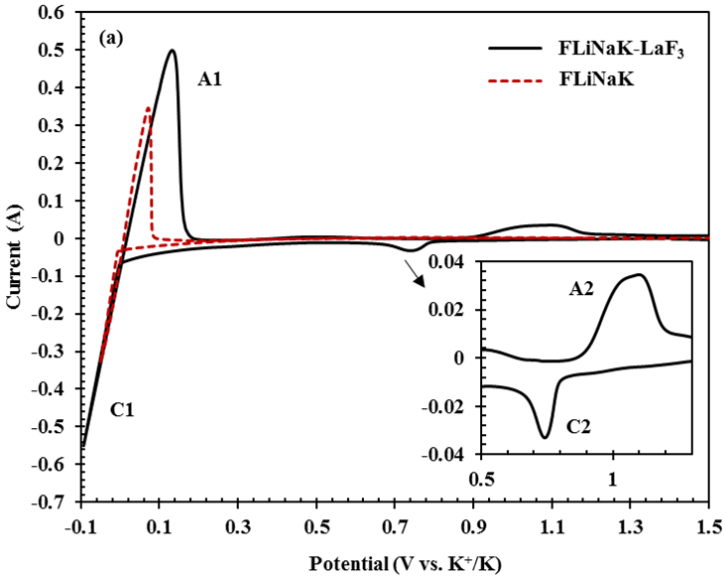

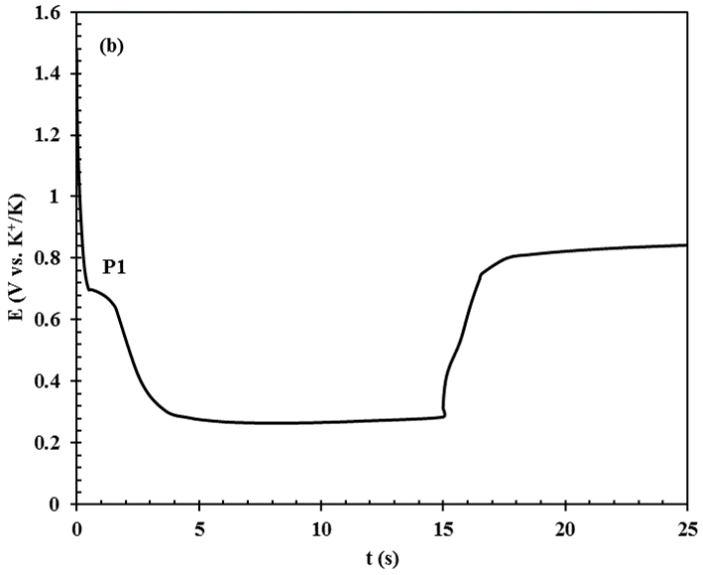

Figure 2-2. (a) Typical cyclic voltammograms obtained in FLiNaK-LaF_3 (working electrode area=0.673 cm^2) and pure FLiNaK molten salts at the scan rate of 100 mV/s. (b) Typical chronopotentiogram obtained in FLiNaK-LaF_3 molten salt with the applied current of -4 mA for 15s (working electrode area=0.673 cm^2). Working electrode: tungsten; counter electrode: tungsten; LaF_3=1.02 wt%; T=923 K.

In order to identify the reaction that occurs prior to the redox reaction of K (I)/ K, the chronopotentiometry electrolysis was performed by applying a reduction current of 2 mA on the tungsten working electrode for 3500s to obtain the reduction product. During this process, the open circuit potential was monitored and controlled such that the reduction potential of K (I) was guaranteed not to be reached. Figure 2-3 (a) shows the open circuit potential evolution with time when the reduction current was applied, from which it can be known that only the reduction reaction prior to that of K (I) occurs during the period when the current was applied. The electrode was taken out immediately after the chronopotentiometry electrolysis to do SEM test.

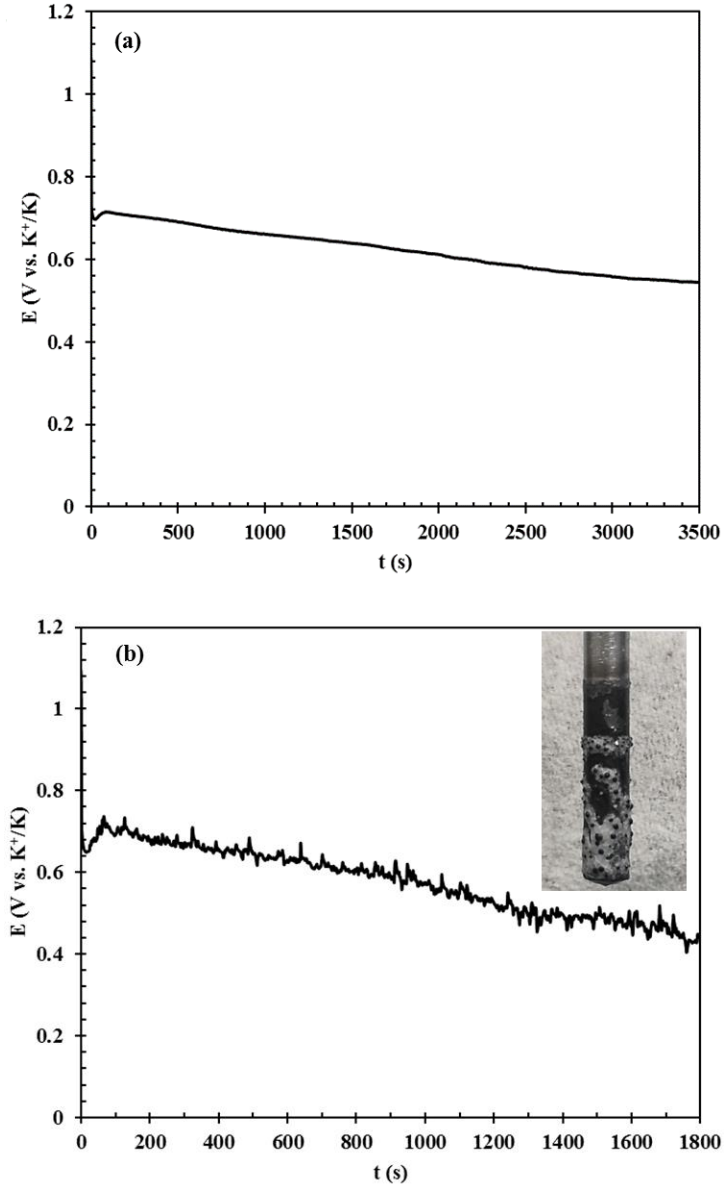

Figure 2-3. (a) Open circuit potential evolution with time when a stable reduction current of 2 mA was applied on the tungsten electrode in FLiNaK-LaF_3 molten salt for 3500s. Working electrode: tungsten (electrode area=1.186 cm^2); counter electrode: graphite; T=973 K; LaF_3=1.68 wt%. (b) Open circuit potential evolution with time when a stable reduction current of 6 mA was applied on the molybdenum electrode in FLiNaK-LaF_3 molten salt for 1800s. Working electrode: tungsten (electrode area=1.174 cm^2); counter electrode: graphite; T=973 K; LaF_3=3.45 wt%.

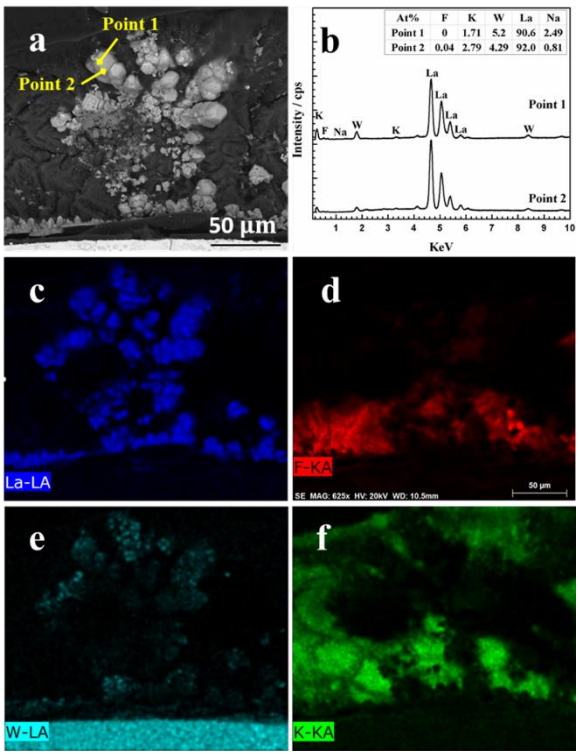

Figure 2-4. SEM results on the cross section of the tungsten electrode after chronopotentiometry electrolysis test.

Figure 2-4 shows the obtained SEM results on the cross section of the tungsten electrode after chronopotentiometry electrolysis test. Figure 2-4 (a) depicts the BSE image, from which it can be seen lots of lanthanum is concentrated at the center. The extremely weak signal of element F in the point scans of the lanthanum concentrated area indicates that the product produced is lanthanum metal. Additionally, the absence of element F in the lanthanum rich area as shown in the EDS mapping (Figure 2-4 (c-f)) illustrates the same result. Based on the results obtained from electrochemical techniques and SEM method, it can be known that the reduction reaction of La ion to La metal occurs prior to the reduction of K (I) in FLiNaK-LaF_3 molten salt. This investigation conflicts with the previous study by Qiao et al [93] in which they declared that the reduction reaction of lanthanum could not happen on inert electrode.

In the work by Qiao et al [93], the working electrode used was molybdenum not tungsten, therefore, the same electrochemical and SEM tests were also carried out on molybdenum working electrode in this study although the electrochemical behaviors on different kinds of inert working electrodes normally are expected to be the same. Figure 2-5 shows the obtained cyclic voltammogram and chronopotentiogram on molybdenum working electrode in FLiNaK-LaF_3 system from which the redox reduction of lanthanum can be observed to occur prior to that of potassium. Chronopotentiometry electrolysis was also performed on the molybdenum working electrode by applying a reduction current of 6 mA for 1800s to deposit lanthanum. Figure 2-3 (b) shows the open circuit potential evolution during the process of chronopotentiometry electrolysis from which it can be known the reduction potential of K (I) was not reached and only the reduction reaction of lanthanum

ion happened. The molybdenum working electrode was taken out immediately out from molten salt after chronopotentiometry electrolysis which is shown in Figure 2-3 (b) inserted picture from which it can be seen lots of substance deposited on it. Figure 2-6 presents the obtained SEM results on the molybdenum working electrode from which the lanthanum metal was also identified.

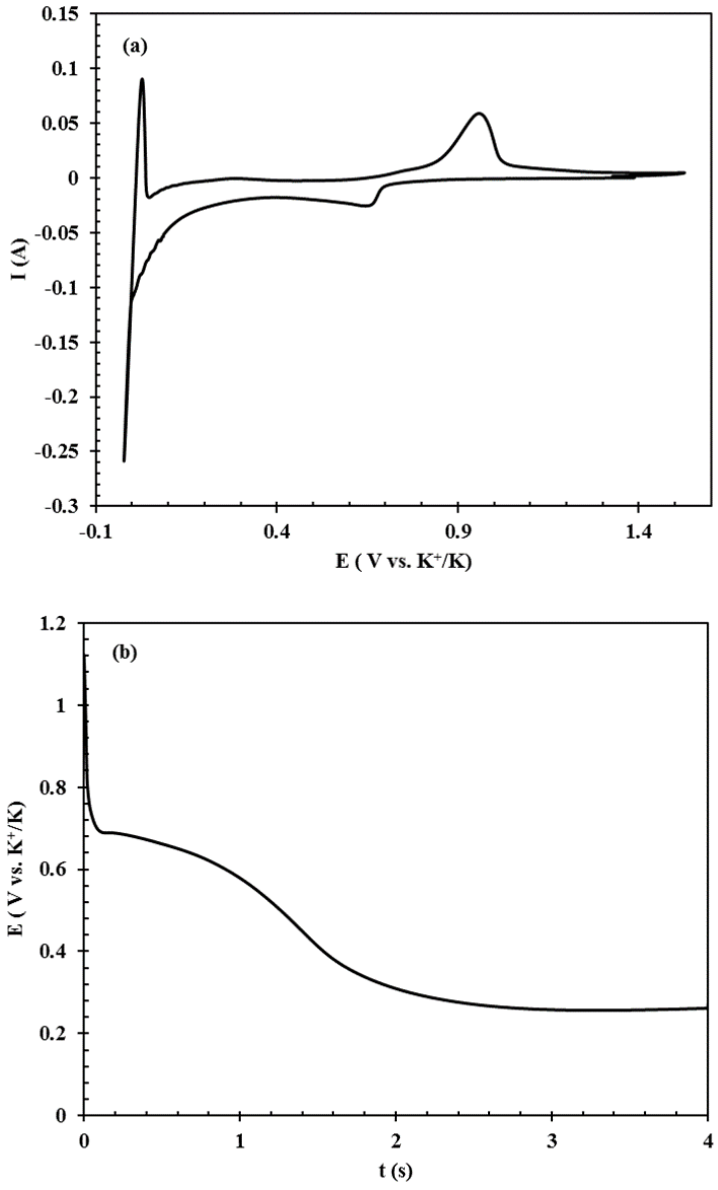

Figure 2-5. (a) Typical cyclic voltammograms obtained in FLiNaK-LaF_3 (working electrode area=1.273 cm^2) and pure FLiNaK molten salts at the scan rate of 200 mV/s. (b) Typical chronopotentiogram obtained in FLiNaK-LaF_3 molten salt with the applied current of -20 mA for 4s (working electrode area=1.273 cm^2). Working electrode: molybdenum; counter electrode: graphite; LaF_3=3.64 wt%; T=973 K.

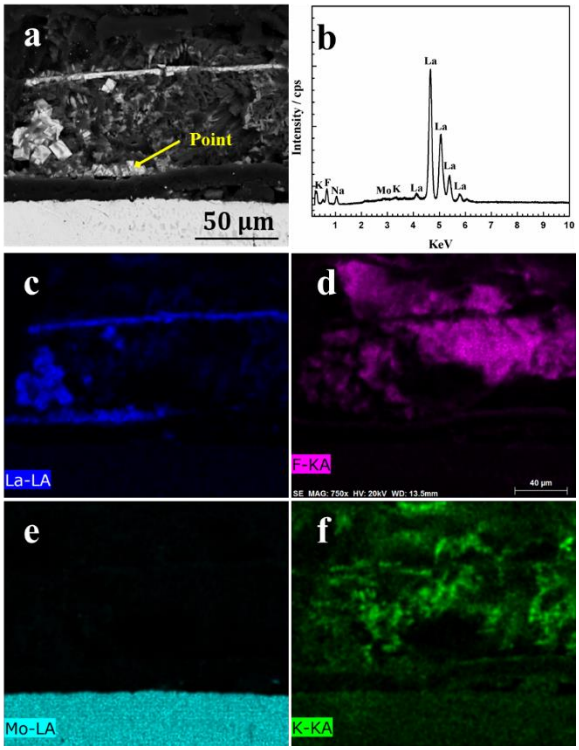

Figure 2-6. SEM results on the cross section of the molybdenum electrode after chronopotentiometry electrolysis test.

Based on the same results obtained on the tungsten and molybdenum working electrodes, it can be concluded that the reduction of lanthanum ion to lanthanum metal occurs prior to the reduction of K (I) to K metal and the electrochemical separation of lanthanum from FLiNaK molten salt can be realized by merely using an inert electrode. It is surprising that lanthanum can be separated out from FLiNaK molten salt since the standard reduction potential of La (III)/La is more negative than that of K(I)/K and other investigators except Chesser et al [94] always think that the deposition of La metal on inert electrode from FLiNaK-LaF_3 system is impossible [93,100].

In addition to inert electrodes, reactive electrode Ni was also used for the electrochemical separation study of LaF_3 in FLiNaK molten salt. Figure 2-7 shows the obtained cyclic voltammogram obtained on Ni working electrode at 973 K in which some extra redox peaks closing to the redox peaks of K^+/K were indicated. It corresponds to the La-Ni intermetallic compound formation and dissolution process. In order to find out the formed intermetallic compound between La and Ni, an electrolysis was performed by applying a reduction current of 10 mA for 1 hour and the Ni working electrode after electrolysis was taken out for SEM analysis. Figure 2-8 shows the obtained SEM result in which the La metal was identified, it should be attributed to the reduction occurring at the left side of the electrochemical window shown in Figure 2-7. No intermetallic compound was formed, it is probably because more energy or time is needed for La-Ni intermetallic compound formation during the electrolysis process.

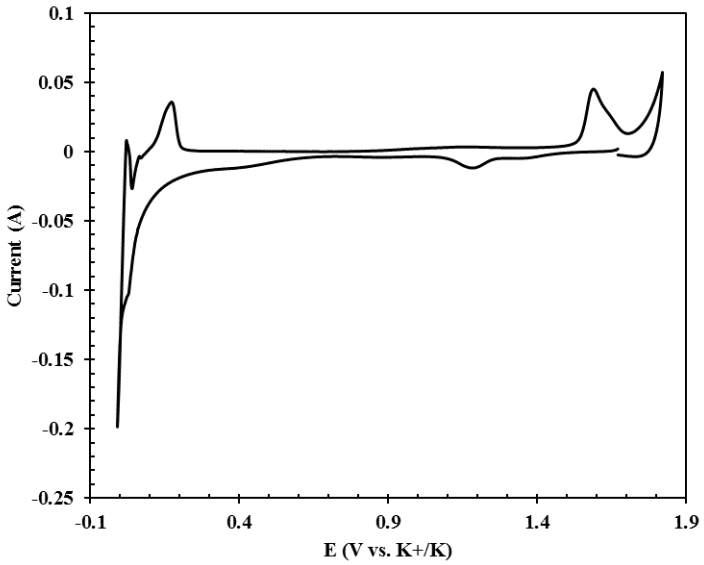

Figure 2-7. Typical cyclic voltammograms obtained in FLiNaK-LaF_3 on Ni electrode (working electrode area=1.295 cm^2) at 973 K.

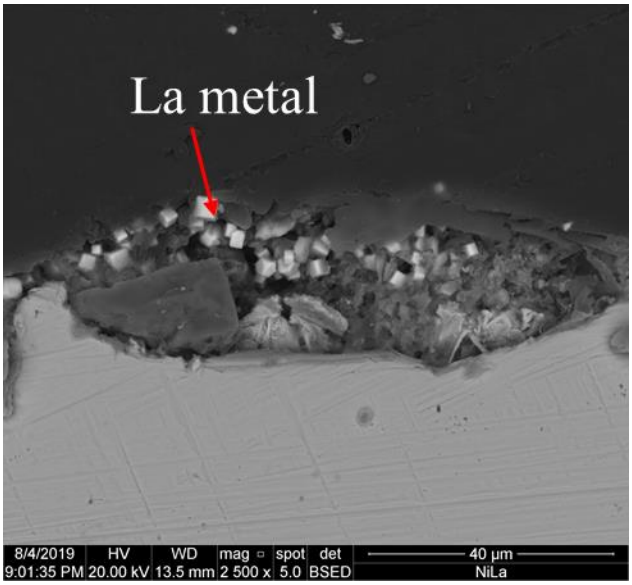

Figure 2-8. SEM analysis on the cross section of the Ni working electrode after electrolysis.

2.4. The reason of the achievement on the electrochemical separation of lanthanum in FLiNaK molten salt by inert electrodes

To find out the reason for the phenomenon that electrochemical separation of lanthanum from FLiNaK molten salt can be achieved by merely using an inert electrode, a series of investigations were carried out. It is found that lanthanum predominantly exists in the species of LaF_6^{3-} instead of La^{3+} in LaF_3-KF [101] and NaF-LiF-LaF_3 [102] salts at the liquid states. The XRD analysis (Figure 2-10) of the quenched LiF-KF-LaF_3 molten salt (2.73 wt% LaF_3 dissolved in eutectic LiF-KF molten salt) at room temperature in our study also indicates the existence of LaF_6^{3-}. It means lanthanum species will exist in the form of

LaF_6^{3-} when NaF or KF appears in molten fluoride salt. In that case, the redox reaction for La in KF-containing molten fluoride salts, for example, would be

$$K_3LaF_6 \leftrightarrow 3KF + La + \frac{3}{2}F_2 \tag{2-1}$$

Comparing with the redox reaction of LaF_3/La, the standard reduction potential $E^o_{K_3LaF_6/La}$ for redox reaction K_3LaF_6/La can be expressed by

$$E^o_{K_3LaF_6/La} = E^o_{LaF_3/La} + \frac{\Delta G(K_3LaF_6)}{nF} \tag{2-2}$$

where $\Delta G(K_3LaF_6) = G(K_3LaF_6) - 3G\ (KF) - G(LaF_3)$, $E^o_{LaF_3/La}$ is the standard reduction potential for redox reaction LaF_3/La. Providing the value on $\Delta G(K_3LaF_6)$ which is reported as 295 KJ/mol in the previous literature [103], the electrodeposition potential for La will shift positively by 1.02 V (Figure 2-9).

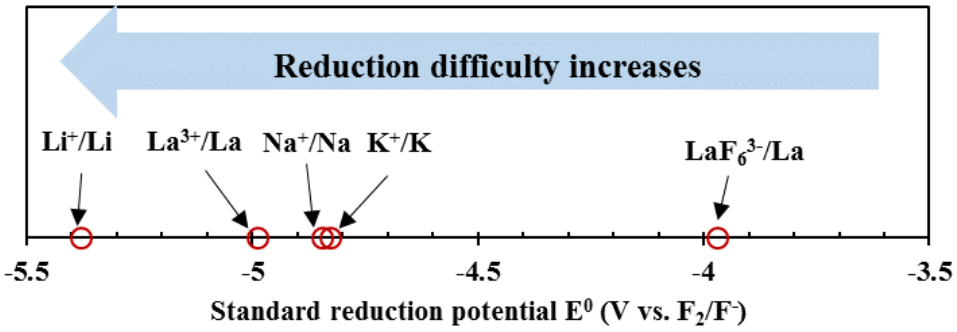

Figure 2-9. Calculated standard reduction potentials of LaF_3/La, LiF/Li, NaF/Na, KF/K and K_3LaF_6/La.

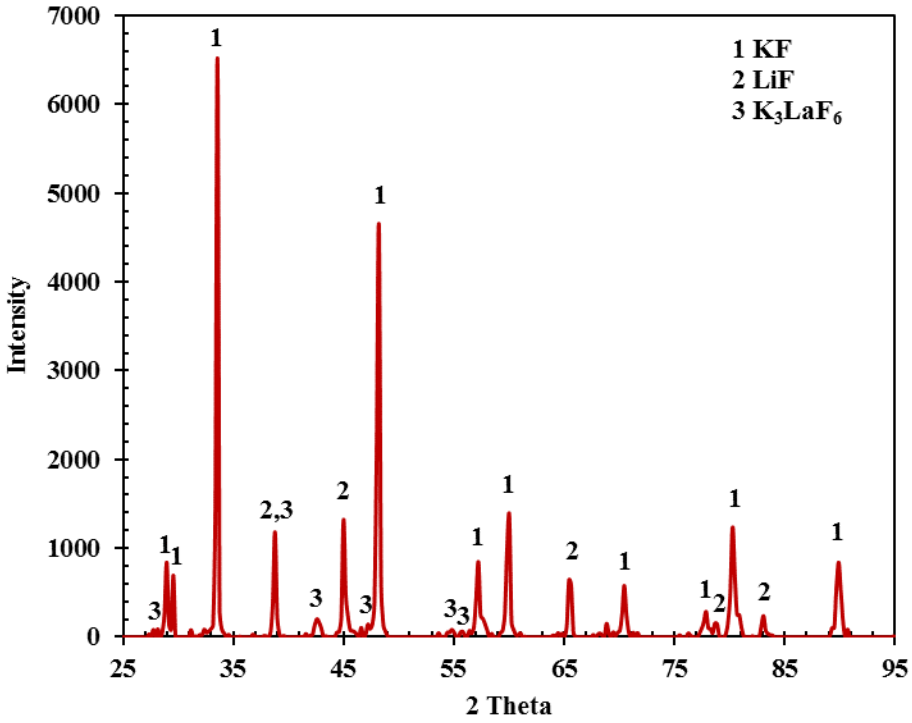

Figure 2-10. XRD analysis result of the quenched eutectic LiF-KF-2.73 wt% LaF_3 molten salt.

Based on the discuss above, the presence of KF or NaF will result in the formation of LaF_6^{3-} and the electrodeposition of La from molten fluoride salts will be much easier. The electrochemical behaviors of La in molten LiF, LiF with the addition of KF, and LiF with the addition of NaF were investigated to confirm our theory, respectively.

The typical cyclic voltammograms of LiF and LiF-LaF_3 recorded on Mo working electrode are shown in Figure 2-11. The result obtained in pure LiF shows no obvious peak in the sweep range between -1.7 V and 0.5 V (vs. Pt), proving the absence of electrochemical reactions. The sharpness of the reduction current at -1.7 V (vs. Pt) should be attributed to the reduction of Li (I). In addition to the redox peaks of Li (I)/Li, the cyclic voltammogram shows a new pair of redox peaks when LaF_3 was dissolved in molten LiF salt, which should be attributed to the reaction of La (III) ↔La [104]. The cyclic voltammetry result obtained on inert Mo electrode also indicates that the electrodeposition of La metal proceeds just prior to the solvent reaction (Li (I)/Li), which is in accordance with the thermodynamic calculation in Figure 2-9.

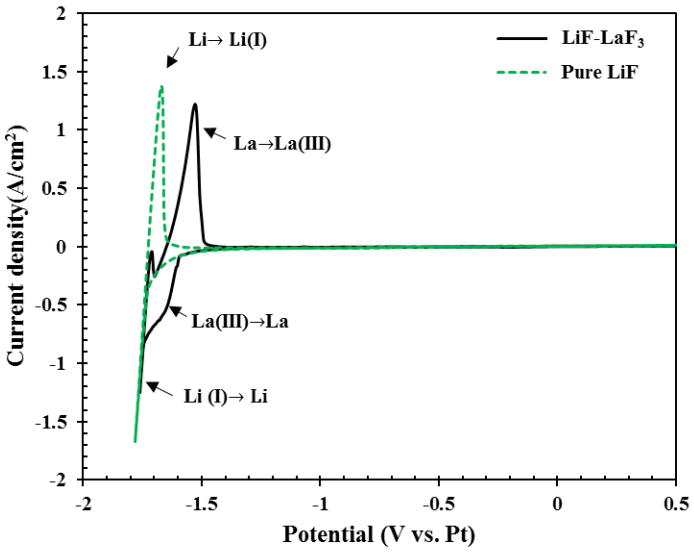

Figure 2-11. Cyclic voltammograms obtained in LiF-LaF_3 and pure LiF molten salts. Scan rate: 100 mV/s; working electrode: Mo; counter electrode: graphite; LaF_3=3.33 wt%; T=1173 K.

As calculated in Figure 2-9, with the addition of either KF (or NaF) into molten LiF, the formation of K_3LaF_6 (or Na_3LaF_6) allows the electrodeposition of La proceeds at a considerably more positive potential [101,102]. To verify this prediction, the electrochemical tests were carried out in LiF-LaF_3 molten salt system with KF added and the results are shown shown in Figure 2-12. The cyclic voltammogram curve obtained in the eutectic LiF-KF (Figure 2-12a, dash line) illustrates no redox peak in the potential range from -1.4 V to 0.4 V (vs. Pt). According to the standard reduction potential shown in Figure 2-9, the reduction of K(I) is easier to occur than that of Li (I) in fluoride salts. Thus, the cathodic and anodic limit C1 and A1 at the left side of the electrochemical window should be attributed to the redox reaction of K (I)/K. A new reduction peak C2 at -0.75 V (vs. Pt) appears after the addition of LaF_3 (*Figure 2-12*a, solid line) which should be attributed to the electrodeposition of La. Comparing with the electrodeposition potential of La in LiF-LaF_3 shown in Figure 2-11, the positive shift on potential caused by the addition of KF is about 1.0 V, which is in good agreement with the calculated results in Figure 2-9. In addition to the cyclic voltammetry test, the chronopotentiometry was performed, the plateau P1 in the obtained chronopotentiogram shown in Figure 2-12b also indicates a great positive shift on the electrodeposition potential of La after KF was added in.

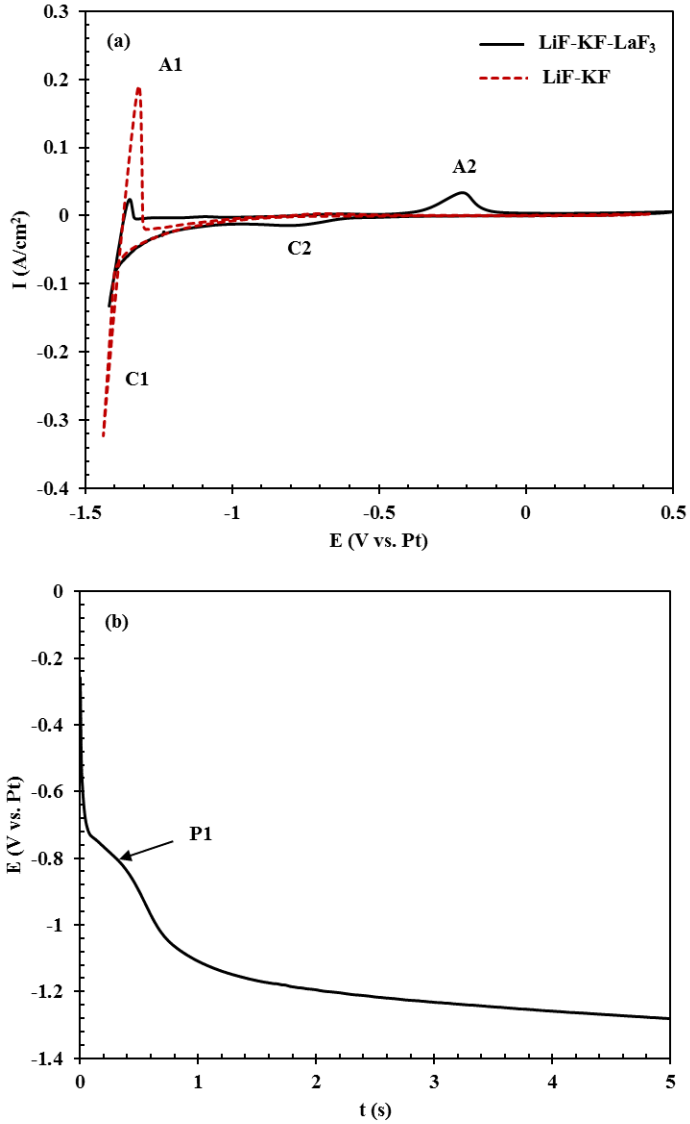

Figure 2-12. (a) Cyclic voltammograms obtained in LiF-KF eutectic molten salt with LaF_3 dissolved in and pure LiF-KF eutectic molten salt at the scan rate of 200 mV/s. (b) Chronopotentiogram of the system of LiF-KF-LaF_3 with the applied current of -50 mA (working electrode area=2.24 cm^2). Working electrode: Mo; counter electrode: graphite; LaF_3=2.73 wt%; T=973 K.

To further confirm the electrodeposition of La, a stable current of -4 mA was provided for 1800s on a Mo working electrode to do chronopotentiometry electrolysis in the LiF-KF eutectic molten salt with 2.73 wt% LaF_3 dissolved in. The cathode potential was monitored and controlled to not reach the reduction potential of alkali species during the electrolysis process. The Mo electrode was taken out from the electrochemical cell immediately after chronopotentiometry electrolysis for subsequent SEM analysis. Figure 2-13 shows the SEM results of the cross section of the polished Mo rod electrode after chronopotentiometry electrolysis. The backscattered electrons (BSE) image was shown in Figure 2-13a in which the gray bottom part and the top black part is Mo electrode and

solidified salt, respectively. Plenty of La was accumulated after electrolysis which can be seen in the middle of the image as shown in Figure 2-13 (a). The point scans of the La rich part show the signal for La element is very strong while it is extremely weak for the element of F. It means the substance deposited is La metal. Figure 2-13 (c-f) shows the EDS mapping results from which the absence of F at the place where La is concentrated can be observed and it further confirms that the deposited material after chronopotentiometry electrolysis is La metal.

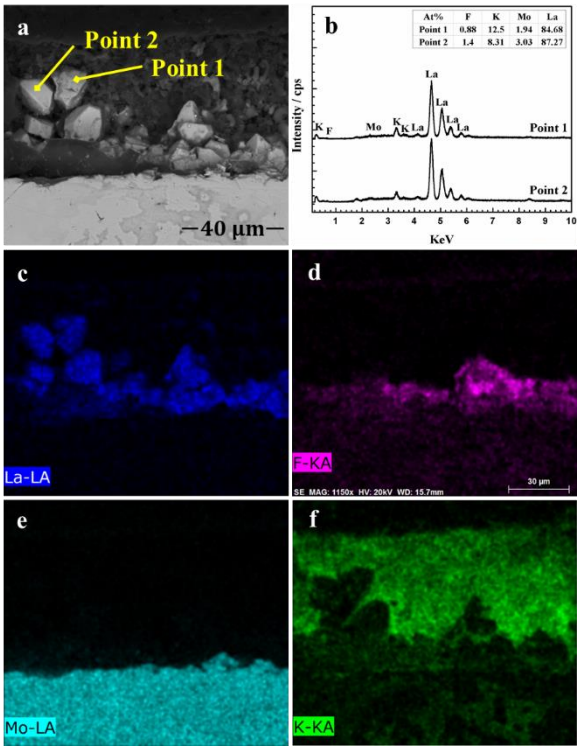

Figure 2-13. (a) Backscattered electrons (BSE) image of the cross section of polished Mo rod electrode after electrolysis in LiF-KF-LaF_3 molten salt; (b) EDS point scan results of point 1 and point 2 in Figure 2-13a; (c)-(f) EDS mapping results of Figure 2-13a.

Similarly, electrochemical tests were also carried out in LiF-LaF_3 molten salt system with the addition of NaF. Figure 2-14 shows the cyclic voltammogram and chronopotentiogram obtained on Mo working electrode in the LiF-NaF-LaF_3 molten salt system. Based on the calculation in Figure 2-9, the peak C1 in the CV test (Figure 2-14a) and P2 in chronopotentiometry test (Figure 2-14b) should be attributed to the reduction of Na (I). With the addition of NaF, a pair of redox peaks (peak C2 and A2) was observed in just the way that the electrochemical behavior of the system was recorded when KF was added. The reduction peak of C2 should be the electrodeposition of La metal while the oxidation peak A2 is the oxidation process of the deposited La. Also, a plateau P1 in (Figure 2-14 (b)) can be seen, which should be related to the deposition of La metal. The same process was conducted as done in LiF-KF-LaF_3 system in which a stable current of -4 mA was applied on the Mo rod electrode for 1800s to do chronopotentiometry electrolysis in the LiF-NaF eutectic molten salt with 3.02 wt% LaF_3 dissolved in. Then the Mo rod electrode

was polished and a SEM test was performed on its cross section. Figure 2-15 shows the obtained SEM results. It can be identified that the element F rarely exists in the La rich locations, which indicates the product produced by the electrolysis is La metal. A strong signal of La can also be observed in the point scans of the La concentrated part. Some amounts of F were also found in the point scans which could be attributed to the salt stuck to the La metal surface.

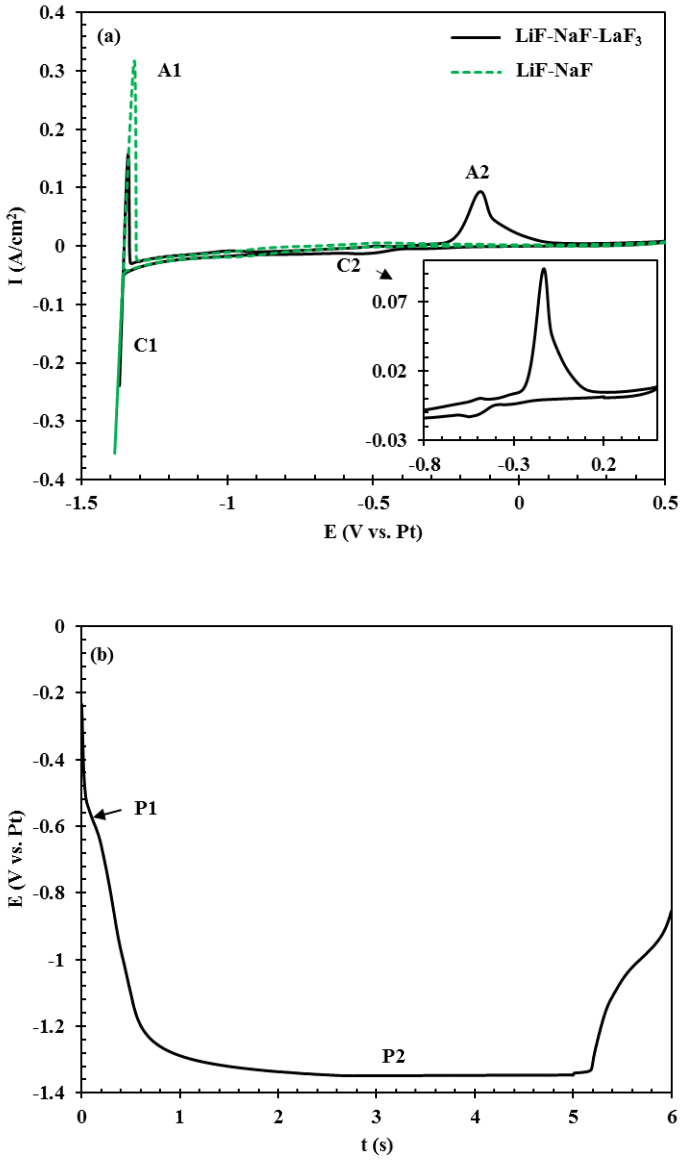

Figure 2-14. (a) Cyclic voltammograms obtained in LiF-NaF eutectic molten salt with LaF_3 dissolved in and pure LiF-NaF eutectic molten salt at the scan rate of 200 mV/s. Insert photograph: the enlargement of the CV curve obtained in LiF-NaF-LaF_3 salt; (b) Chronopotentiogram of the system of LiF-NaF-LaF_3 with the applied current of -20 mA (working electrode area=0.577 cm^2). Working electrode: Mo; counter electrode: graphite; LaF_3=3.02 wt%; T=1023 K.

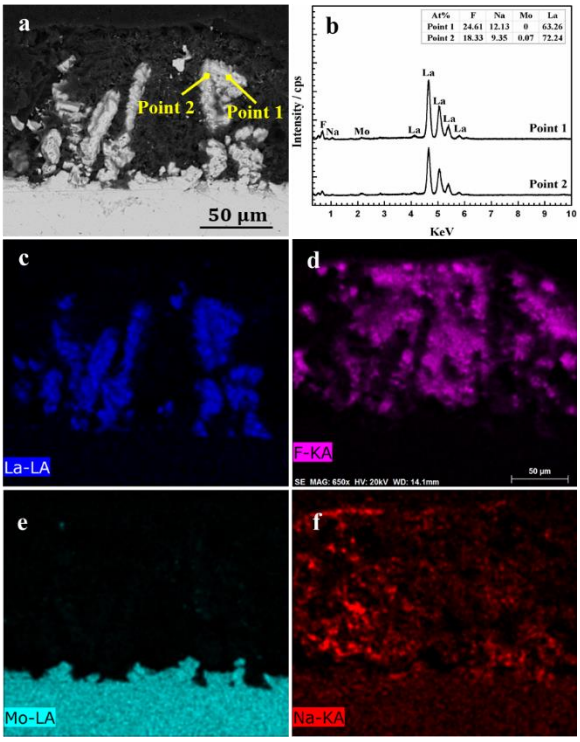

Figure 2-15. (a) Backscattered electrons (BSE) image of the cross section of polished Mo rod electrode after electrolysis in LiF-NaF-LaF_3 molten salt; (b) EDS point scan results of point 1 and point 2 in Figure 2-15a; (c)-(f) EDS mapping results of Figure 2-15a.

Based on the discusses above, it can be concluded that the formation of LaF_6^{3-} make the electrochemical separation of lanthanum from FLiNaK molten salt by inert electrode be possible. In addition, the finding that the extraction of La from molten fluoride salt can be assisted by KF or NaF will provide a new method for the electrochemical separations of stubborn elements.

2.5. Electrochemical investigation of CeF_3 in molten FLiNaK salt on W, Cu, and Ni electrodes

2.5.1. Electrochemical behavior of CeF_3 in FLiNaK melt on W electrode

The typical cyclic voltammograms on W working electrode for FLiNaK and FLiNaK-CeF_3 are shown in Figure 2-16 (a). The cathodic limit at the left of the electrochemical window is the deposition of K (I), which has been verified by Qiao et al [99] through the potential measurements of Li (I)/Li, Na (I)/Na, and K (I)/K using each alkali-metal electrode in the FLiNaK melt. Different from the result obtained from blank FLiNaK molten salt, an extra pair of redox peaks C1/A1 shows up when a small amount of CeF_3 is added into FLiNaK molten salt. The redox reaction C1/A1 was focused and several cyclic voltammetry cycle scans were performed as shown in Figure 2-17. It is noted that two pre-reduction peaks show up from the second cycle and become more pronounced after each cycle scan. The similar phenomenon has also been observed in the previous study [105], however, the

reason for this is still not well understood. Chronopotentiometry test was carried out in FLiNaK-CeF_3 molten salt system as well. The obtained chronopotentiogram is shown in Figure 2-16 (b) in which a plateau P1 is indicated. It is found that the peak current density in the obtained cyclic voltammogram is especially small, and the transition time in the chronopotentiogram is very short although a small current was applied.

Cyclic voltammetry tests were carried out when two different amounts of CeF_3 were added into FLiNaK molten salt. As shown in the enlarged plot inserted in Figure 2-16 (a), only a slight difference was observed on the obtained redox peaks in FLiNaK-2.93 wt% CeF_3 and FLiNaK-5.93 wt% CeF_3 molten salts and the peak current density at lower concentration even present a higher value. In addition, there is a shoulder with the oxidation peak A1 for the cyclic voltammogram at higher concentration while not for the lower concentration. Repeat cyclic voltammetry tests were performed for both the high and low concentrations. The obtained results are shown in Figure 2-18 where the shoulder is observed for both of these two different concentrations. Therefore, the shoulder should result from the effect of the electrode such as the roughness or the desorption effect of the oxidation reaction. Considering the redox peaks C1/A1 only show up when CeF_3 was added into FLiNaK molten salt, this redox reaction must be related to Ce. However, based on the thermodynamic calculation shown in Figure 2-1, this pair of redox peaks could not be attributed to redox reaction of Ce (III)/Ce because of the more cathodic standard reduction potential than that of K(I)/K. Moreover, no increase on the peak current density of cyclic voltammogram with the addition of more CeF_3 into FLiNaK molten salt also reflects that the redox peaks do not result from the redox reaction of Ce (III)/Ce.

To identify this redox reaction, a potentiostatic electrolysis was conducted in FLiNaK-2.93 wt% CeF_3 molten salt by applying a voltage of 0.5 V (vs. K^+/K) for 3600 s. The W working electrode was taken out from the electrochemical test cell right after the potentiostatic electrolysis and SEM analyses were performed on it. Figure 2-19a depicts the backscattered electrons (BSE) image of the cross section of the polished tungsten rod electrode after electrolysis, of which the white bottom part and black top part are tungsten electrode and epoxy, respectively. At the center of Figure 2-19a, lots of Ce is accumulated. Figure 2-19 (b-d) shows the EDS mapping results in which the absence of F at the place where Ce is concentrated can be observed and it indicates the deposit product after electrolysis is Ce metal. SEM and EDS analyses were also performed on the cross section of the W electrode in a small magnification and the results were shown in Figure 2-20. From which, deposited Ce metal was also observed along the electrode. Based on all the evidence we have now, it is suspected that the reduction peak C1 may be attributed to the reduction of the small amount of Ce component ions formed by Ce and impurity ions such as oxide ions or hydroxide ions. The formation of the component ions greatly shifts the electrodeposition potential of Ce metal to a more positive value. The oxidation peak A1 should correspond to the oxidation of Ce metal to the Ce component ions. Based on the small peak current density in cyclic voltammogram which is probably due to the small amount of the formed Ce component ions in FLiNaK molten salt, Ce metal cannot be extracted out on a large scale.

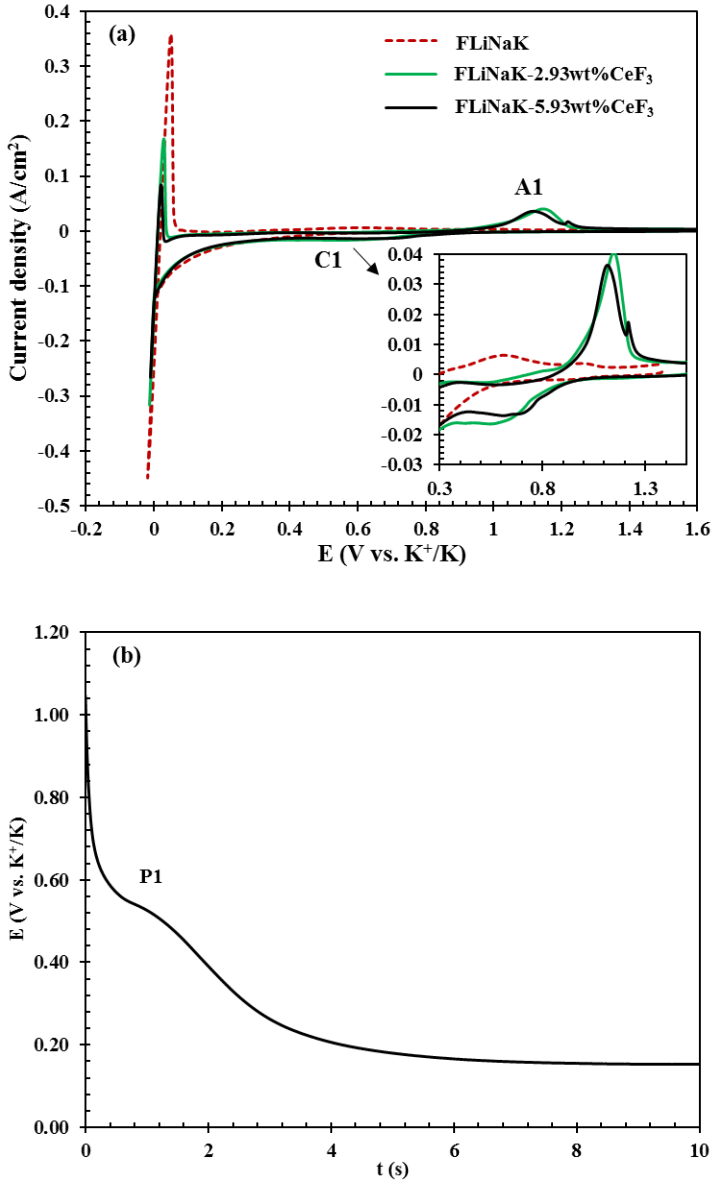

Figure 2-16. (a) Cyclic voltammograms obtained in FLiNaK-CeF_3 and blank FLiNaK salt melt at the scan rate of 200 mV/s. (b) Chronopotentiogram of the system FLiNaK-CeF_3 (CeF_3=2.41 wt%) with the applied current of -10 mA (working electrode area=0.698cm^2). Working electrode: W; counter electrode: graphite; T=973K.

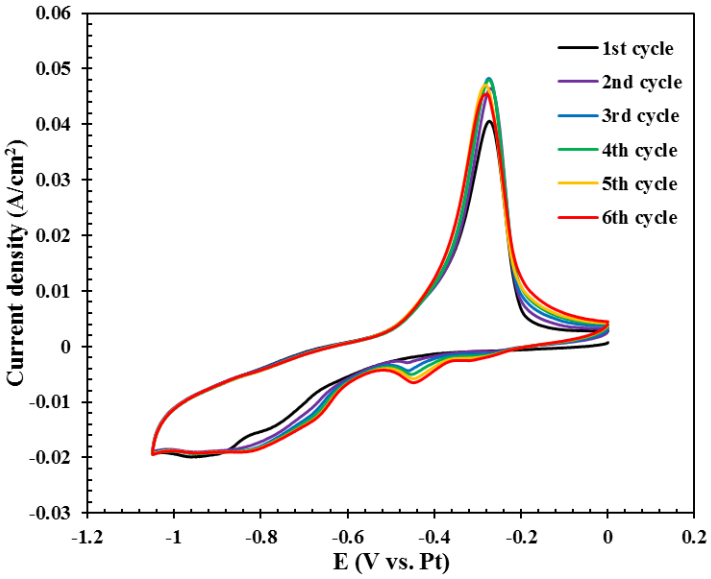

Figure 2-17. Several cyclic voltammetry cycle scans for redox reaction C1/A1.

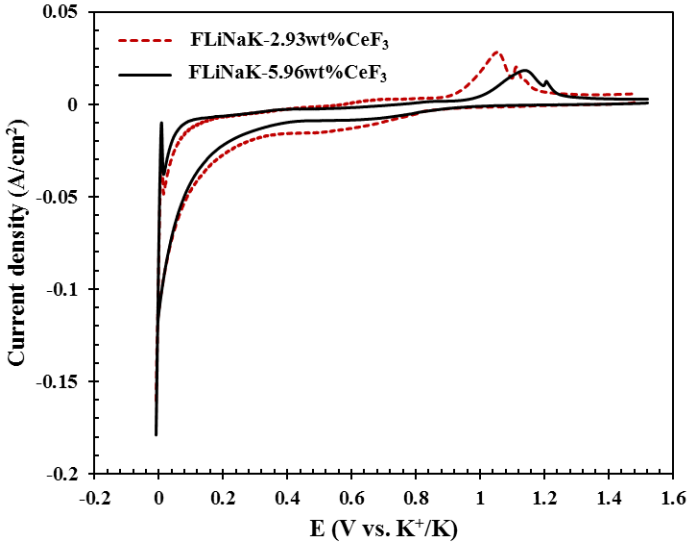

Figure 2-18. Cyclic voltammograms obtained in FLiNaK-CeF_3 at the scan rate of 200 mV/s. Working electrode: W; counter electrode: graphite; T=973K.

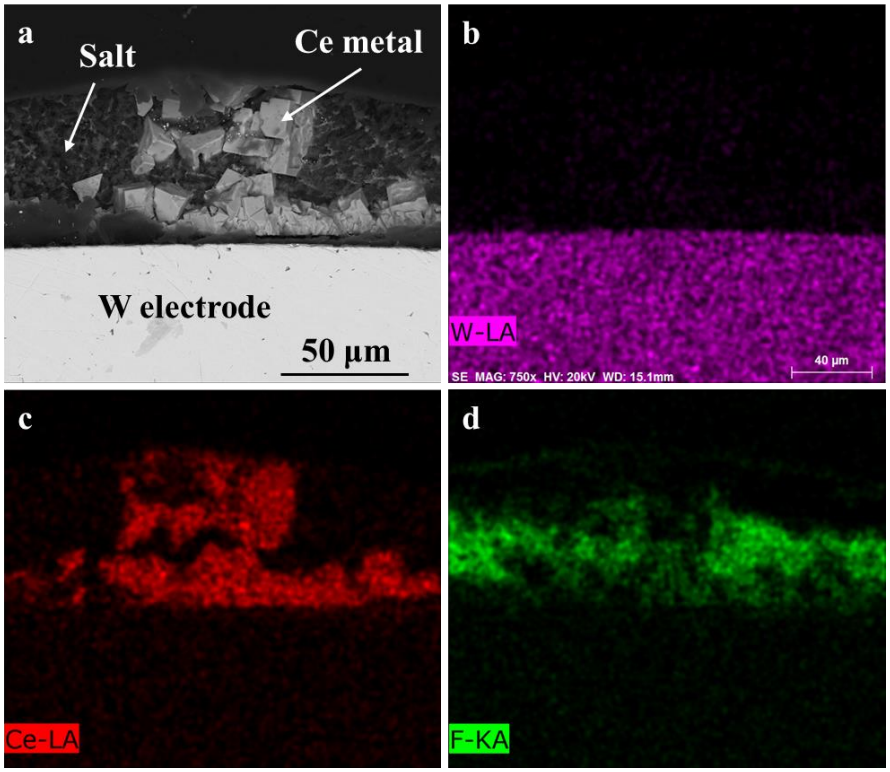

Figure 2-19. (a) Backscattered electrons (BSE) image of the cross section of polished tungsten rod electrode after electrolysis; (b)-(d) EDS mapping results of Figure 2-19a.

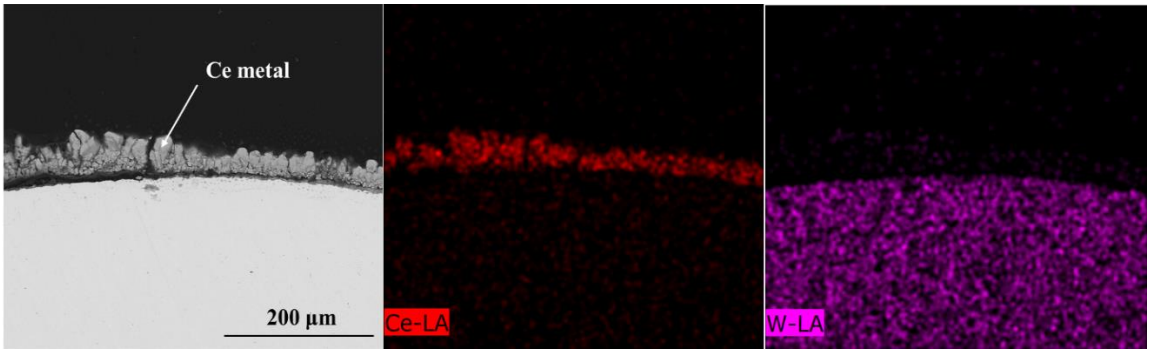

Figure 2-20. SEM analysis on the W electrode after potentiostatic electrolysis.

2.5.2. Electrochemical behavior of CeF_3 in FLiNaK melt on Cu and Ni working electrodes

The electrochemical study of CeF_3 in FLiNaK on W electrode indicates that Ce probably cannot be efficiently separated out from FLiNaK molten salt by using an inert electrode because of the small electrodeposition current density. The use of solid reactive electrode can help shift the electrodeposition potential of Ce to a less cathodic value through the formation of an intermetallic compound. When using a reactive electrode, B, the electrochemical deposition reaction of Ce^{3+} on it can be written as

$$xCe^{3+} + 3xe^{-} + yB \leftrightarrow Ce_xB_y \qquad (2\text{-}3)$$

where Ce_xB_y is the formed intermetallic compound between Ce and reactive electrode *B*. Then the equilibrium potential of Ce^{3+}/Ce_xB_y is

$$E_{Ce^{3+}/M_xB_y} = E_{Ce^{3+}/Ce} - \frac{1}{x}\frac{\Delta G(Ce_xB_y)}{3F} \quad (2\text{-}4)$$

where $E_{Ce^{3+}/Ce}$ is the equilibrium potential when pure *Ce* is deposited on an inert electrode, $\Delta G(Ce_xB_y)$ is the Gibbs free energy of formation of compound Ce_xB_y. The value of E_{Ce^{3+}/Ce_xB_y} will be more positive than $E_{Ce^{3+}/Ce}$ as the value of $\Delta G(Ce_xB_y)$ is negative. Thus, the formation of intermetallic compound between Ce and a reactive electrode allows Ce ions to be reduced at a potential less cathodic than that for the deposition of a pure metal. Ni and Cu are the two most popular reactive electrodes for the electrochemical separations of stubborn fission products in molten fluoride salts because of their high temperature tolerance [106]. With Ni and Cu metals, Ce can form several intermetallic compounds while alkali metal (K, Li, Na) cannot [107]. Thus, the deposition potential of Ce will move to a less cathodic value and then may be separated out at a potential which is less cathodic than the reduction potential of K (I)/K by using Ni and Cu as the working electrodes.

Before performing the electrochemical test on Ni and Cu electrodes, the intermetallic compounds formed between Ce and these two reactive electrodes, the Gibbs free energy of formation of the formed intermetallic compounds, and the potential shift calculated based on equation (2-4) are summarized in Table 2-1. From which it can be known a greater positive potential shift can be obtained when using Ni electrode compared with the use of Cu electrode. Among all the intermetallic compounds that could be formed, $CeNi_5$ is the one which can bring the greatest positive potential shift.

Table 2-1. The Gibbs free energy of formation of the formed intermetallic compounds and the corresponded potential shift when using Ni and Cu reactive electrodes to separate Ce at 973 K.

Reactive electrode	Intermetallic compound	G_f (J/mol)	Electron transfer number	Potential shift (V)
Ni [52]	Ce_7Ni_3	-219846	3	0.109
	CeNi	-66022		0.228
	$CeNi_3$	-133040		0.460
	Ce_2Ni_7	-290625		0.502
	$CeNi_5$	-173488		0.599
Cu [60]	$CeCu_6$	-78147	3	0.270
	$CeCu_5$	-71827		0.248
	$CeCu_4$	-64779		0.224
	$CeCu_2$	-50010		0.173
	CeCu	-26564		0.092

Electrochemical test was first carried out on a Cu working electrode to identify the feasibility of the separation of Ce. Figure 2-21 shows the cyclic voltammogram of FLiNaK-CeF_3 on a Cu working electrode. It can be observed that there is a pair of redox peaks that show up prior to K (I)/ K which is the same as the results obtained when W is used as the working electrode. No intermetallic compound formation was found and the reason for this phenomenon could attribute to that the Gibbs free energy of formation of Ce_xCu_y is not enough to shift the intermetallic compound deposition potential to a more anodic value than that of K (I)/K. As shown in Figure 2-1, the standard reduction potential difference between Ce (III)/Ce and K(I) /K is around 0.1 V. If the activity of K (I) in FLiNaK molten salt is assumed to be 0.42 (the mole fraction of KF in FLiNaK) while that of Ce (III) is assumed to be 10^{-5} which is the typical value in molten chloride salt at the concentrations studied in the present work [108], then the equilibrium reduction potential difference between Ce (III)/Ce and K(I) /K is around 0.33 V. Therefore, the largest potential shift of 0.27 V brought by Cu reactive electrode as listed in Table 2-1 is probably not enough to make the Ce separate out from FLiNaK molten salt.

Potentiostatic electrolysis was also carried out on the Cu working electrode by setting a voltage of 0.5 V (vs. K^+/K) for 3600 s. The electrode was taken out immediately after the test for SEM and EDS analyses. Figure 2-13a shows the backscattered electrons (BSE) image of the cross section of copper rod electrode where an evident grey strip layer can be clearly seen. In EDS mapping analysis (Figure 2-13b-d), fluorine element is obviously absent in the Ce strip layer. It means the reduction product after electrolysis is Ce metal and this result is consistent with the one obatined on W electrode. At the same time, no overlapping of copper and cerium is found which demonstrates the absence of intermetallic compound between cerium and copper metal. SEM and EDS analyses in small magnifications were also performed on the cross section of the Cu electrode and the results are shown in Figure 2-23 in which deposited Ce metal was also observed along the electrode. This phenomenon is very interesting since intermetallic compound formation generally occurs in the potential prior to the pure metal deposition. However, no intermetallic compound formation was found in both the electrochemical tests and SEM analyses although the Ce metal deposition was found. The reason is probably that the Ce component ions formed by Ce and impurity ions is too few and the current arisen from the reduction reaction is too small to drive the Ce to diffuse into Cu and further form intermetallic compounds.

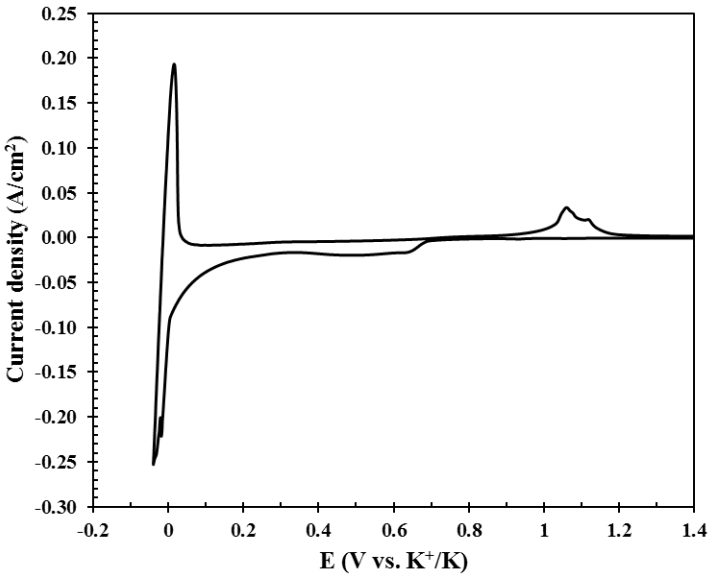

Figure 2-21. Cyclic voltammogram of CeF_3 in FLiNaK molten salt recorded on Cu working electrode. Counter electrode: graphite; CeF_3=1.37 wt%; T=973K; Scan rate: 100 mV/s.

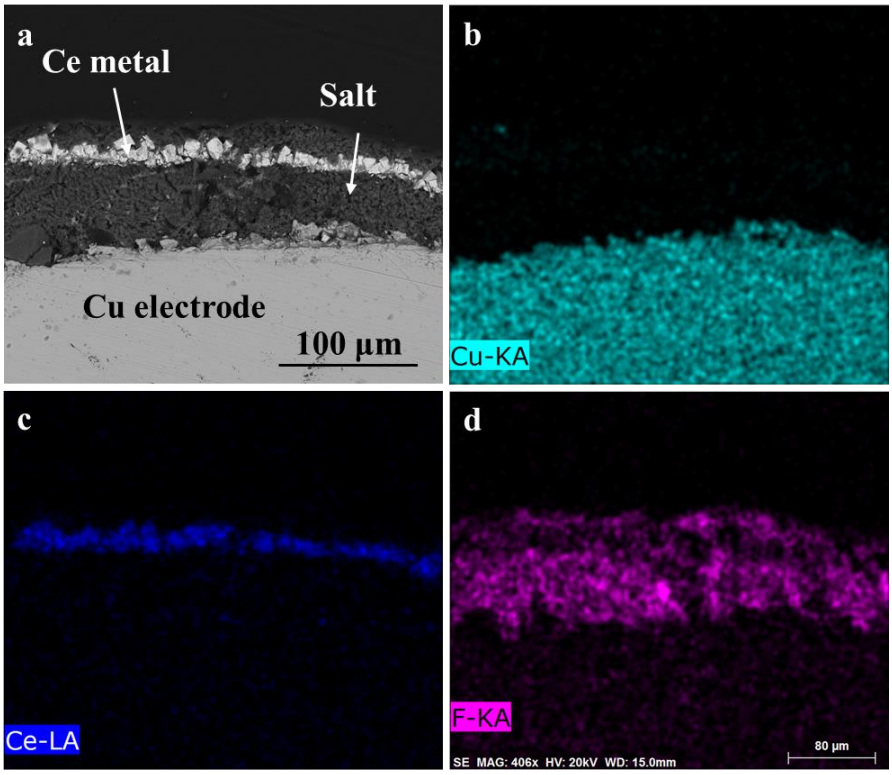

Figure 2-22. (a) Backscattered electrons (BSE) image of the cross section of polished copper rod electrode after electrolysis; (b)-(d) EDS mapping results of Figure 2-13a.

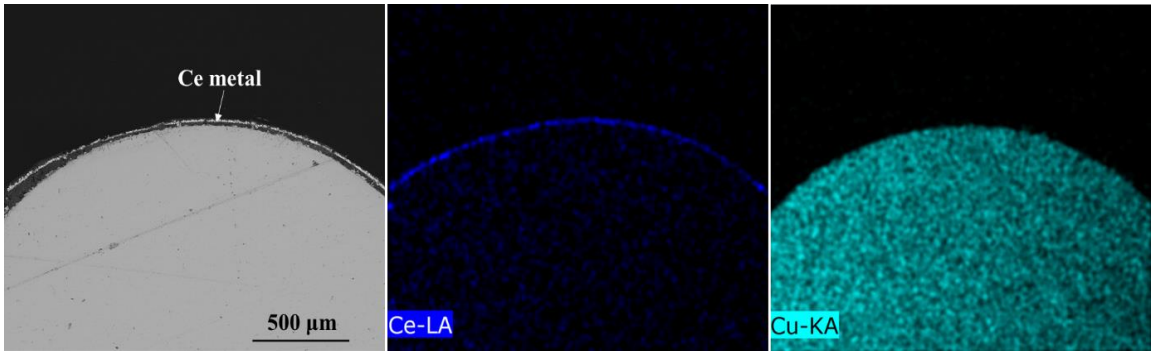

Figure 2-23. SEM analysis on the Cu electrode after potentiostatic electrolysis.

Electrochemical test was also performed on a Ni working electrode. Figure 2-24 shows the typical cyclic voltammogram of FLiNaK-CeF_3 molten salt system recorded on the Ni working electrode at the temperature of 973 K. Different from the results obtained on W and Cu electrode, several extra cathodic and anodic peaks are observed prior to the redox reaction of K (I)/K. In order to find out the cathodic peaks and their corresponding anodic peaks, several cyclic voltammetry tests at various switching potentials were subsequently conducted and the results are shown in Figure 2-25. Similar to the cyclic voltammogram recorded on W and Cu electrode, cathodic peak C_I and anodic peak A_I were also observed at the right side of the electrochemical window. It should be noticed that the position of A_I shifts slightly when setting different switching potentials which may be due to the surface change on the working electrode when intermetallic compound is formed. Cathodic peak C_{II} corresponds to an intermetallic compound formation between Ni and Ce. Only one anodic peak A_{II} can be observed when the switching potential is set to be 0.05 V (vs. K^+/K) whereas, two anodic peaks A_{II} and A_{III} are indicated when the switching potential of 0.01 V (vs. K^+/K) is applied. It means the dissolution of the formed intermetallic Ce-Ni compound when more Ce is deposited could be multi-step reactions. The same phenomenon was also observed in the LiF-CaF_2-CeF_3 system on Ni working electrode [109]. Figure 2-25 also shows the potentials of oxidation peaks A_{II} and A_{III} shift to a more anodic value slightly when the switching potential is set to a more cathodic value. It is probably because more Ce-Ni intermetallic compound is formed when a more cathodic switching potential is set.

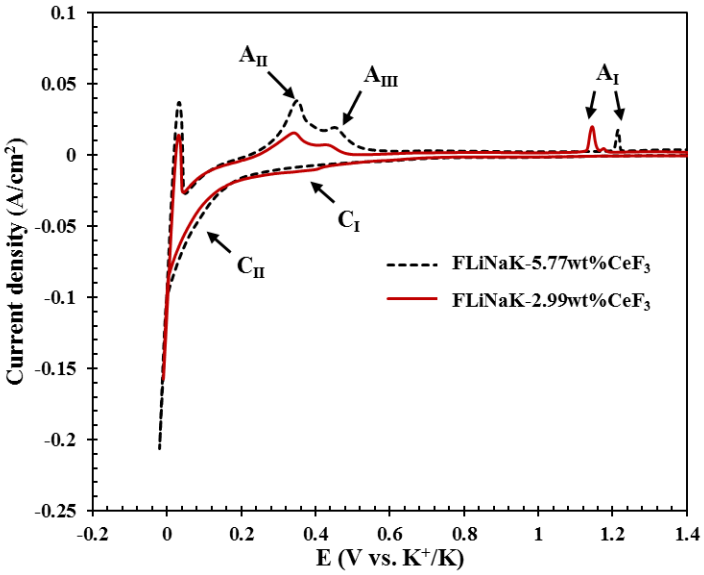

Figure 2-24. Cyclic voltammograms obtained in FLiNaK-2.99 wt% CeF_3 and FLiNaK-5.77 wt% CeF_3 molten salts on Ni working electrode. Counter electrode: graphite; T=973K; Scan rate: 200 mV/s.

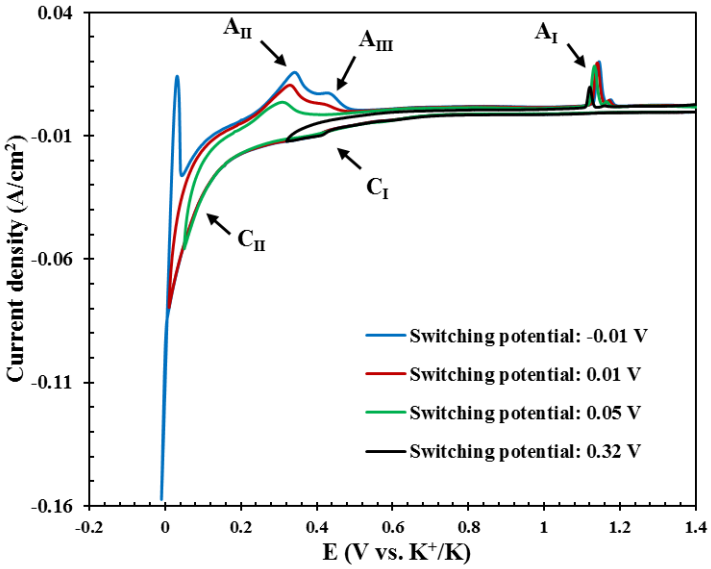

Figure 2-25. Cyclic voltammograms performed in FLiNaK-2.99 wt% CeF_3 molten salt at various switching potentials on Ni working electrode. Counter electrode: graphite; Scan rate: 200 mV/s.

To know whether the diffusion of Ce in Ni metal is limiting or not when the intermetallic compound is formed, the cyclic voltammetry tests at different concentrations were also carried out in this study. Figure 2-24 shows the cyclic voltammograms obtained in FLiNaK-2.99 wt% CeF_3 and FLiNaK-5.77 wt% CeF_3 molten salts, respectively. It can be seen that there is nothing changed on the configurations of the obtained cyclic voltammograms except the increases on the redox peaks of C_{II}, A_{II}, and A_{III} at higher concentration. This means that no new intermetallic compound will be formed when

different concentrations of CeF_3 exist in FLiNaK molten salt. Same as the results obtained on W electrode, there is only a slight difference on the peak current densities of C_I/A_I when different amounts of CeF_3 are added into FLiNaK molten salt. However, the location of oxidation peak A_I shifts a little which may be due to the surface change on the Ni electrode when intermetallic compound is formed as discussed above.

The co-reduction of Ni (II) and Ce (III) is also conducted on an inert W electrode to further confirm that Ni metal could assist the reduction of CeF_3 to occur at a potential higher than KF reduction. Figure 2-26 shows the representative cyclic voltammogram of FLiNaK-5.96 wt% CeF_3-0.28 wt% NiF_2 molten salt system at 973 K on the W working electrode. The redox peaks at the right side of the electrochemical window correspond to the redox reaction of Ni (II)/ Ni. For the left side of the electrochemical window, the redox peaks C_{II}, A_{II}, and A_{III} associated with the Ni-Ce intermetallic compound formation and dissolution are observed which is the same as the results obtained on Ni electrode without the addition of NiF_2. This result further affirms that Ni electrode could realize the extraction of Ce from FLiNaK molten salt. The redox peaks C_I/A_I which correspond to the redox reaction of Ce component ions was also detected here.

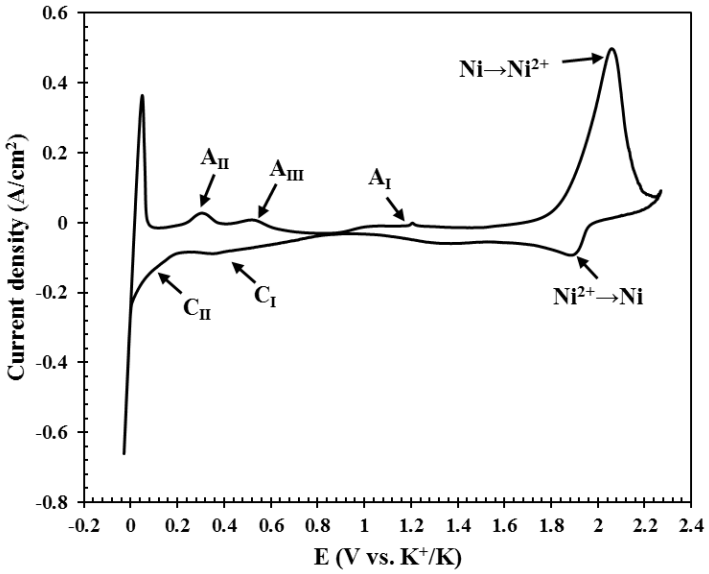

Figure 2-26. Cyclic voltammograms performed in FLiNaK-5.96 wt% CeF_3-0.28 wt% NiF_2 molten salt on W working electrode. Counter electrode: graphite; Scan rate: 200 mV/s.

The electrochemical behavior of FLiNaK-CeF_3 molten salt system was also studied by chronopotentiometry technique on Ni working electrode at the temperature of 973 K. The chronopotentiogram was obtained by applying a reduction current for 4 s and then the evolution of open circuit potential was recorded for another 46 s as shown in Figure 2-27. A plateau P1 can be observed when a reduction current of 10 mA is applied which is associated with the reduction of Ce component ions to Ce metal. The plateau P2 is attributed to the reduction of K (I) to K metal. A slight rise of this plateau over time was indicated, which may attribute to the nucleation of K on the electrode. No obvious transition plateau for Ce-Ni intermetallic compound formation was observed during the reduction process even when a higher reduction current, for example, 40 mA or 80 mA, is

applied. It is probably because the potentials for intermetallic compound formation and K (I) reduction are too close to each other. The evolution of open circuit potential was monitored after 4 s, and several plateaus were identified: A corresponds to the oxidation of the deposited K on the electrode surface, B and C corresponds to the dissolution of Ce-Ni intermetallic compounds, D corresponds to the anodic peak as observed in the cyclic voltammogram, previously discussed in the W and Cu electrodes sections.

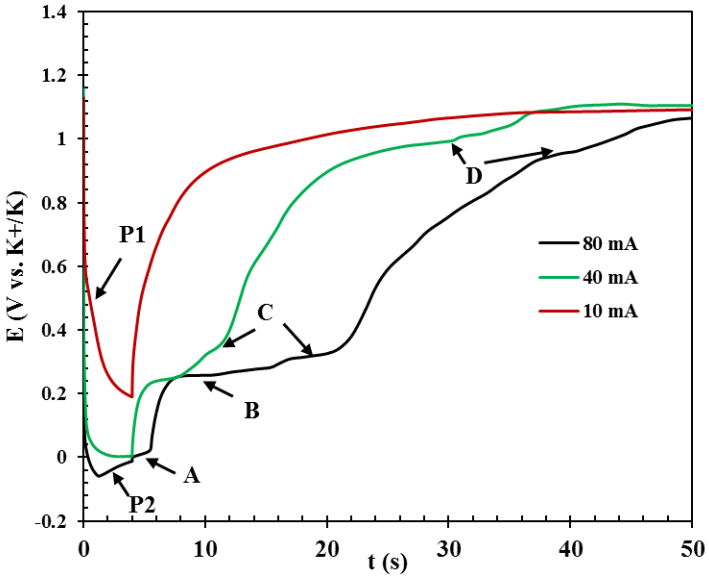

Figure 2-27. Potential evolution of the Ni working electrode against K^+/K over time by chronopotentiometry test at the temperature of 973 K through applying different reduction currents. Counter electrode: graphite; CeF_3=5.06 wt%; working electrode area=1.035cm^2.

To identify the formed Ce-Ni intermetallic compound when Ni working electrode is used in electrochemical tests, potentiostatic electrolysis was performed by applying a voltage of 0.02 V (vs. K^+/K) for 1 hour in FLiNaK-5.77 wt% CeF_3 molten salt system. SEM and EDS analyses were conducted to characterize the cross section of the nickel working electrode after electrolysis. In Figure 2-28a, an evident white strip can be seen on the top of nickel electrode, EDS mapping results (Figure 2-28c-d) obtained on this strip reveal the well overlapping of cerium and nickel. It implies the formation of intermetallic compound. Further EDS analyses of point 1 and point 2 (Figure 2-28b) on that strip give an atom ratio of ~1:5 between Ce and Ni for the formed Ce-Ni intermetallic compound. Thus, the formed Ce-Ni intermetallic compound should be $CeNi_5$. It is consistent with the theoretical calculation shown in Table 2-1 where $CeNi_5$ is the intermetallic compound which can bring the largest potential shift. The SEM analysis results also indicate that only the formation of $CeNi_5$ could achieve the extraction of Ce from FLiNaK molten salt. In addition to $CeNi_5$, some Ce metal was also observed in some parts of the cross section of the Ni electrode as shown in Figure 2-29. This phenomenon is the same as the one found in W and Cu electrodes. Potentiostatic electrolysis was also performed in FLiNaK molten salt with CeF_3 at a lower concentration (2.99 wt%) by applying a voltage of 0.02 V (vs. K^+/K) for 1 hour. Further SEM and EDS analyses were carried out on the cross section of the Ni electrode after electrolysis and the same results (Figure 2-30) were obtained as the ones acquired at the higher concentration (5.77 wt% CeF_3).

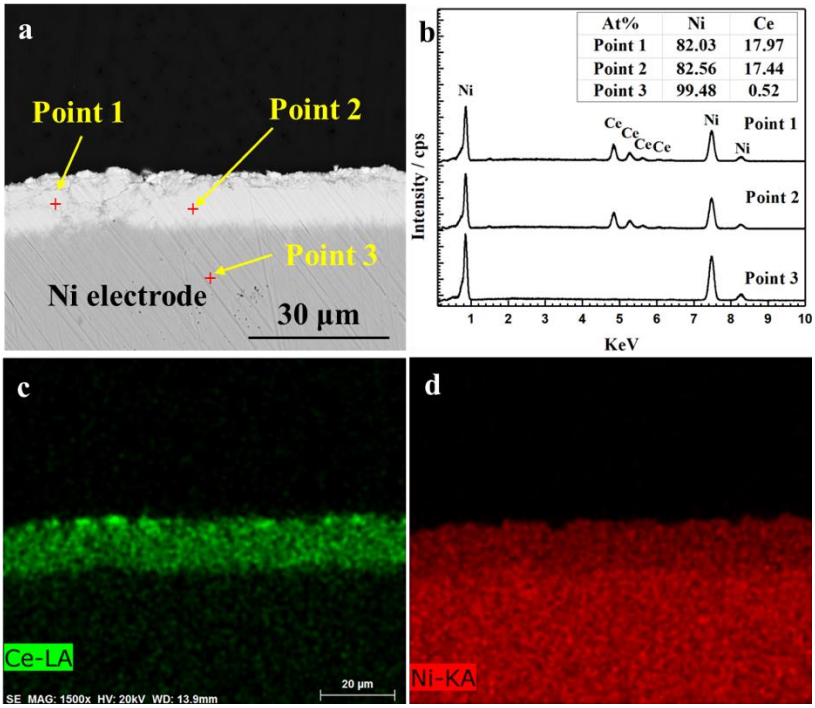

Figure 2-28. (a) Backscattered electrons (BSE) image of the deposited Ce-Ni intermetallic compound at nickel rod electrode; (b) EDS point scan results of point 1, point 2 and point 3 in Figure 2-28a; (c)-(d) EDS mapping results of Figure 2-28a.

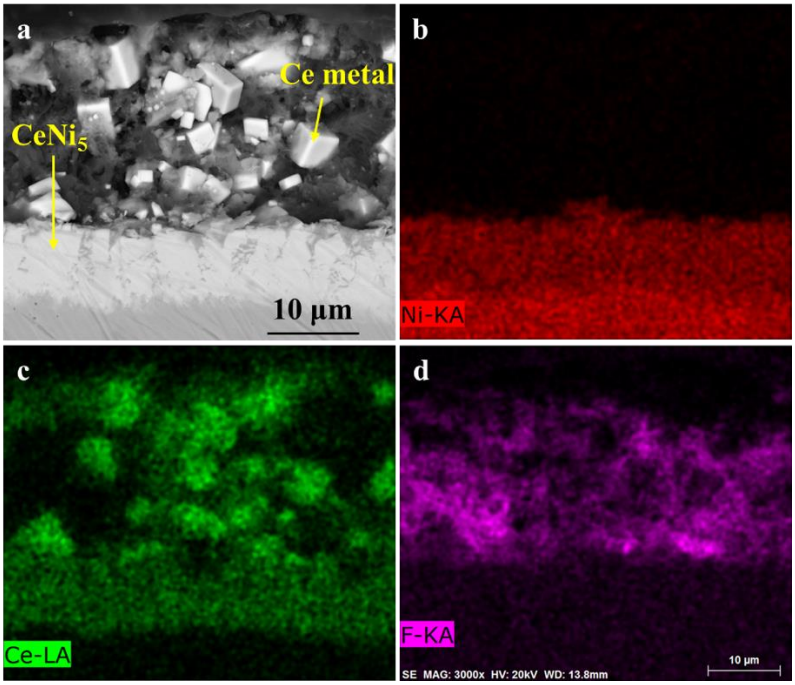

Figure 2-29. (a) Backscattered electrons (BSE) image of the cross section of polished nickel rod electrode with deposited Ce metal and Ce-Ni intermetallic compound after electrolysis; (b)-(d) EDS mapping results of Figure 2-29a.

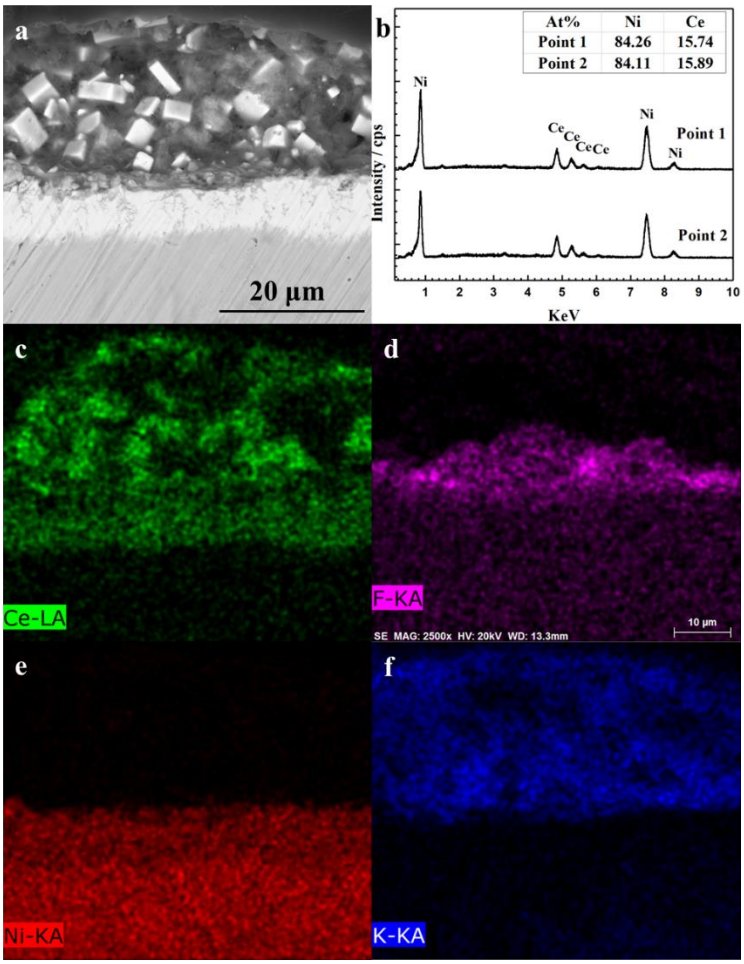

Figure 2-30. SEM analysis on the Ni electrode after potentiostatic electrolysis in FLiNaK-2.99 wt% CeF_3 molten salt system.

XRD analyses were also executed to confirm the results obtained on Ni electrode. Before XRD tests, potentiostatic electrolysis was performed on a Ni foil (area=~1 cm^2) by applying the voltage of 0.02 V (vs. K^+/K) for 1 hour. The Ni foil was taken out from electrochemical cell immediately after the electrolysis and then sealed in a Kapton tape to avoid the exposure to air. Figure 2-31 shows the result of XRD analysis from which the intermetallic compound $CeNi_5$ is observed and it is the same as what obtained from SEM tests. No Ce metal was detected which is probably due to the quantity of the deposited Ce metal being too small.

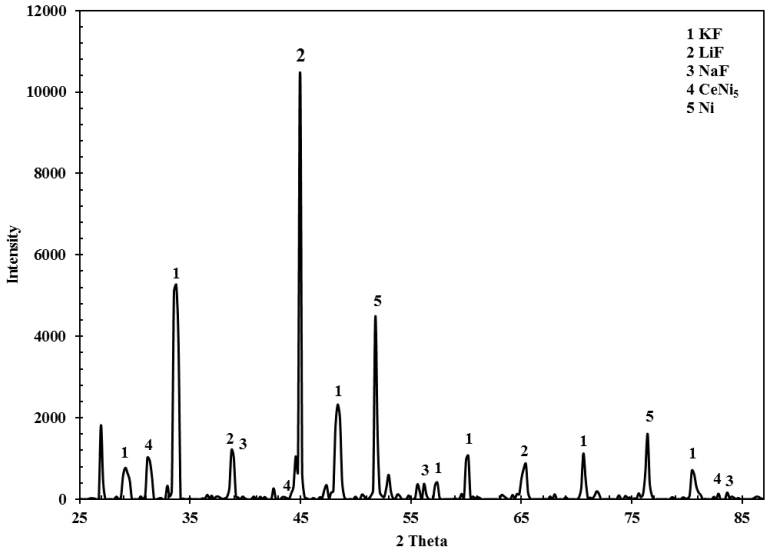

Figure 2-31. XRD analysis result of the chronopotentiometry electrolysis products of FLiNaK-CeF_3 melt on Ni electrode.

2.6. Conclusion

In this chapter, electrochemical tests including cyclic voltammetry and chronopotentiometry of LaF_3 in molten FLiNaK salt were conducted and compared with the results of pure FLiNaK in the study. Although the standard reduction potential of La (III)/La is more cathodic than that of the basic salt melt constituents: K (I)/K and Na (I)/Na, the redox reaction of lanthanum in the salt occurring prior to that of potassium was confirmed by these tests. To identify the redox reaction happens to lanthanum, chronopotentiometry electrolysis was performed to obtain the reduction product on both tungsten and molybdenum electrodes which was later utilized for SEM analyses. The results of SEM analyses verified that the reduction product is lanthanum metal. It is suspected that the formation of LaF_6^{3-} in molten fluoride salt because of the existence of KF or NaF results in this interesting phenomenon. Based on this finding, an innovative method can be proposed for the separation of La or other fission product in molten fluoride salts. In this new method, KF or NaF is added into the molten fluoride salts in which La predominantly exists in form of LaF_6^{3-} instead of La^{3+} species and then the equilibrium reduction potential of La shifts to a more positive value. Unlike the electrodeposition methods assisted by using liquid metal and reactive electrodes, which face the challenges of the isolation of the reactive electrode due to the formation of intermediate compound and the ability to maintain a low activity value of active metal in liquid electrode, the method developed in this study will help get pure La metal in a simpler way. It is anticipated that this technique can also be applied to extract other active metals such as critical materials (rare earth metals) from molten fluoride salts or other kinds of molten salt systems. In addition to inert electrode, Ni electrode was also used for the electrochemical separation of lanthanum in FLiNaK molten salt in which an intermetallic compound formation between Ni and La was identified.

The electrochemical behaviors of CeF_3 in FLiNaK melt at 973 K on different working electrodes (W, Cu, and Ni) are also explored in this chapter. It was found only Ni electrode was able to form intermetallic compound with Ce. The formed intermetallic compound was later identified to be $CeNi_5$ by SEM and XRD analyses. To confirm the feasibility of Ni electrode on the electrochemical separation of Ce from FLiNaK molten salt, the co-reduction of Ni (II) and Ce (III) was also investigated on an inert W electrode and the same result was obtained as the one acquired on Ni electrode. Therefore, among the three electrodes tested in the study, only Ni electrode can be applied to separate Ce from FLiNaK molten salt. A new redox reaction was also observed by both cyclic voltammetry and chronopotentiometry methods on all the three electrodes. The reduction product for this new redox reaction was found to be Ce metal. It is suspected that this new redox reaction is associated with the Ce component ions which are formed by Ce and impurity ions such as oxide or hydroxide ions. However, based on the extremely small current density obtained from cyclic voltammetry test which is probably due to small amount of the formed Ce component ions, the Ce cannot be extracted from FLiNaK molten salt on a large scale.

3. Fundamental property studies of lanthanum in FLiNaK molten salt

3.1. Introduction

Lanthanum is one of the abundant lanthanide fission products in nuclear reactors [110] and which is commonly taken as a model system for the electrochemical separations of fission products in molten salt. To manage the electrochemical separation of lanthanum, the understanding of its fundamental properties is significant. Massive studies have been performed for the fundamental properties of lanthanum in LiCl-KCl molten salt [111,112,113]. However, the investigation of lanthanum in molten fluoride salt is still very rare. Chesser et al. [94] recently studied the diffusion coefficient of lanthanum in FLiNaK molten salt using cyclic voltammetry technique, and reported that the diffusion coefficient is much less than that in chloride salt.

Based on study in Chapter 2, lanthanum species exist in the form of LaF_6^{3-} instead of La^{3+} in FLiNaK molten salt, it is interesting to know the kinetics properties of LaF_6^{3-} in molten salt and their difference with that of La^{3+}. In the present work, the diffusion coefficients of LaF_6^{3-} in FLiNaK molten salt were studied at different concentrations and temperatures by the method of chronopotentiometry. Additionally, potentiodynamic polarization measurements at different LaF_6^{3-} concentrations and temperatures were carried out. Through using a non-simplified electrode kinetics equation as reported by Guo et al [114] to nonlinearly fit the obtained potentiodynamic polarization curves, the kinetics parameters such as exchange current density, reaction rate constant, and charger transfer coefficient were determined.

3.2. Experimental

All the electrochemical experiments and salt preparations were performed in an argon-filled glove box manufactured by Inert Technology. The oxygen and moisture inside the glovebox were maintained below 5 ppm and 0.5 ppm respectively during normal operation. The chemicals used in this study include lithium fluoride (LiF, >99.0% purity, Sigma Aldrich), sodium fluoride (NaF, >99.0% purity, Sigma Aldrich), and potassium fluoride (KF, >99.5% purity, Sigma Aldrich). To provide lanthanum ions, lanthanum fluoride (LaF_3) with the purity of ≥99.99% was procured from Sigma Aldrich. 50 g FLiNaK constituents were prepared by weighing LiF, NaF, and KF chemicals according to the FLiNaK composition of 46.5 mol% LiF, 11.5 mol% NaF, and 42 mol% KF using a precision analytical balance with an accuracy of 0.0001 g (MS 105DU Mettler Toledo). The prepared FLiNaK constituents and LaF_3 chemicals were mixed very well inside a plastic sample bottle and then transferred to a nickel crucible (55 ml, Sigma Aldrich). The nickel crucible with an external alumina safety crucible was then placed in a muffle furnace (Thermofisher Scientific FB1315M) for which the temperature can be maintained within ±1℃ during the experiment. The muffle furnace was customized with a lid which was equipped with a quartz assembly to fix the electrodes. The salt mixture was dehydrated at

473 K for 24 hours to eliminate the oxygen and moisture and subsequently heated up to the target temperature for further electrochemical tests.

The electrochemical tests in this study utilized a three-electrode electrochemical cell in the furnace. The working electrodes used was a 1.6 mm diameter tungsten rod (Midwest Tungsten Service, >99.5% purity). The counter electrode was a 3.05 mm diameter graphite rod (99.9995% purity, Alfa Aesar). The reference electrode utilized was a 0.81 mm diameter platinum wire (99.99%, Surepure Chemetals). The bottoms of the electrodes were immersed in the FLiNaK-LaF_3 salt bath while their top ends were connected to the Gamry Interface 1000 poteniostat to perform the electrochemical measurements. The surface area of the working electrode was measured according to the submerged depth into the salt melt. Open circuit potential test was conducted before the chronopotentiometry and potentiodynamic polarization tests to check the stability of the system. The current interrupt method which is programmed in the Gamry Framework software was chosen to perform IR compensation in all the measurements.

3.3. Results and discussions

The electrochemical behavior of LaF_3 in FLiNaK molten salt has been studied in Chapter 2 by cyclic voltammetry test as shown in Figure 3-1. Generally, it is believed that the electrodeposition of lanthanum is impossible in FLiNaK molten salt because of the more cathodic standard reduction potential of La^{3+}/La than that of K^+/K. However, lanthanum predominantly exists in the species of LaF_6^{3-} instead of La^{3+} in FLiNaK molten salt as discussed in Chapter 2 and the existence of LaF_6^{3-} helps shift the electrodeposition potential to a more anodic value. As a result, the electrochemical reduction of LaF_3 in FLiNaK molten salt is a one-step charge transfer process, i.e., $LaF_6^{3-}+3e^- \rightarrow La+6F^-$, as reported in Chapter 2.

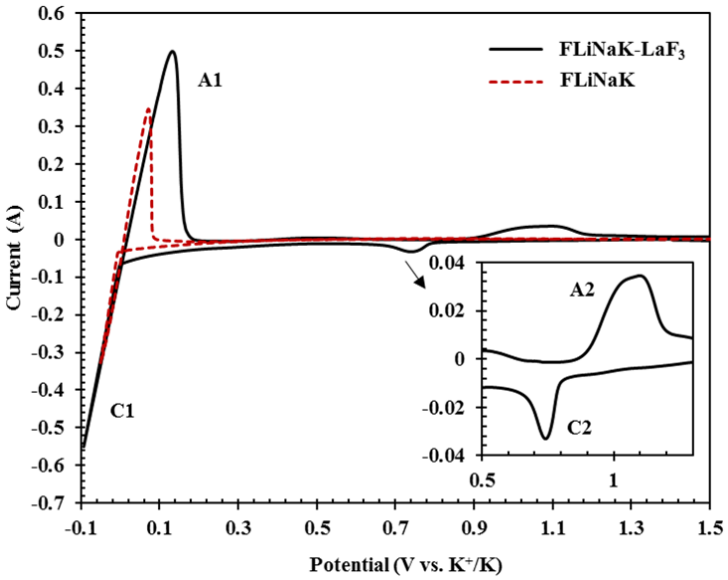

Figure 3-1. Typical cyclic voltammograms obtained in FLiNaK-LaF_3 (working electrode area=0.673 cm^2) and pure FLiNaK molten salts at the scan rate of 100 mV/s reported in Chapter 2.

Based on the known redox reaction of LaF_3 occurring in FLiNaK molten salt, the reduction process of LaF_3 in FLiNaK melt was studied by chronopotentiometry (CP) test in the present study and then the diffusion coefficients were determined at several temperatures. Figure 3-2 illustrates the typical chronopotentiograms of LaF_3 (1.05×10^{-4} mol/cm^3) in FLiNaK molten salt at the temperatures of 923, 973, and 1023 K when applying different currents. The first plateau shown with time evolution corresponds to the reduction of LaF_6^{3-} into La metal. After this plateau, the cathodic potential rapidly decreased to reach a limiting value which corresponds to the reduction of potassium. The transition time for the reduction of LaF_6^{3-} can be determined from chronopotentiograms using the method described in the literature [115]. Figure 3-3 (A) shows the relationship between the applied current and the obtained transition time for the chronopotentiometry data given in Figure 3-2. A fine proportional relation can be observed between I and $\tau^{-1/2}$. It indicates that the Sand's equation is applicable for the reduction of LaF_3 in FLiNaK molten salt. The diffusion coefficient of LaF_6^{3-} can be calculated from the slope of the plot of I versus $\tau^{-1/2}$ based on Sand's equation [116] shown below

$$I\tau^{1/2} = 0.5nFC_o^*S\pi^{1/2}D^{1/2} \quad (3\text{-}1)$$

where I is the applied current (A), τ is the transition time (s), C_o^* is the bulk concentration (mol/cm^3), D is the diffurion coefficient (cm^2/s), F is the Faraday's constant, S is the working electrode surface area (cm^2) and n is the electron transfer number.

In addition to the chronopotentiometry test of LaF_3 in FLiNaK molten salt at the concentration of 1.05×10^{-4} mol/cm^3, a similar test was performed at a higher concentration (2.25×10^{-4} mol/cm^3). The relationship between the applied current I and the obtained transition time τ was plotted which can be seen in Figure 3-3 (B). The diffusion coefficients at these two different concentrations were calculated based on equation (3-1) and summarized in Table 3-1. These values are smaller than the reported 9.16×10^{-7} cm^2/s at 923K, 2.15×10^{-6} cm^2/s at 973 K, and 4.62×10^{-6} cm^2/s at 1023 K by Chesser et al [94]. However, if that considering all of these values are extremely small, this discrepancy may be acceptable. When comparing with the diffusion coefficient of lanthanum ions in chloride salt [117], it is found the one obtained in FLiNaK molten salt is much smaller. The reason for this phenomenon could be that the lanthanum species exist in the form of LaF_6^{3-} in FLiNaK molten salt not La^{3+} which is the presented form in chloride salt. The mobility of LaF_6^{3-} in FLiNaK molten salt is reduced since it is "heavier" than La^{3+}.

Assuming that the diffusion coefficient is independent of concentration which has been verified by simulations on other molten salt system [118], the average value at 923, 973, and 1023 K was calculated respectively from the data obtained at these two different concentrations. The average diffusion coefficient can be further used to produce the Arrhenius plot as shown in Figure 3-4. Based on the fitted linear relationship in the Arrhenius plot, the diffusion coefficient of LaF_6^{3-} in FLiNaK molten salt was formulated as

$$lnD = -1.5945 - 12487/T \quad (3\text{-}2)$$

According to the Arrhenius equation as follows

$$D = D_0 \exp\left(-\frac{E_a}{RT}\right) \tag{3-3}$$

where E_a is activation energy (J/mol), R is the gas constant and T is temperature (K), the activation energy E_a was acquired with the value of 103.8 KJ/mol which is close to the value of 127 KJ/mol reported in the previous study [94].

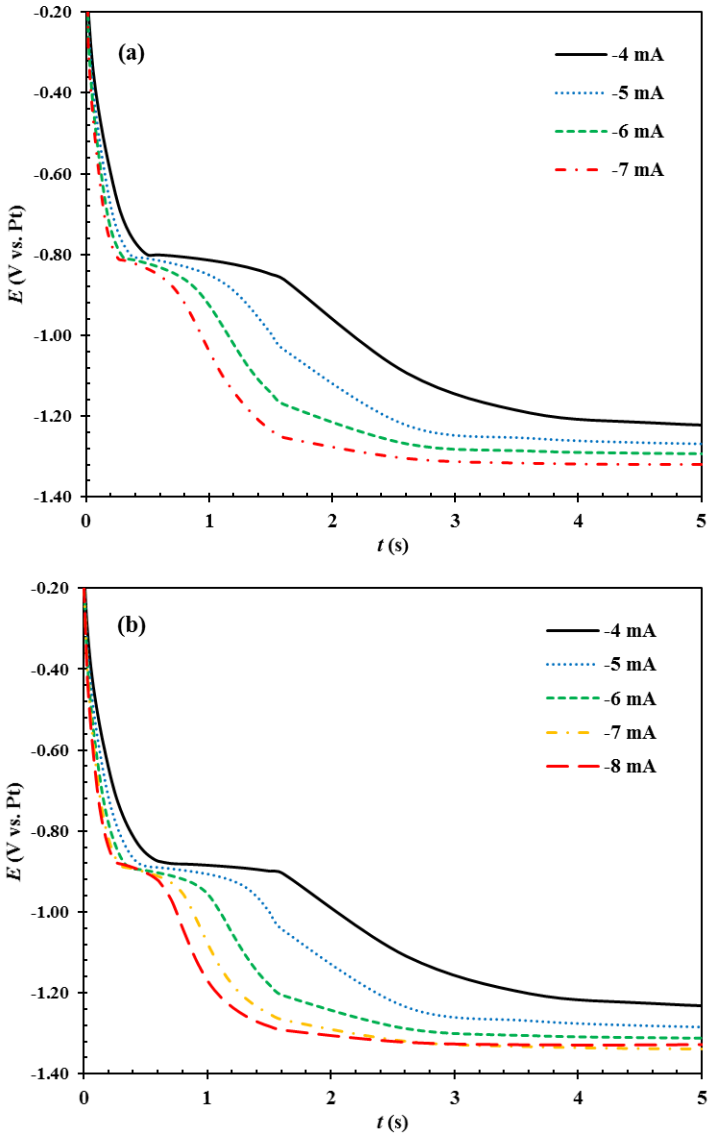

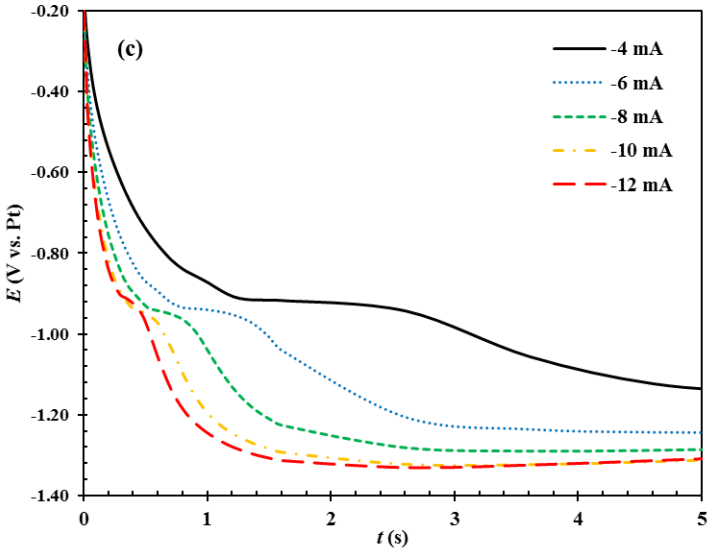

Figure 3-2. Chronopotentiograms of LaF_3 in FLiNaK molten salt at the temperatures of (a) 923 K, (b) 973 K, and (c) 1023 K. LaF_3=1.05×10^{-4} mol/cm^3; electrode area=0.296 cm^2.

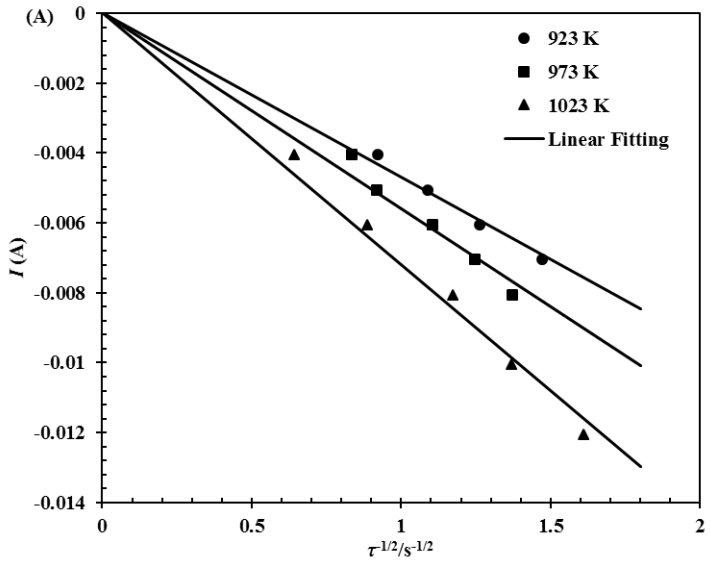

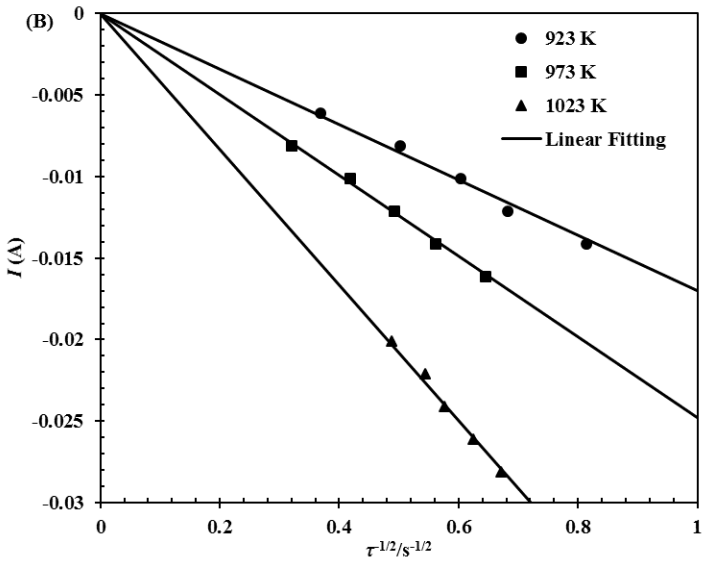

Figure 3-3. Linear relationship of I versus $\tau^{-1/2}$ for the CP test of LaF_3 in FLiNaK molten salt with the concentration of (A) $LaF_3=1.05\times10^{-4}$ mol/cm^3 and (B) $LaF_3=2.25\times10^{-4}$ mol/cm^3.

Table 3-1. Diffusion coefficients of LaF_6^{3-} in FLiNaK molten salt determined using equation (3-1).

C_o^* (mol/cm^3)	1.05×10^{-4}			2.25×10^{-4}		
T (K)	923	973	1023	923	973	1023
$D\times10^7$ (cm^2/s)	3.47	4.92	8.14	2.24	4.76	13.4

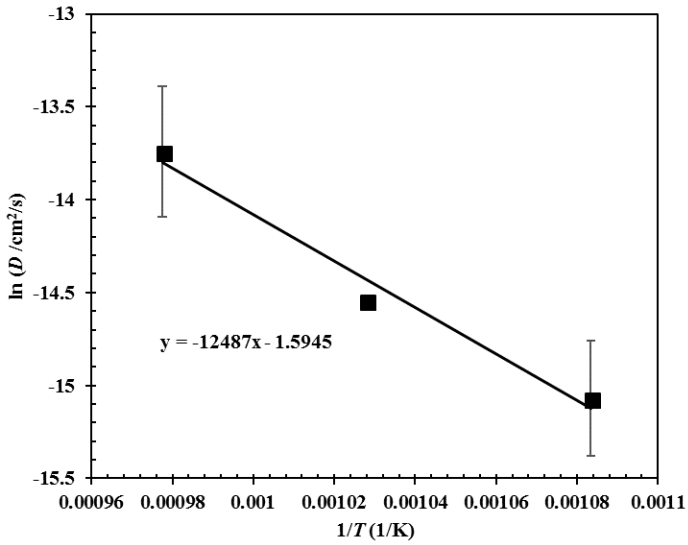

Figure 3-4. Arrhenius plot of diffusion coefficient as a function of temperature.

Kinetic parameters such as exchange current density and charge transfer coefficient are important to understand the reaction kinetics of LaF_6^{3-} to La metal in FLiNaK molten salt. Potentiodynamic polarization can be used to determine the values of these kinetic

parameters. In potentiodynamic polarization, the electrode at zero-current potential is in fact under cathodic polarization since the measured current is the sum of charging current and faradaic current [119]. Charging current comes from the continuous change of the potential during the scan process and is proportional to scan rate. Based on that the magnitude of charging current decreases with the decreasing scan rate, low scan rate is usually employed in potentiodynamic polarization to minimize the influence of charging current. The zero-current potentials at the scan rates of 0.5 and 1 mV/s are commonly believed to nearly equal the equilibrium potential. However, the potentiodynamic polarizations at 0.5 and 1 mV/s will take longer time, and the electrode surface may change greatly during this process and bring more noise to the curve obtained. In the present study, the potentiodynamic polarizations were first carried out at four different scan rates: 0.5, 1, 2, and 5 mV/s. Figure 3-5 indicates the potentiodynamic polarization curves at these four different scan rates which overlap significantly during each scan except the distortion part can be observed. Therefore, the scan rate of 5 mV/s is sufficiently low to approach the steady state in the investigated system and will be adopted for all the following tests.

In Figure 3-5, the potential applied on the inert working electrode (W) was scanned from the negative overpotential to the anodic direction in the potentiodynamic polarization test. In the negative overpotential section, LaF_6^{3-} was reduced to La metal and formed a layer on the tungsten working electrode surface. A distortion on the curve where the initial potential scan started was observed in this section which could be attributed to the initial development of the diffusion layer. In the positive overpotential section, the dissolution of the deposited La occurs and the current increased with the increase of overpotential. An irregular variation was observed after overpotential η reached the value of around 0.1 V. This is due to the heterogeneous dissolution of the deposited La layer which might not be uniform after the negative overpotential scan [120]. The dissolution of La layer and the decrease of La coverage area on the electrode with time might be different at different scan rates, as a result, there is an obvious deviation on the distortion area in the positive overpotential scan section for each scan.

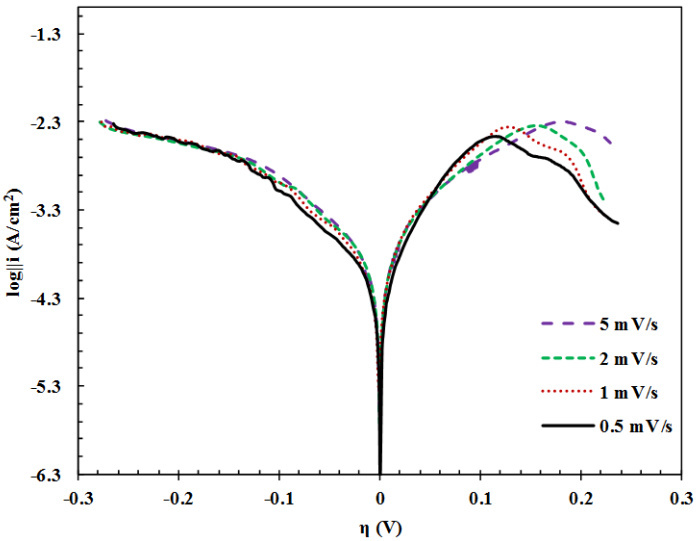

Figure 3-5. Potentiodynamic polarization curves measured at different scan rates for LaF_3 in FLiNaK molten salt. LaF_3=1.58×10^{-4} mol/cm^3; T=923K.

Figure 3-6 illustrates the potentiodynamic polarization curves obtained at the scan rate of 5 mV/s for FLiNaK molten salt containing different concentrations of LaF_3 at the temperatures of 923, 973, and 1023 K, respectively, from which it can be seen the measured current density increases with concentration for each temperature. The surface area of the working electrode was used to convert the current to current density based on the assumption that the current is uniformed distributed on electrode surface.

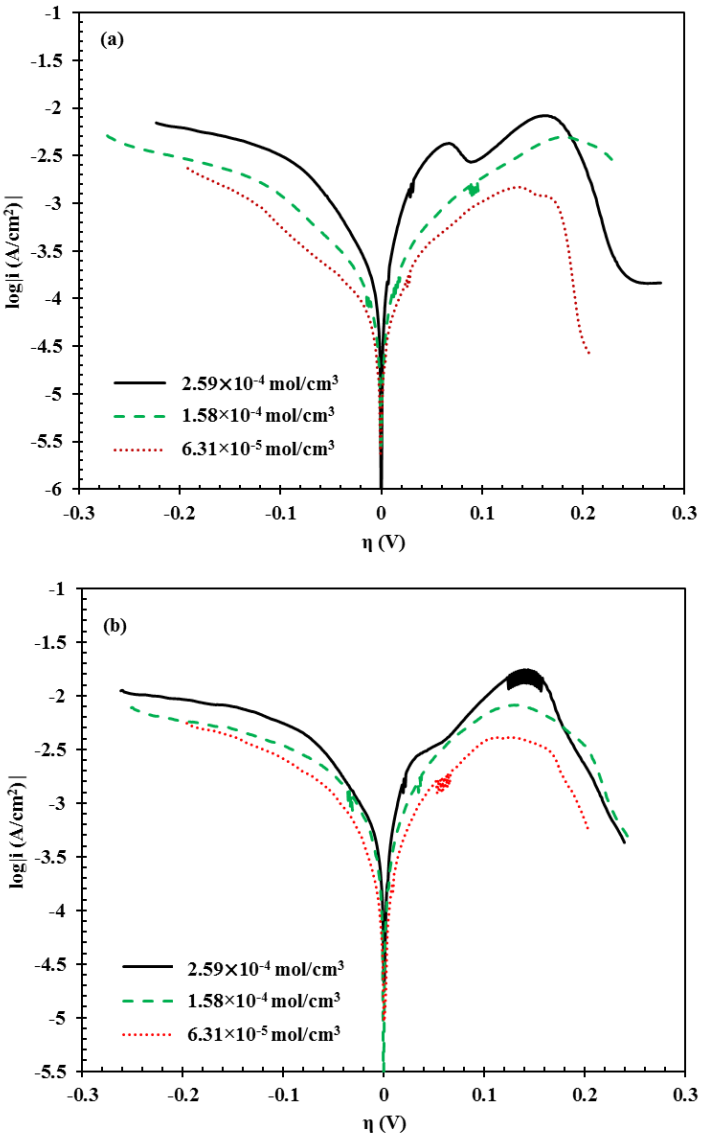

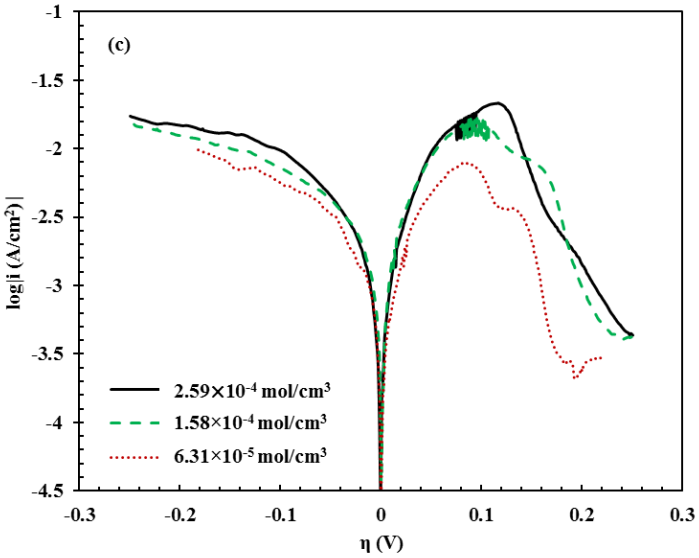

Figure 3-6. Potentiodynamic polarization curves at different concentrations for the temperatures of (a) 923 K, (b) 973 K, and (c) 1023 K. Scan rate: 5 mV/s.

In order to determine the kinetic parameters, an analysis method based on the non-simplified electrode kinetic equation was applied here. This method is thought to be more reliable than the conventional Tafel and linear polarization methods [120]. The non-simplified electrode kinetic equation for the redox reaction of La can be expressed as follows [120]

$$i = \frac{i_0 \left\{ exp\left[\frac{(1-\alpha)nF)}{RT}\eta\right] - exp\left(\frac{-\alpha nF}{RT}\eta\right)\right\}}{1 - \frac{i_0}{i_L} exp\left(\frac{-\alpha nF}{RT}\eta\right)} \quad (3\text{-}4)$$

Where i is the current density (A/cm^2), i_0 is the exchange current density (A/cm^2), n is the electron transfer number, α is the charge transfer coefficient, η is the overpotential (V). i_L (A/cm^2) is the limiting diffusion current density which is defined as below

$$i_L = -nFDC_o^*/\delta \quad (3\text{-}5)$$

where δ is the diffusion layer thickness (cm).

Equation (3-4) was applied to fit the experimental potentiodynamic polarization curves. The values of the various parameters that best fit the experimental data can be extracted by the least squares fitting procedure through minimizing χ^2 with respect to the 3 fitting parameters: i_0, i_L, and α. Thus, if we refer to the parameters by a vector m= [i_0, i_L, α], then the Chi-squared function to be minimized can be expressed by

$$\chi^2(m) = \left| i^{sim}(m) - i^{exp}(m) \right|^2 \quad (3\text{-}6)$$

The non-linear least squared algorithm can search this 3-dimensional parameter space to find the optimum values that minimize χ^2. Due to the distortion at both ends of the experimental polarization curve, the data in the overpotential range of -0.2 to 0.05 V were used to do the fitting. Through this way, these three parameters at which the calculated potentiodynamic polarization best fits the experimental one can be obtained. The solid lines in Figure 3-7 are the calculated polarization curves at the optimized values. It can be seen that the experimental data at the range (-0.2~ 0.1 V) are fitted well by the method. The optimized values for the parameters are included in Table 3-2 In addition to the parameters discussed previously, reaction rate constant k^0 is another key kinetics parameter for understanding the kinetics of the redox reaction. It is related to the exchange current density i_0 and charge transfer coefficient α by the following correlation [116, 120]:

$$i_0 = nFk^0 {C_o}^{*(1-\alpha)} \tag{3-7}$$

The values of i_0 listed in Table 3-2 were plotted against its corresponding concentration of LaF_3 in mol/cm^3 which can be seen in Figure 3-8. Equation (3-7) was used to fit the data points in Figure 3-8 from which it can be shown all data points agree well with the fitted power law trend line. The values of α from the fitted expression using equation (3-7) are 0.47 at 923 K, 0.51 at 973 K, and 0.47 at 1023 K, respectively. These numbers in fact are close to the values of α obtained from the optimization fitting of individual test results (Table 3-2). Table 3-3 lists the values of k^0 determined from the fitted expression by equation (3-7), from which it can be known k^0 increases with temperature.

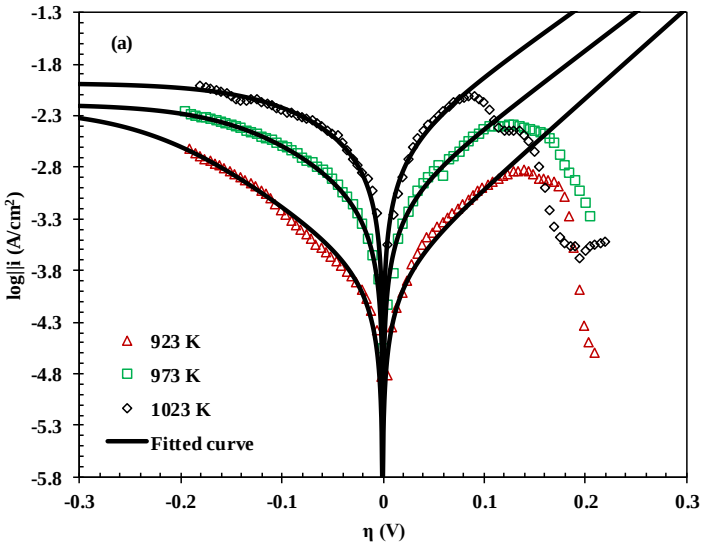

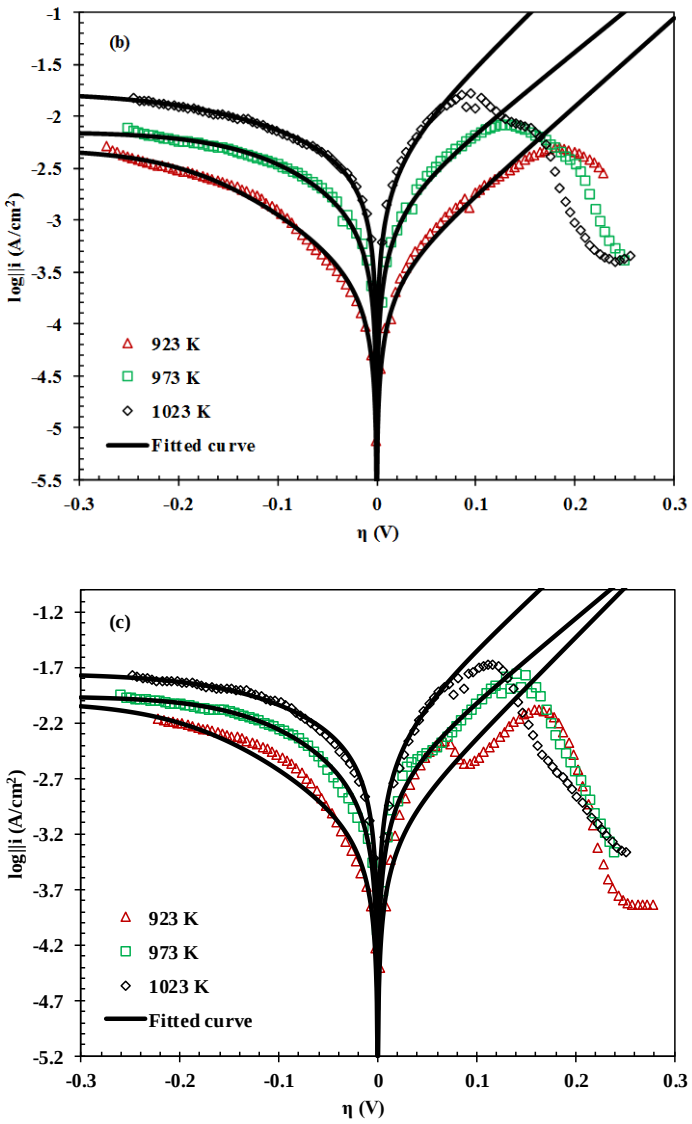

Figure 3-7. Potentiodynamic polarization curves at the scan rate of 5 mV/s for LaF_3 in FLiNaK molten salt at the temperatures of 923, 973, and 1023 K. (a) LaF_3=6.31×10^{-5} mol/cm^3; (b) LaF_3=1.58×10^{-4} mol/cm^3; (c) LaF_3=2.59×10^{-4} mol/cm^3.

Table 3-2. Optimized parameters determined by non-simplified electrode kinetic equation.

Concentration(mol/cm^3)	T (K)	i_0 (A/cm^2)	α	i_L (A/cm^2)
6.31×10^{-5}	923	0.00013	0.47	-0.0058
	973	0.00069	0.52	-0.0065
	1023	0.00250	0.53	-0.0102
1.58×10^{-4}	923	0.00025	0.48	-0.0049
	973	0.00120	0.50	-0.0070
	1023	0.00380	0.37	-0.0169
2.59×10^{-4}	923	0.00060	0.45	-0.0010
	973	0.00180	0.52	-0.0109
	1023	0.00460	0.44	-0.0177

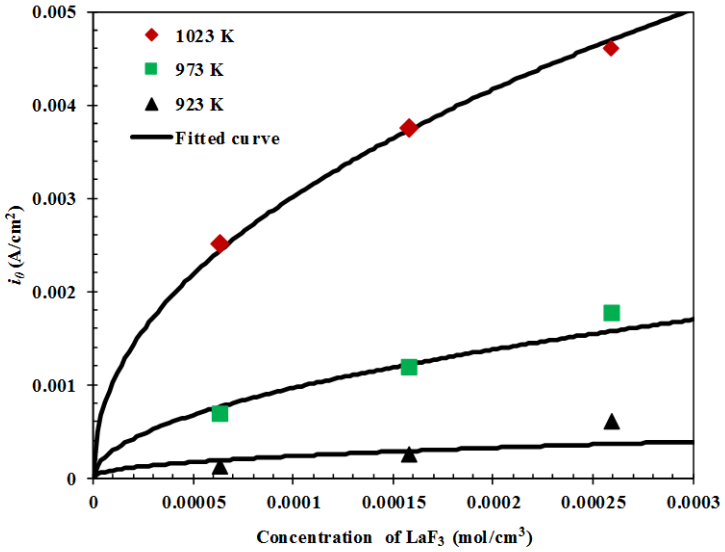

Figure 3-8. The plot of i_0 from Table 3-2 versus LaF_3 concentration.

Table 3-3. The obtained values of α and K^0 at different temperatures using equation (3-7).

T (K)	K^0 (cm/s)	α
1023	7.6×10^{-7}	0.47
973	3.8×10^{-7}	0.51
923	5.9×10^{-8}	0.47

3.4. Conclusion

The present study explored the fundamental properties of LaF_6^{3-} in FLiNaK molten salt at different concentrations and temperatures. The diffusion coefficient was obtained from chronopotentiometry test using Sand's equation and it is found the diffusion coefficient of LaF_6^{3-} in FLiNaK molten salt is much smaller than that of La^{3+} in chloride salt. The diffusion coefficients at the temperature range of 923 to 1023 K showed temperature dependence in compliance with Arrhenius law which were determined as $lnD = -1.5945 - 12487/T$. The activation energy for the diffusion of LaF_6^{3-} ions in FLiNaK molten salt was determined to be 103.8 KJ/mol. Other kinetics parameters including exchange current density, charge transfer coefficient, and reaction rate constant of LaF_6^{3-}/La reaction were also studied by performing potentiodynamic polarization tests at three different concentrations in the temperature range of 923 K to 1023 K. A non-simplified electrode kinetics equation was employed as the analysis method to nonlinearly fit the obtained potentiodynamic polarization curves. Unlike the conventional Tafel and LP methods in which the mass transfer influence is neglected, the obtained kinetics parameters by the non-simplified electrode kinetics equation which incorporates both the reaction kinetics and mass transfer will be more reliable.

4. Analytical methods for consecutive charge transfer electrochemical reaction with the presence of reductant and product: fundamental properties of CrF_2 in FLiNaK molten salt

4.1. Introduction

Chromium is considered the predominant corrosion product since it forms one of the most stable fluorides and is more readily oxidized than nickel or iron [121]. The understanding of the electrochemistry-related fundamental properties of chromium cations in FLiNaK molten salt will be beneficial for performing pyrochemical separation of chromium and in situ detecting or quantifying dissolved chromium cations during the corrosion process. For instance, the known diffusion coefficient can be used to online monitor the extent of chromium corrosion in heat transfer loops by electrochemical analysis. As a result, several relevant studies have been carried out for the investigation of chromium cations in FLiNaK molten salt. Yoko et al [122] studied the reduction mechanism of CrF_3 in FLiNaK molten salt and reported the diffusion coefficient of Cr (III) at different temperatures by the means of cyclic voltammetry and chronopotentiometry. Wang et al [123] derived the diffusion coefficient of Cr (III) in FLiNaK molten salt based on Warburg coefficient in electrochemical impedance spectroscopy (EIS). There is very limited study on the diffusion coefficient of Cr (II). To fill this research gap, Wu et al [124] investigated the diffusion coefficients of both Cr (III) and Cr (II) ions in FLiNaK melt by cyclic voltammetry. In that study, the diffusion coefficient of Cr (II) was calculated using Berzins equation [125] based on Cr (II)/Cr cathodic peak current density and the assumption of $C_{Cr(II)} = C_{Cr(III)}$ which actually makes no sense.

The present study was focused on the fundamental properties investigation of CrF_2 in FLiNaK molten salt. It is proposed in the previous studies [122,126,127,128] that the disproportionation of $3CrF_2 \leftrightarrow 2CrF_3 + Cr$ probably occurs in molten fluoride salts. This disproportionation reaction was proved by Peng et al [129] by electrochemical techniques and spectrometry methods. The XRD analysis (Figure 4-1) of the quenched FLiNaK-CrF_2 molten salt at room temperature in our study shows the existence of both the chromium trivalent ion and chromium metal. It further indicates that the disproportionation reaction of CrF_2 occurs in FLiNaK molten salt. In addition, assuming the molten salt structure is unchanged during the quench process, the XRD pattern shown in Figure 4-1 reflects that chromium trivalent ion exists in the form of CrF_6^{3-} not Cr^{3+} while chromium divalent ion exists in the species of CrF_3^- not Cr^{2+} in FLiNaK molten salt. This phenomenon was also verified by Peng et al [129] through the Raman spectroscopy test of the molten FLiNaK-CrF_2 salt. Therefore, CrF_3^- and CrF_6^{3-} will be adopted to represent chromium ions in all the following discussions.

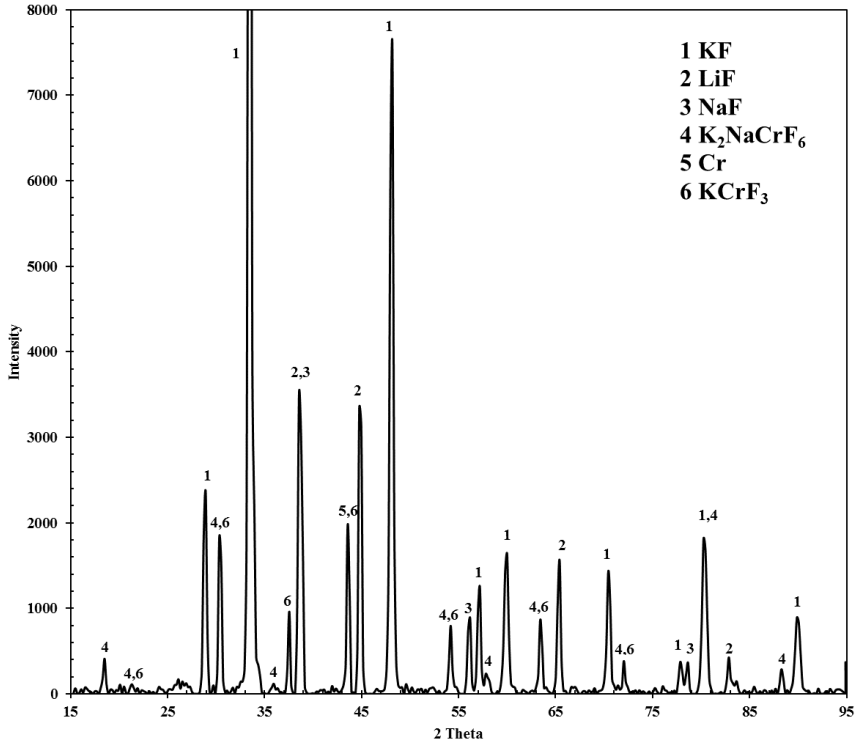

Figure 4-1. XRD analysis result of the quenched FLiNaK-CrF_2 molten salt.

Based on that a part of CrF_2 in FLiNaK molten salt will undergo the disproportionation reaction, both the CrF_3^- and CrF_6^{3-} species will exist in FLiNaK-CrF_2 molten salt system studied in the present work. Randles equation [130] is typically used to calculate the diffusion coefficient based on the peak current density in cyclic voltammogram for a reversible soluble-soluble system. However, it should be noted that this equation is only applicable when only one member (either reactant or product) of a redox couple is present in the electrolyte. It means Randles equation will not be applicable for FLiNaK-CrF_2 molten salt system in which both members of the redox couple CrF_3^-/CrF_6^3 exist. Sand's equation [131] can be used in the data analysis of chronopotentiogram for simple charge transfer reaction. However, for FLiNaK-CrF_2 system in which there is a consecutive charge transfer reaction with both CrF_3^- and CrF_6^{3-} species existing, Sand's equation will not be applicable. In the present study, new data analysis methods were proposed for cyclic voltammogram and chronopotentiogram of the consecutive charge transfer reaction with the presence of both reactant and intermediate product in electrolyte initially. The diffusion coefficients of CrF_3^- and CrF_6^{3-} obtained based on these new data analysis methods will be more reliable.

4.2. Experimental

All the sample preparations and electrochemical experiments were performed in a glovebox (Inert Technology) in which the moisture and oxygen levels were maintained under 0.5 ppm and 5 ppm, respectively. Chemicals including lithium fluoride (LiF, >99.0% purity, Sigma Aldrich), sodium fluoride (NaF, >99.0% purity, Sigma Aldrich), potassium fluoride (KF, >99.5% purity, Sigma Aldrich), and chromium difluoride (CrF_2, 99%,

Synquest Lab) were provided for this study. For each test, 50 g FLiNaK salt were prepared based on the composition of 46.5 mol% LiF, 11.5 mol% NaF, and 42 mol% KF using a precision analytical balance with the accuracy of 0.0001 g (MS 105DU Mettler Toledo). A small amount of CrF_2 was added into FLiNaK salt powder and mixed well inside a plastic sample bottle before transferring to a nickel crucible (55 ml, Sigma Aldrich). A three-electrode electrochemical test cell was assembled in a muffle furnace (Thermofisher Scientific FB1315M) for which the temperature can be maintained within $\pm$1℃. The nickel crucible with prepared salt powder was placed in the furnace and heated to the target temperature. Before heating up to the target temperature, the mixed salt powder was dehydrated at 473 K for 24 hours to remove the oxygen and moisture. The three electrodes used in this study consists of a 1.0 mm diameter tungsten working electrode (Midwest Tungsten Service, >99.5% purity), a 3.05 mm diameter graphite counter electrode (99.9995% purity, Alfa Aesar), and a 0.81 mm diameter platinum reference electrode (99.99%, Surepure Chemetals). The electrodes were polished with a sandpaper and washed ultrasonically in de-ionized water before using. During the experiment, the bottoms of these three electrodes were immersed in the FLiNaK-CrF_2 salt bath while the tops were connected to the Gamry Interface 1000 poteniostat through which the electrochemical signals were obtained. No touch of the electrodes with nickel crucible was confirmed before any experiment. The current interrupt method which is programmed in the Gamry Framework software was chosen to perform IR compensation in all the measurements.

4.3. Results and discussions

The electrochemical behavior of CrF_2 in FLiNaK molten salt was studied by the electrochemical technique of cyclic voltammetry. Figure 4-2 shows a typical cyclic voltammogram of CrF_2 in FLiNaK molten salt. The cathodic limit at the left side of the electrochemical window corresponds to the reduction of K (I) [99]. Two pairs of redox peaks C1/A1 and C2/A2 can also be observed in Figure 4-2. Based on the previous studies [124,129], these two pairs of redox peaks are attributed to the reactions (4-1) and (4-2).

$$CrF_6^{3-} + e^- \leftrightarrow CrF_3^- + 3F^- \quad (4\text{-}1)$$

$$CrF_3^- + 2e^- \leftrightarrow Cr + 3F^- \quad (4\text{-}2)$$

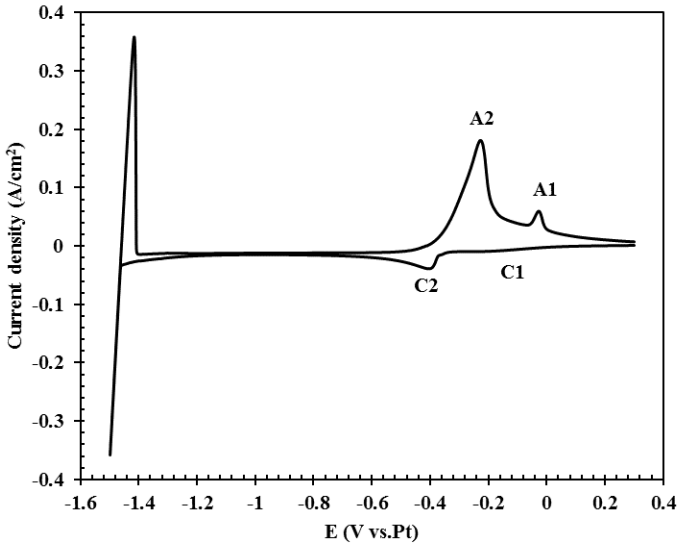

Figure 4-2. Cyclic voltammogram of CrF_2 in FLiNaK molten salt at the temperature of 873 K and scan rate of 100 mV/s. Working electrode: tungsten; reference electrode: platinum; counter electrode: graphite. $CrF_2=9.08\times10^{-5}$ mol/cm^3.

The potential evolution of the tungsten working electrode against platinum reference electrode over time is also monitored by applying a reduction current of 180 mA for 4 s and then an oxidation current of 180 mA for another 4 s as well. Figure 4-3 indicates the acquired chronopotentiometry data. CrF_6^{3-} is first reduced to CrF_3^- after a reduction current is applied, plateau A in Figure 4-3 corresponds to the reduction reaction of CrF_6^{3-} to CrF_3^-. The plateau A is not obvious here because a large current (180 mA) is imposed. After the concentration of CrF_6^{3-} drops to zero at the electrode surface, the flux of CrF_6^{3-} is insufficient to accept the electrons being forced across the electrode-solution interface, the potential shifts to a more negative value where the reduction reaction of CrF_3^- to Cr happens. It is reflected in plateau B. The potential transits to the value where the reduction reaction of K (I) to K happens after the depletion of CrF_3^- at the electrode surface which is indicated in plateau C. An oxidation current of 180 mA is applied after 4 s, as a result, the OCP steps up as shown in plateau C′ which corresponds to the oxidation of the deposited K. Similarly, the plateaus B′and A′ correspond to the oxidation of Cr and CrF_3^-, respectively. The plateau difference of C′ and C can be used to calculate the electrolyte resistance by comparing the potential difference between two applied currents. The ratio of $\Delta V/\Delta I$ indicates an electrolyte resistance of 0.15 Ω.

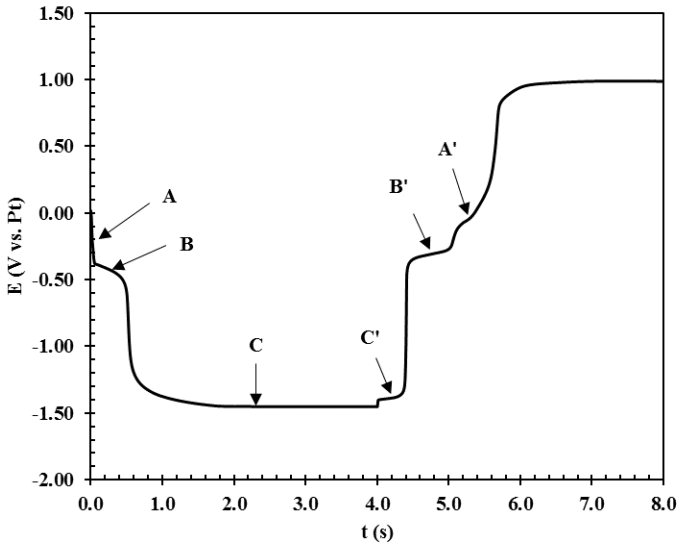

Figure 4-3. Potential evolution of the tungsten working electrode (s=0.6481 cm^2) against platinum reference electrode over time by chronopotentiometry test at the temperature of 1023 K. Counter electrode: graphite. CrF_2=2.37×10^{-4} mol/cm^3.

In order to study the fundamental properties of CrF_6^{3-} and CrF_3^- in FLiNaK molten salt, the cyclic voltammogram of the redox reaction of CrF_6^{3-}/ CrF_3^- is focused on and measured. Figure 4-4 shows the typical cyclic voltammogram of CrF_6^{3-}/ CrF_3^- in FLiNaK molten salt with the addition of 9.08×10^{-5} mol/cm^3 CrF_2 at different scan rates for the temperature of 873 K. At the various scan rates from 100 to 450 mV/s, the potentials for both the anodic and cathodic peak currents occurring are the same. It means the redox reaction of CrF_6^{3-}/ CrF_3^- is reversible based on that the peak potential is independent of scan rate when electron transfer rate is faster than its mass transport rate [132]. At the same time, the good linear correlation between peak current density and the square root of scan rate as shown in Figure 4-5 also indicates the reversibility of the redox couple of CrF_6^{3-}/ CrF_3^-. In addition, the reversibility of this redox reaction was confirmed in the previous studies by Wu et al [124] and Peng et al [129].

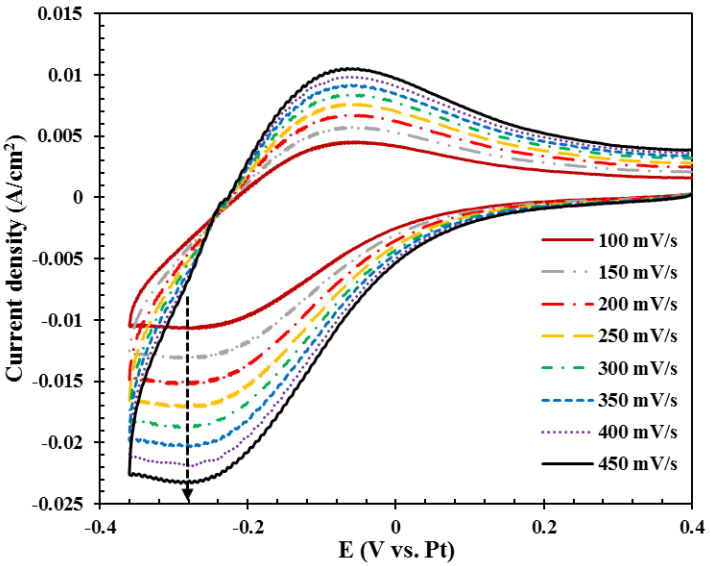

Figure 4-4. Cyclic voltammograms of redox reaction CrF_6^{3-}/ CrF_3^- couple in FLiNaK molten salt 873 K. Reference electrode: platinum, counter electrode: graphite. CrF_2=9.08×10^{-5} mol/cm^3.

The Randles equation (equation (4-3)) is typically used for electrode processes where the electrochemical equilibrium is reversible and achieved between two soluble species.

$$i_{\mathrm{p}} = 0.4463nFAC_{\mathrm{b}}D^{1/2}\left(\frac{nFv}{RT}\right)^{1/2} \tag{4-3}$$

where i_{p} is the peak current, A; D is the diffusion coefficient, cm^2/s; C_{b} is bulk concentration, mol/cm^3; n is the number of exchanged electrons of the reaction; and v is the scan rate, V/s; A is the electrode area, cm^2. However, it should be noted that the derivation of Randles equation is based on the assumption of no reductant presents. Based on the previous study by Peng et al [129] using electrochemical techniques and spectrometry method such as Raman spectroscopy and our X-ray powder diffraction (XRD) study of the quenched FLiNaK-CrF_2 molten salt, it is found CrF_6^{3-} is more stable than CrF_3^- in FLiNaK melt and CrF_3^- can be converted to CrF_6^{3-} and Cr metal via the disproportion discussed above. The conversion ratio of CrF_3^- to CrF_6^{3-} at 873 K was also confirmed with the values of 86.71% to 88.23% by Peng et al [129] and the data reported will be used here. Therefore, CrF_3^- and CrF_6^{3-} species coexist in the salt although only CrF_2 was added in molten FLiNaK in this study. The average conversion ratio of Cr divalent ions to Cr trivalent ions, 87.57%, reported in the previous study [129] was used to determine the concentrations of CrF_3^- and CrF_6^{3-} species in FLiNaK melt, respectively.

For the system where both oxidant and reductant exist, the theory developed by Keightley et al [133] can be adopted for the data analysis of the reversible cyclic voltammogram. For the reversible cyclic voltammetry in the presence of product, the current density in the forward sweep $\vec{\imath}$ and backward sweep $\overleftarrow{\imath}$ can be expressed by [133,134]

$$\vec{\imath} = nF\left(C_{\mathrm{b}}^{\mathrm{R}} {D_{\mathrm{R}}}^{1/2} + C_{\mathrm{b}}^{\mathrm{O}} {D_{\mathrm{O}}}^{1/2}\right)\left(\frac{nFv}{RT}\right)^{1/2} \chi(\xi;\xi_i) \tag{4-4}$$

$$\overleftarrow{\imath} = nF\left(C_{\mathrm{b}}^{\mathrm{R}} {D_{\mathrm{R}}}^{1/2} + C_{\mathrm{b}}^{\mathrm{O}} {D_{\mathrm{O}}}^{1/2}\right)\left(\frac{nFv}{RT}\right)^{1/2} [\chi(2\xi_r - \xi, \xi_i) - \chi(2\xi_r - \xi, \xi_r) - \chi(-\xi, \xi_r)] \tag{4-5}$$

where $\chi(x,\alpha) = \frac{\mathrm{d}^{1/2}}{\mathrm{d}x^{1/2}} \frac{1}{2\sqrt{\pi}} \left[\tanh\left(\frac{x+\alpha}{2}\right) - \tanh\left(\frac{\alpha}{2}\right)\right]$; $\xi = nF(E - E_{1/2})/RT$; $\xi_i = nF(E_i - E_{1/2})/RT$; $\xi_r = nF(E_r - E_{1/2})/RT$; $E_i = E_{1/2} + \frac{RT}{nF} \ln \frac{C_{\mathrm{b}}^{\mathrm{O}} {D_{\mathrm{O}}}^{1/2}}{C_{\mathrm{b}}^{\mathrm{R}} {D_{\mathrm{R}}}^{1/2}}$; E_r is the reversal potential; $E_{1/2}$ is half wave potential.

Either the forward or the backward branch of the cyclic voltammogram can be calculated by equations (4-4) and (4-5). It is found the value of $C_{\mathrm{b}}^{\mathrm{R}} {D_{\mathrm{R}}}^{1/2} / C_{\mathrm{b}}^{\mathrm{O}} {D_{\mathrm{O}}}^{1/2}$ is solely dependent on the current peak potential difference ΔE_p between the forward current peak and backward current peak [133]. It means the ratio of D_{R} to D_{O} can be predicted by the value of ΔE_p determined from the experimental cyclic voltammetry. Table 4-1 presents the current peak potential difference in cyclic voltammetry at different scan rates for two replicate tests at 873 K when 9.08×10^{-5} mol/cm^3 CrF_2 was added into FLiNaK molten salt. ΔE_p are averaged with the value of 0.239 V for test #1 and 0.230 V for test #2. The values of $\frac{nF}{RT}\Delta E_p$ are calculated and the corresponding values of $\frac{C_{\mathrm{b}}^{\mathrm{CrF_6^{3-}}} {D_{\mathrm{CrF_6^{3-}}}}^{1/2}}{C_{\mathrm{b}}^{\mathrm{CrF_3^-}} {D_{\mathrm{CrF_3^-}}}^{1/2}}$ obtained from equations (4-4) and (4-5) are listed in Table 4-2. The shapes and peaks of cyclic voltammograms calculated from equations (4-4) and (4-5) will vary with values of $\frac{C_{\mathrm{b}}^{\mathrm{CrF_6^{3-}}} {D_{\mathrm{CrF_6^{3-}}}}^{1/2}}{C_{\mathrm{b}}^{\mathrm{CrF_3^-}} {D_{\mathrm{CrF_3^-}}}^{1/2}}$ and the corresponded $\frac{|i_p|}{nFC_{\mathrm{b}}^{\mathrm{CrF_6^{3-}}} {D_{\mathrm{CrF_6^{3-}}}}^{1/2}} \left(\frac{RT}{nFv}\right)^{1/2}$ is also listed in Table 4-2.

Table 4-1.Current peak potential difference determined in cyclic voltammetry results shown in Figure 4-4.

Scan rate (mV/s)	ΔE_p (V)	
	Test #1	Test #2
100	0.229	0.246
150	0.236	0.229
200	0.240	0.235
250	0.235	0.227
300	0.239	0.234
350	0.240	0.230
400	0.241	0.223
450	0.239	0.231

Table 4-2. The predicted coordinates of cyclic voltammetry current peaks at the selected bulk concentration ratios for the cyclic voltammetry results shown in Figure 4-4.

Temperature	$\frac{nF}{RT}\Delta E_p$	$\frac{C_b^{CrF_6^{3-}} D_{CrF_6^{3-}}{}^{1/2}}{C_b^{CrF_3^-} D_{CrF_3^-}{}^{1/2}}$	$\frac{\lvert i_p \rvert}{nFC_b^{CrF_6^{3-}} D_{CrF_6^{3-}}{}^{1/2}}\left(\frac{RT}{nFv}\right)^{1/2}$
-	2.236	0	0.4463
873 K Test #1	3.172	2.348	0.5631
873 K Test #2	3.053	1.976	0.5226

As shown in Table 4-2, for every value $\frac{nF}{RT}\Delta E_p$ obtained from cyclic voltammogram, there is a corresponding value for $\frac{|i_p|}{nFC_b^{CrF_6^{3-}} D_{CrF_6^{3-}}{}^{1/2}}\left(\frac{RT}{nFv}\right)^{1/2}$ and it can be used to calculate the diffusion coefficient of CrF_6^{3-} in FLiNaK melt $D_{CrF_6^{3-}}$ directly. For the system without the presence of product, the value of $\frac{C_b^{CrF_6^{3-}} D_{CrF_6^{3-}}{}^{1/2}}{C_b^{CrF_3^-} D_{CrF_3^-}{}^{1/2}}$ is 0 and $\frac{|i_p|}{nFC_b^{CrF_6^{3-}} D_{CrF_6^{3-}}{}^{1/2}}\left(\frac{RT}{nFv}\right)^{1/2} = 0.4463$ which is the Randles equation (4-3) commonly used. Figure 4-5 shows in the linear relationship between the cathodic current peaks $i_{p,c}$ and the square root of scan rate v at the temperature of 873 K. The slope of that linear correlation can be used to determine the diffusion coefficients $D_{CrF_6^{3-}}$ which is 8.76×10^{-6} cm^2/s on average at 873 K. Based on the obtained $D_{CrF_6^{3-}}$, the diffusion coefficient for CrF_3^- in molten FLiNaK can be obtained from the values of $\frac{C_b^{CrF_6^{3-}} D_{CrF_6^{3-}}{}^{1/2}}{C_b^{CrF_3^-} D_{CrF_3^-}{}^{1/2}}$ listed in the third column of Table 4-2. The acquired $D_{CrF_3^-}$ is 4.27×10^{-5} cm^2/s on average at 873 K.

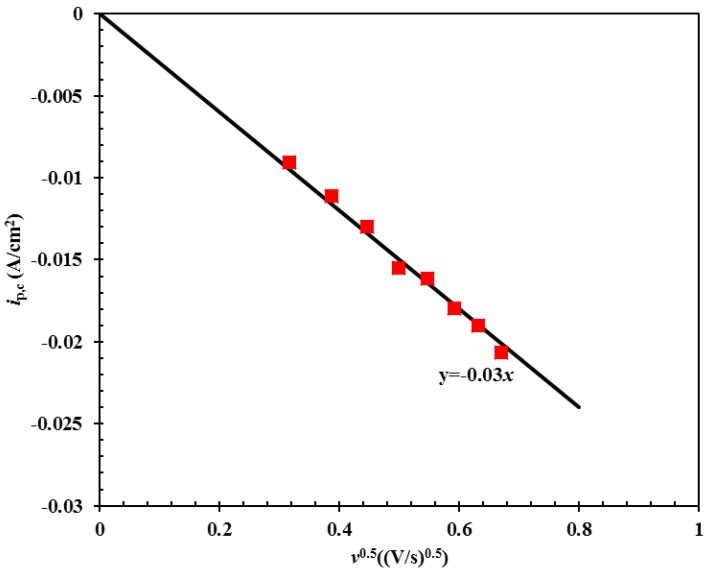

Figure 4-5. Linear relationship of $i_{p,c}$ versus $v^{0.5}$ for the cyclic voltammogram given in Figure 4-4.

Chronopotentiometry test can also be used to study the thermodynamic properties of CrF_6^{3-} and CrF_3^- in FLiNaK. As discussed before, there are two charge reactions which happen for CrF_6^{3-} when applying a reduction current: $CrF_6^{3-}+e^- \leftrightarrow CrF_3^-+3F^-$ and $CrF_3^-+2e^- \leftrightarrow Cr+3F^-$. It is found that the plateau for the first charge reaction $CrF_6^{3-}+e^- \leftrightarrow CrF_3^-+3F^-$ is not easy to be identified from Figure 4-3. In order to obtain an obvious potential transition and then confirm the transition time for the first charge reaction, small currents were applied here. Figure 4-6 shows the typical chronopotentiograms for charge reaction of $CrF_6^{3-}+e^- \leftrightarrow CrF_3^-+3F^-$ obtained at the temperature of 873 K. Whereas, higher currents were applied for obtaining the potential transition of the charge reaction $CrF_3^-+2e^- \leftrightarrow Cr+3F^-$, the typical resulting chronopotentiograms are shown in Figure 4-7.

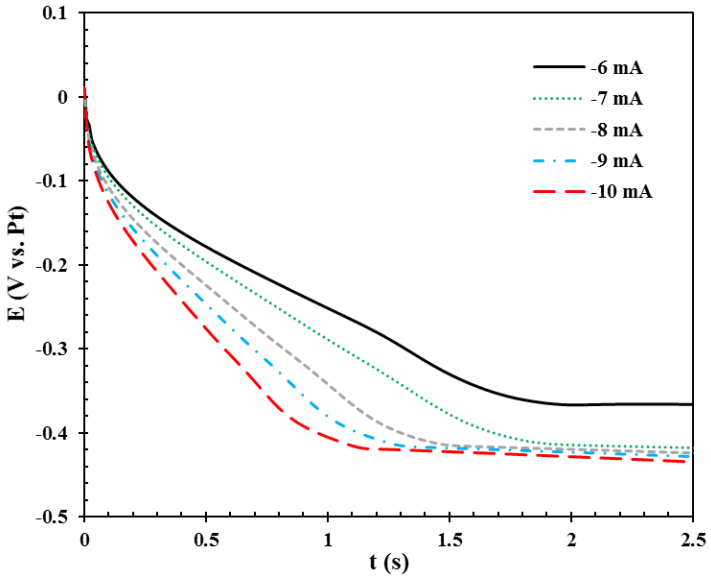

Figure 4-6. Typical chronopotentiograms for reaction of $CrF_6^{3-}+e^- \leftrightarrow CrF_3^-+3F^-$ at 873 K for molten FLiNaK salt with addition of 9.08×10^{-5} mol/cm^3 CrF_2. Electrode area=0.5417 cm^2.

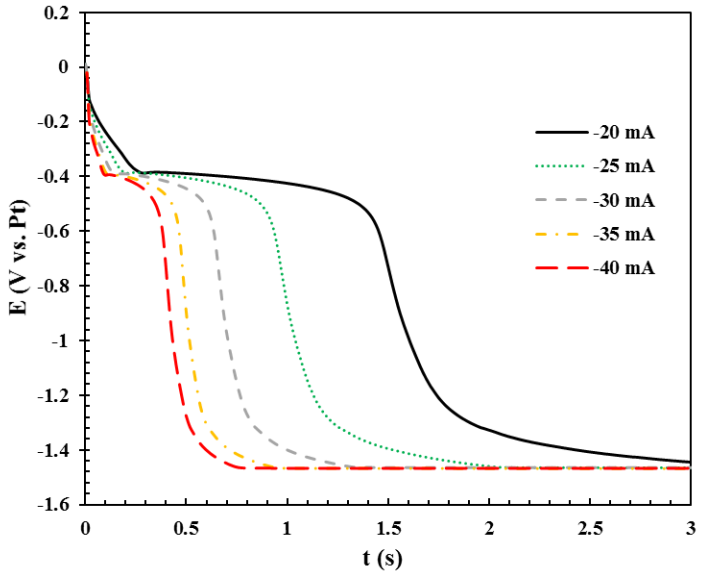

Figure 4-7. Typical chronopotentiograms for reaction of $CrF_3^-+2e^-\leftrightarrow Cr+3F^-$ at 873 K for molten FLiNaK salt with addition of 9.08×10^{-5} mol/cm^3 CrF_2. Electrode area=0.5417 cm^2.

In chronopotentiometry test, the transition time can be determined from the chronopotentiogram using the method described in the literature [135]. The plots of I versus $\tau^{-1/2}$ in Figure 3-3 exhibit a linear relationship passing through the origin point. The Sand's equation [131] is applicable for the redox reaction of CrF_6^{3-}/ CrF_3^-. Therefore, the diffusion coefficient of CrF_6^{3-} in molten FLiNaK can be calculated from the plot slope of I versus $\tau^{-1/2}$ through Sand's equation

$$I\tau^{1/2} = 0.5nFC_b^{CrF_6^{3-}}A\pi^{1/2}D_{CrF_6^{3-}}{}^{1/2} \qquad (4\text{-}6)$$

where I is the applied current, A; τ is the transition time, s; A is the working electrode surface area, cm^2.

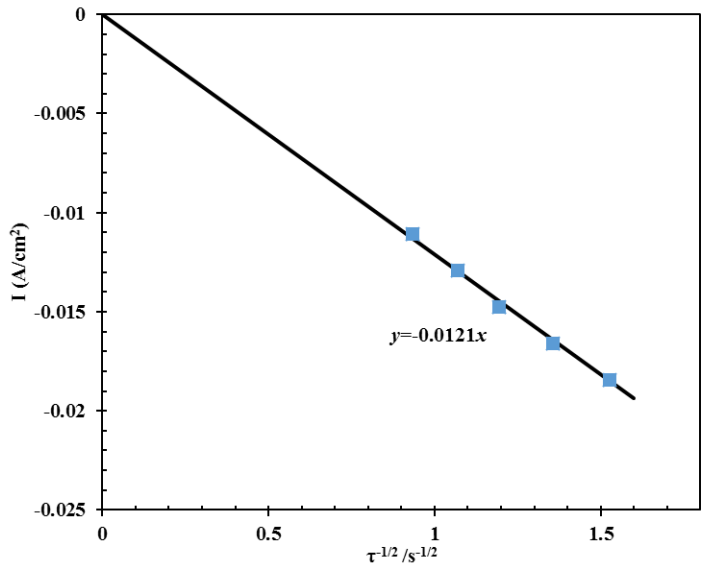

Figure 4-8. Linear relationship of I versus $\tau^{-1/2}$ for the chronopotentiometry test of redox couple CrF_6^{3-}/ CrF_3^- in molten FLiNaK salt with addition of 9.08×10^{-5} mol/cm^3 CrF_2 at 873K.

For the second charge reaction $CrF_3^- + 2e^- \leftrightarrow Cr + 3F^-$, the sand's equation which is applied for one simple charge transfer process cannot be used. For that reason, equations were derived here for two consecutive charge reactions with the presence of both reactant and intermediate product in electrolyte initially. The two charge reactions can be expressed by the following elementary processes (4-7) and (4-8):

$$A + n_1 e \leftrightarrow B \tag{4-7}$$

$$B + n_2 e \leftrightarrow C \tag{4-8}$$

If the reactant A, intermediate product B, and final product C obey Fick's law, the following initial and boundary conditions can be assumed [136,137]:

$$C_A = C_A^*, C_B = C_B^*, C_C = 0; t = 0 \tag{4-9}$$

$$C_A \to C_A^*, C_B \to C_B^*, C_C \to 0; t > 0; x \to \infty \tag{4-10}$$

$$(n_1 + n_2) D_A \frac{\partial C_A}{\partial x} + n_2 D_B \frac{\partial C_B}{\partial x} = \frac{i}{FA}; t > 0; x = 0 \tag{4-11}$$

where C_A^* and C_B^* are bulk concentrations of species A and B in electrolyte, respectively. The diffusion equations to be solved for reactions (4-7) and (4-8) are

$$\begin{cases} \dfrac{\partial C_A}{\partial t} = D_A\left(\dfrac{\partial^2 C_A}{\partial x^2}\right) \\ \dfrac{\partial C_B}{\partial t} = D_B\left(\dfrac{\partial^2 C_B}{\partial x^2}\right) \\ \dfrac{\partial C_C}{\partial t} = D_C\left(\dfrac{\partial^2 C_C}{\partial x^2}\right) \end{cases} \tag{4-12}$$

If only species A and B are initially present in the electrolyte, the Laplace transformation of Eq. (4-12) can be expressed by

$$\begin{cases} \overline{C_A}(x,s) = \dfrac{{C_A}^*}{s} + \left[\overline{C_A}(x=0) - \dfrac{{C_A}^*}{s}\right] exp\left(-\sqrt{s/D_A}x\right) \\ \overline{C_B}(x,s) = \dfrac{{C_B}^*}{s} + \left[\overline{C_B}(x=0) - \dfrac{{C_B}^*}{s}\right] exp\left(-\sqrt{s/D_B}x\right) \\ \overline{C_C}(x,s) = \overline{C_C}(x=0) exp\left(-\sqrt{s/D_C}x\right) \end{cases} \tag{4-13}$$

The Laplace transform of one boundary condition Eq. (4-11) for constant current can be given by

$$(n_1+n_2)D_A\frac{\partial\overline{C_A}(x,s)}{\partial x} + n_2 D_B\frac{\partial\overline{C_B}(x,s)}{\partial x} = \frac{i}{sFA} \tag{4-14}$$

The differentiation of Eq.(4-13) with respect to x at x=0 yields the following expression

$$\begin{cases} \left(\dfrac{\partial\overline{C_A}(x,s)}{\partial x}\right)_{x=0} = -\sqrt{s/D_A}\left[\overline{C_A}(x=0) - \dfrac{{C_A}^*}{s}\right] \\ \left(\dfrac{\partial\overline{C_B}(x,s)}{\partial x}\right)_{x=0} = -\sqrt{s/D_B}\left[\overline{C_B}(x=0) - \dfrac{{C_B}^*}{s}\right] \\ \left(\dfrac{\partial\overline{C_C}(x,s)}{\partial x}\right)_{x=0} = -\sqrt{s/D_C}\,\overline{C_C}(x=0) \end{cases} \tag{4-15}$$

Substituting Eq. (4-15) to Eq. (4-14), then Eq. (4-16) can be obtained

$$\begin{aligned} &(n_1+n_2){D_A}^{1/2}\overline{C_A}(x=0) + n_2{D_B}^{1/2}\overline{C_B}(x=0) \\ &\quad = (n_1+n_2){D_A}^{1/2}\frac{{C_A}^*}{s} + n_2{D_B}^{1/2}\frac{{C_B}^*}{s} - \frac{i}{s^{3/2}FA} \end{aligned} \tag{4-16}$$

The inverse Laplace transformation of Eq. (4-16) can be performed and the expression for time-dependent surface concentrations of species A and B is yielded:

$$(n_1 + n_2){D_A}^{1/2}C_A(x = 0) + n_2{D_B}^{1/2}C_B(x = 0) = (n_1 + n_2){D_A}^{1/2}{C_A}^{*} + n_2{D_B}^{1/2}{C_B}^{*} - \frac{2it^{1/2}}{\pi^{1/2}FA} \quad (4\text{-}17)$$

After the two potential transitions happen for the two charge transfer reactions, that is, at the overall transition time τ, both $C_A(x = 0)$ and $C_B(x = 0)$ drop to zero, Eq. (4-17) can be rewritten by

$$(n_1 + n_2){D_A}^{1/2}{C_A}^{*} + n_2{D_B}^{1/2}{C_B}^{*} = \frac{2i\tau^{1/2}}{\pi^{1/2}FA} \quad (4\text{-}18)$$

Based on Eq. (4-18), the diffusion coefficient of CrF_3^- in molten FLiNaK can be obtained after knowing diffusion coefficient of CrF_6^{3-} by Sand's equation (4-6). The $i\tau^{1/2}$ in Eq.(4-18) is determined by linear fitting the slope of *I* versus $\tau^{-1/2}$ with the intercept of zero. The fitting curve for the molten salt system of FLiNaK-9.08×10^{-5} mol/cm^3 CrF_2 at 873K is shown in Figure 4-9. Two replicate tests as done for cyclic voltammetry discussed above are performed in FLiNaK-9.08×10^{-5} mol/cm^3 CrF_2 molten salt system. The calculated diffusion coefficients of CrF_3^- by Eq. (4-18) as well as CrF_6^{3-} by Sand's equation (4-6) from these tests are summarized and listed in Table 4-3. The average diffusion coefficients of CrF_6^{3-} and CrF_3^- obtained from chronopotentiometry tests are 7.74×10^{-6} cm^2/s and 2.55×10^{-5} cm^2/s respectively which are close to the values of 8.76×10^{-6} cm^2/s and 4.27×10^{-5} cm^2/s achieved from cyclic voltammetry tests. The values of diffusion coefficient of CrF_6^{3-} obtained in this study are higher than the values of $(9.56\pm0.57)\times10^{-7}$ cm^2/s reported by Wu et al [124] at 973 K and 5.9×10^{-7} cm^2/s measured by Yoko et al [122] at 989 K while lower than 6.25×10^{-4} cm^2/s acquired by Wang et al [123] at 973 K. The diffusion coefficient of CrF_3^- is rarely studied before except the one predicted by Wu et al [124] where the obtained value is $(3.68\pm0.09)\times10^{-6}$ cm^2/s which is much lower than the values obtained in this study. One reason causing their underestimation could be the inappropriate use of Berzin's equation which is only applicable for the one simple charge transfer electrochemical reaction.

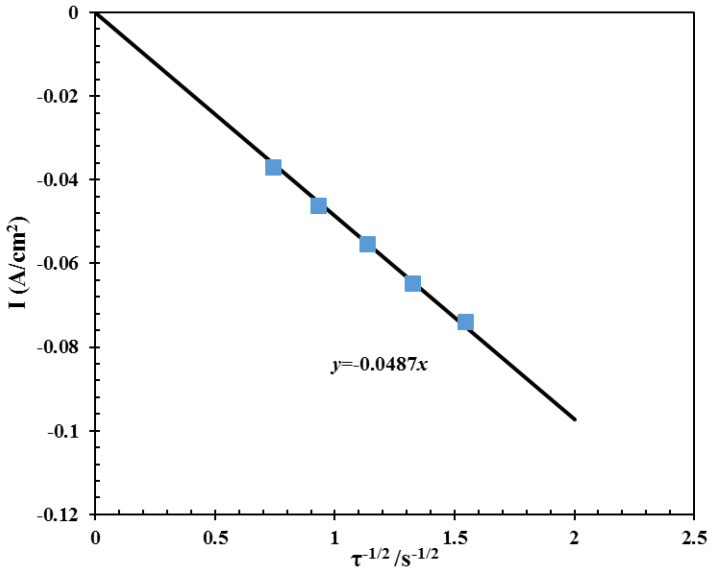

Figure 4-9. Linear relationship of I versus $\tau^{-1/2}$ for the chronopotentiometry overall reaction of CrF_6^{3-} to Cr at 873 K for FLiNaK-9.08×10^{-5} mol/cm^3 CrF_2 molten salt system.

Table 4-3. The obtained diffusion coefficients for CrF_6^{3-} and CrF_3^- from chronopotentiometry tests at the temperature of 873 K.

-	Diffusion coefficient	
	CrF_6^{3-} ($cm^2/s\times10^{-6}$)	CrF_3^- ($cm^2/s\times10^{-5}$)
Test #1	6.70	3.88
Test #2	8.77	1.22
Average	7.74	2.55

4.4. Conclusion

In this chapter, the electrochemical behaviors of CrF_2 in FLiNaK molten salt were studied by the electrochemical techniques of cyclic voltammetry and chronopotentiometry. It was found that both chromium divalent and trivalent ions presented in FLiNaK-CrF_2 molten salt, and which exist in the forms of CrF_3^- and CrF_6^{3-}, respectively. The cyclic voltammetry measurements performed for the redox reaction of CrF_6^{3-}/ CrF_3^- at 873 K showed the reversible and diffusion-controlled behavior. Considering the co-existence of CrF_3^- and CrF_6^{3-} species in FLiNaK-CrF_2 molten salt system, the conventional analytical methods such as Randles equation and Sand's equation are not applicable. Analytical methods for consecutive charge transfer electrochemical reaction with the presence of reductant and product were developed to do the data analysis of the cyclic voltammetry and chronopotentiometry results obtained in this study. Both the diffusion coefficients of CrF_6^{3-} and CrF_3^- were determined through the new analytical methods. Comparing the values obtained through the conventional analysis methods which are only applicable for the simple charge transfer reaction with reactant presented, the results obtained in this study will be more reliable. The new analytical methods could also be applied to the fundamental properties studies in other systems where both reactant and product exist, for example, the presence of both U^{4+} and U^{3+}, or presence of both Eu^{3+} and Eu^{2+} in molten salts.

5. Concentration and temperature dependent activity coefficients of fission products in liquid bismuth

5.1. Introduction

Liquid bismuth was proposed to be used to separate fission products from FLiNaK molten salt for the FHR coolant clean-up. The activity coefficient is the essential factor for assessing the viability of bismuth in separating these fission products species from molten FLiNaK salt. The current available data on the activity coefficients of fission products is for infinitely diluted solution case which is assumed to not depend on the concentration. Considering the dependence of activity coefficient on the concentration, these reported data at dilution may be far from the practical applications since the concentrations of lanthanides in liquid bismuth are usually changeable and much higher than the dilution. The present chapter focuses on the understanding of the concentration-dependence of the activity coefficients of Dy, Gd, Ho, La, Lu, Nd, Tb, and Tm in liquid bismuth based on the assessed expressions of Gibbs energy [138-143]. The activity coefficients were calculated at three temperatures (873, 923, and 973 K) and the temperature- and concentration-dependent correlations of the activity coefficients were developed by which the activity coefficient at a given concentration up to the solubility limit in the temperature range of 873 to 973 K can be calculated.

5.2. Methodology

In the thermodynamic assessment of a binary system by the method of CALPHAD, the liquid solution is generally described by the sub-regular model with the Redlich-Kister formula [144]. Its Gibbs energy can be expressed by

$$G_{real}^{liq} = x_A {G_A}^{liq,0} + x_B {G_B}^{liq,0} + RT(x_A ln x_A + x_B ln x_B) + x_A x_B \sum_{i=0}^{m} L_i^{liq} (x_A - x_B)^i \quad (5\text{-}1)$$

where ${G_A}^{liq,0}$ and ${G_B}^{liq,0}$ are the Gibbs free energy of the pure component A and B at their liquid state, respectively, x_A and x_B are the mole fraction A and B in the binary, R is the gas constant, respectively, and T is the temperature in Kelvin. L_i^{liq} is the binary interaction parameter between species A and B.

For the ideal liquid solution of a binary system, the Gibbs energy is written as

$$G_{ideal}^{liq} = x_A {G_A}^{liq,0} + x_B {G_B}^{liq,0} + RT(x_A ln x_A + x_B ln x_B) \quad (5\text{-}2)$$

Combining equation (5-1) and (5-2), the molar excess Gibbs energy is obtained with the following expression

$$\bar{G}_{excess} = G_{real}^{liq} - G_{ideal}^{liq} = x_A x_B \sum_{i=0}^{m} L_i^{liq} (x_A - x_B)^i \quad (5\text{-}3)$$

The activity coefficient of B, for example, can be calculated by the partial molar excess Gibbs energy ΔG_{excess} [145,146]:

$$RTln\gamma_B = \left(\frac{\partial G_{excess}^t}{\partial n_B}\right)_{n_A,p,T} = \left(\frac{\partial (n_A + n_B)\bar{G}_{excess}}{\partial n_B}\right)_{n_A,p,T} = \Delta G_{excess} \quad (5\text{-}4)$$

where n is mole fraction.

5.3. Results and discussion

Based on the computed parameters published for the expression of L_i^{liq} [138-143], the activity coefficients of Dy, Gd, Ho, La, Lu, Nd, Tb, and Tm in liquid bismuth were calculated by equation (5-4). In these references, L_i^{liq} was temperature-dependent and can be expressed with equations (5-5) by assuming that the excess heat capacity is zero [147].

$$L_i^{liq} = a_i + b_i T \quad (5\text{-}5)$$

where a_i and $b_i$are constants. Given the finding of that excess Gibbs energy is linearly temperature-dependent in the experiment [69], this common assumption should be close to the real situation. The substitution of L_i^{liq} in Eq. (5-5) to Eq. (5-3) reveals ΔG_{excess} is linearly temperature-dependent, corresponding to the expression of $\Delta G_{excess} = \Delta H_{mix} - \Delta S_{excess} T$. Thus, ΔH_{mix} and ΔS_{excess} can be considered as constants at a given concentration, and the relationship between the activity coefficient and temperature can be expressed by

$$ln\gamma = \frac{\Delta H_{mix}}{RT} - \frac{\Delta S_{excess}}{R} = a(x) + \frac{b(x)}{T} \quad (5\text{-}6)$$

where $a(x)$ and $b(x)$ are concentration-dependent variables. Based on the reported expressions for L_i^{liq} [138-143], the expressions of $a(x)$ and $b(x)$ can be obtained which are shown in Table 5-1. The correlations in Table 5-1 can be used to evaluate the activity coefficients of these eight lanthanides in liquid bismuth at concentrations below solubility limit.

Table 5-1. Correlations for the activity coefficients of lanthanides in liquid bismuth.

Element	$ln\gamma = a(x) + \frac{b(x)}{T}$	
	$a(x)$	$b(x)$

Dy	$0.219389x^5 + 5.27833x^4 - 15.7205x^3$ $+15.5663x^2 - 6.18138x + 0.837864$	$120098x^5 - 300974x^4 + 231603x^3$ $-60666.7x^2 + 29930.5x - 19990.7$
Gd	$-11.1026x^5 + 41.0031x^4 - 59.3434x^3$ $+41.2856x^2 - 13.0403x + 1.19763$	$115468x^5 - 305701x^4 + 273066x^3$ $-114351x^2 + 54968.9x - 23450.6$
Ho	$-12.3558x^5 + 45.0757x^4 - 64.071x^3$ $+43.8425x^2 - 13.9959x + 1.50447$	$69284.8x^5 - 144059.x^4 + 58422.4x^3$ $+19092.5x^2 + 16359.7x - 19100.4$
La	$4.57907x^3 - 9.96467x^2$ $+6.19213x - 0.806531$	$88108.5x^4 - 232720x^3 + 176307x^2$ $-6888.48x - 24807.3$
Lu	$3.3197x^2 - 6.6394x + 3.3197$	$49045x^4 - 134680x^3 + 105114x^2$ $-2367.81x - 17111$
Nd	$31.7537x^4 - 84.6764x^3 + 75.5352x^2$ $-24.0558x + 1.44335$	$76978.6x^5 - 197258x^4 + 150830x^3$ $-42278.1x^2 + 36204x - 24476.8$
Tb	$11.5468x^4 - 30.7914x^3 + 27.9047x^2$ $-9.62232x + 0.962232$	$55280.3x^4 - 140197x^3 + 92097.7x^2$ $+15275.4x - 22456.1$
Tm	$14.4335x^4 - 37.7195x^3 + 36.1418x^2$ $-16.859x + 4.00325$	$57012.3x^4 - 152995x^3 + 116039x^2$ $-1142.89x - 18913.8$

Figure 5-1 presents the calculated results of activity coefficients of Dy, Gd, Ho, La, Lu, Nd, Tb, and Tm in liquid bismuth at the temperatures of 973, 923, and 873 K. Equations (5-3) and (5-4) show molar excess Gibbs energy and the activity coefficient will stay constant with increasing mole fraction when the solute (lanthanides) reaches the solubility limit and intermetallic compounds were formed between bismuth and solute (lanthanides). The solubility limit of the lanthanides studied is provided in Table 5-2. The activity coefficient was calculated at the concentration up to solubility limit in the study. Figure 5-1 indicates that activity coefficients of most of those elements except Lu and Tb increase with increasing mole fraction. Activity coefficients of Lu and Tb decrease initially and then increase with the increasing mole fraction. Good linearity between the logarithmic activity coefficient and the mole fraction was observed for Dy, Gd, and Nd at all temperatures, as shown in Figure 5-1.

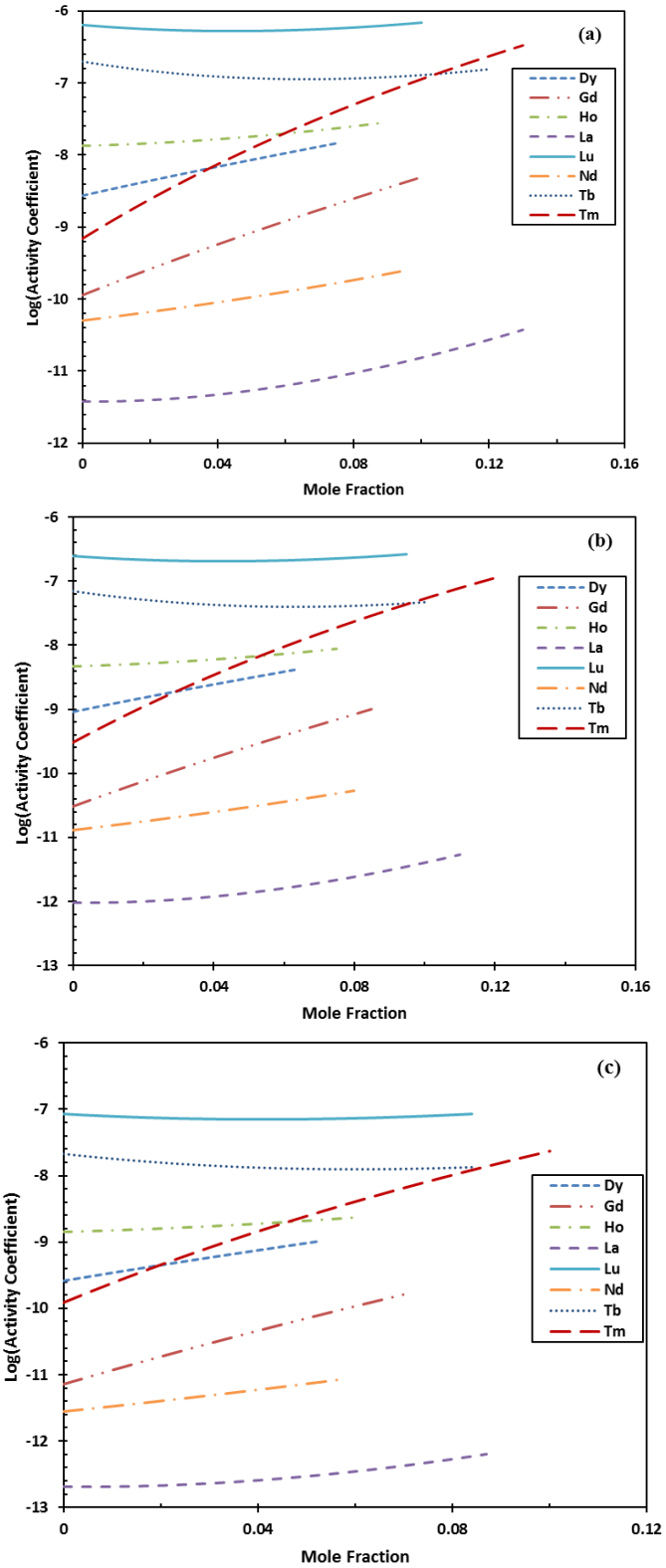

Figure 5-1. Relationship between logarithms of activity coefficient and mole fraction of lanthanides in liquid bismuth at the temperatures of 973 K (a), 923 K (b), and 873 K (c).

Table 5-2. Solubility limit of lanthanides in liquid bismuth at the temperatures of 873 K, 923 K, and 973 K.

Ref.	Element	Solubility limit (mole fraction %)		
		873 K	923 K	973 K
[138]	Dy	5.3	6.3	7.5
[139]	Gd	7.0	8.5	10.0
[139]	Ho	6.0	7.5	9.0
[140]	La	8.7	11.0	13.0
[141]	Lu	8.4	9.5	10.0
[142]	Nd	5.8	8.0	9.5
[143]	Tb	8.5	10.0	12.0
[142]	Tm	10.0	12.0	13.0

Two parameters influencing the concentration-dependence of the activity coefficient are interaction parameter L_i^{liq} and maximum power *m* in equation (5-3). Obviously, L_i^{liq} is independent of the mole fraction of species. It works as a constant term affecting the relationship between the activity coefficient and concentration at a given temperature. However, the value of maximum power *m* required to characterize a system can be different to fit a system in the practical optimization. These two factors explain why the variation trends of activity coefficients for different elements are different in Figure 5-1. The difference on the value of maximum power *m* for different cases determines that there is no common definite correlation to express the relationship between the activity coefficient and concentration for all the elements studied.

Figure 5-1 also shows the important role of temperature on the value of the activity coefficient. For all of these eight lanthanides in liquid bismuth, the mixing enthalpy of liquid decreases with the mole fraction of lanthanides in bismuth at concentrations below solubility. As a result, the value of ΔH_{mix} or *b* in equation (5-6) is negative. That is why activity coefficients of these lanthanides in liquid bismuth at a higher temperature have a larger value.

The Calculated activity coefficients of Dy, Gd, Ho, La, Lu, Nd, Tb, and Tm in liquid bismuth at the concentration up to its solubility limit are summarized and compared with the available literature data in Table 5-3 to Table 5-5, respectively. Considering activity coefficients of these elements are very small, the calculated results should be reasonable and acceptable if the calculated activity coefficients are at the same order of magnitude as the published literature data. Table 5-3 to Table 5-5 show that the calculated activity coefficients of Dy, Gd, Ho, La, and Nd in liquid bismuth are in good agreement with the values reported by others. The overestimated activity coefficient of terbium (Tb) may be attributed to the not very good optimized parameters for L_i^{liq} [143]. Based on the authors' knowledge, there was no reported data for Lu and Tm in liquid bismuth.

Table 5-3. Activity coefficients of lanthanides in liquid bismuth at 873 K.

Element	Mole fraction	Log(activity coefficient)	Studies
Dy	0~0.053	-9.58~-8.98	This study

	0.005	-9.85	[79]
	0.005	-10.16	[69]
Gd	0~0.070	-11.15~-9.78	This study
	0.0006	-10.12	[77]
	0.005	-10.18	[69]
	Dilution	-10.4	[76]
	Dilution	-10.06	[78]
	Dilution	-9.78	[72]
	Dilution	-10.10	[73]
Ho	0~0.060	-8.85~-8.62	This study
	0.005	-9.7	[80]
	0.001	-9.43	[81]
La	0~0.087	-12.69~-12.20	This study
	0.005	-11.79	[69]
	Dilution	-11.84	[70]
	Dilution	-11.65	[71]
	Dilution	-11.73	[72]
	Dilution	-11.75	[73]
Lu	0~0.084	-7.15~-7.07	This study
Nd	0~0.058	-11.55~-11.06	This study
	0.005	-12.03	[74]
	Dilution	-10.78	[75]
	Dilution	-10.94	[76]
Tb	0~0.085	-7.90~-7.67	This study
	0.005	-9.95	[69]
Tm	0~0.100	-9.91~-7.63	This study

Dilution: mole fraction is less than 1 at%.

Table 5-4. Activity coefficients of lanthanides in liquid bismuth at 923 K.

Element	Mole fraction	Log(activity coefficient)	Studies
Dy	0~0.063	-9.04~-8.39	This study
	0.005	-9.26	[79]
	0.005	-9.53	[69]
Gd	0~0.085	-10.51~-9.00	This study
	Dilution	-9.47	[77]
	0.005	-9.53	[69]
	Dilution	-9.75	[76]
	Dilution	-9.45	[78]
	Dilution	-9.22	[72]
	Dilution	-9.48	[73]
Ho	0~0.075	-8.33~-8.06	This study
	0.005	-9.09	[80]
	0.001	-8.88	[81]
La	0~0.110	-12.02~-11.27	This study
	0.005	-11.07	[69]

	Dilution	-11.15	[70]
	Dilution	-10.93	[71]
	Dilution	-11.01	[72]
	Dilution	-11.04	[73]
Lu	0~0.095	-6.69~-6.58	This study
Nd	0~0.080	-10.89~-10.27	This study
	0.005	-11.28	[74]
	Dilution	-10.10	[75]
	Dilution	-10.23	[76]
	Dilution	-8	This study
Tb	0~0.100	-7.40~-7.16	[69]
	0.005	-9.30	This study
Tm	0~0.120	-9.52~-6.95	This study

Dilution: mole fraction is less than 1 at%.

Table 5-5. Activity coefficients of lanthanides in liquid bismuth at 973 K.

Element	Mole fraction	Log(activity coefficient)	Studies
Dy	0~0.075	-8.56~-7.84	This study
	0.005	-8.73	[79]
	0.005	-8.96	[69]
Gd	0~0.100	-9.95~-8.31	This study
	Dilution	-8.92	[77]
	0.005	-8.94	[69]
	Dilution	-9.17	[76]
	Dilution	-8.90	[78]
	Dilution	-8.72	[72]
	Dilution	-8.93	[73]
Ho	0~0.090	-7.87~-7.54	This study
	0.005	-8.54	[80]
	0.001	-8.39	[81]
La	0~0.130	-11.42~-10.43	This study
	0.005	-10.42	[69]
	Dilution	-10.53	[70]
	Dilution	-10.28	[71]
	Dilution	-10.37	[72]
	Dilution	-10.40	[73]
Lu	0~0.100	-6.28~-6.16	This study
Nd	0~0.095	-10.30~-9.61	This study
	0.005	-10.61	[74]
	Dilution	-9.48	[75]
	Dilution	-9.59	[76]
Tb	0~0.120	-6.95~-6.70	This study
	0.005	-8.72	[69]
Tm	0~0.130	-9.17~-6.48	This study

Dilution: mole fraction is less than 1 at%.

The relationships between the activity and the concentration were also investigated. Here only the activities at 973 K were plotted and analyzed in Figure 5-2 because of the similar change patterns of activity coefficients with concentrations at three temperatures for each lanthanide as shown in Figure 5-1. Similar to the previous study of Pr, Ce, and Er [148], a unit-slope diagonal line is not indicated in the coordinate of Figure 5-2. It means the change of the activity with concentration is far away from Raoult's law [149,150]. Raoult's law [149,150] states that the activity of a component in liquid mixture is related to its activity of pure substance and its mole fraction in the solution.

$$\alpha = x\alpha^0 \tag{5-7}$$

where α^0 is the activity of the pure component and can be taken as unity, and x is the mole fraction of the component. It is only applicable to an ideal solution where there is no intermolecular interaction between particles or each intermolecular interaction equals those of the pure components [149,150]. The systems investigated with relatively low concentration in the study do not obey this law. For a real solution of lanthanide-bismuth mixture, the activity coefficient γ_{Ln} needs to be introduced. It denotes the deviation from the ideal solution. Now we have

$$\alpha_{Ln} = x_{Ln}\gamma_{Ln}\alpha_{Ln}^0 \tag{5-8}$$

When the mole fraction of solute approaches 1, the solution can be treated approximately as ideal solution and the activity coefficient of solute approaches unity. When comparing equations (5-7) and (5-8) and considering activity coefficients of these lanthanides in liquid bismuth are extremely low, there is thus a dramatically negative deviation of these systems from the ideal ones. Therefore, the interactions between the unlike atoms are significantly different from these between like atoms. Generally, more energy would be released for the attraction set up between unlike atoms compared with breaking the originally like atom pairs. It results in an exothermic enthalpy of mixing and explains the negative values of enthalpies of mixing for these binary systems reported before [138-143].

It should be noted that at infinite dilution (x_{Ln} approaches 0), the activity coefficient will have a constant value of γ_{Ln}^{∞}. In this region, the system can be depicted by Henry's law [151]

$$\alpha_{Ln} = x_{Ln}K_H \tag{5-9}$$

where Henry's constant K_H is used. Comparing equation (5-8), the activity coefficient γ_{Ln}^{∞} can be expressed by

$$\gamma_{Ln}^{\infty} = K_H/\alpha_{Ln}^0 \tag{5-10}$$

It indicates the activity coefficient is a constant in infinite dilution and there is a linear relationship between the activity and concentration. As shown in Figure 5-2, if focusing on the infinite dilution, activities show linear relationships with concentrations at infinite dilution. Upon the infinite dilution, neither Raoult's law nor Henry's law is necessarily

followed. Another interesting thing observed is that the activities increase faster than the linear relationship at low concentration for all elements except Lu and Tb. Further theoretical or experimental studies maybe needed to thoroughly understand it.

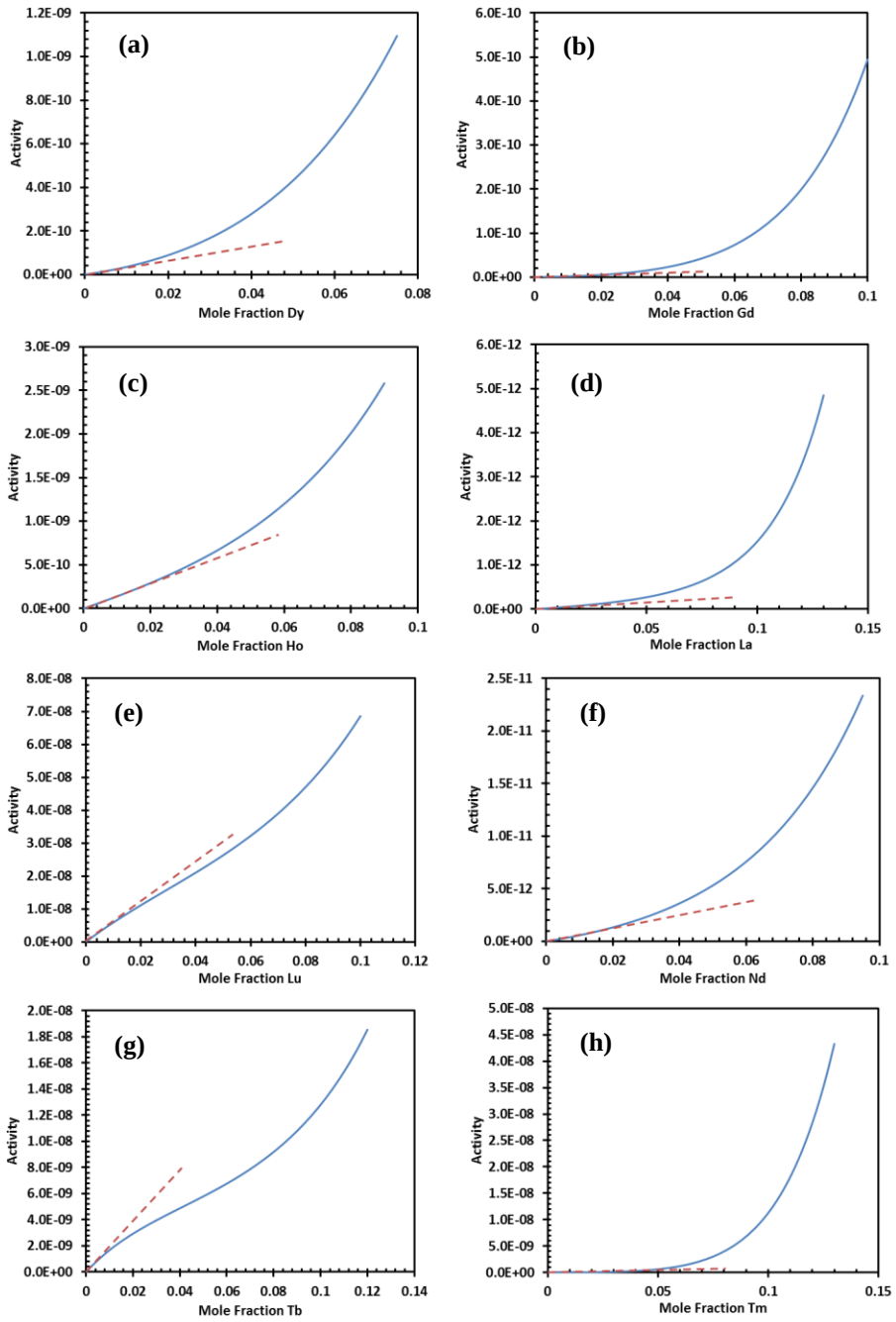

Figure 5-2. The activities of lanthanides in liquid bismuth at the temperature of 973 K. Solid line is the activity at different concentration while the dashed line is the linear relationship of the activity with concentration at dilution.

5.4. Conclusion

In this chapter, the activity coefficients of fission products in liquid bismuth at different concentrations and temperatures were studied based on the assessed results for Gibbs energy of solution by CALPHAD method. It is found that the activity coefficients of Dy, Gd, Ho, La, Nd, and Tm in liquid bismuth increase with the increasing concentration, while the activity coefficients of Lu and Tb increase initially and then decrease with the increasing concentration. Correlations for the activity coefficients were also obtained for the concentration range up to the solubility limit and the temperature range of 873-973 K. The obtained activity coefficients over a wide concentration and temperature would greatly contribute to the FHR primary coolant cleanup system development.

6. Concentration-dependent activity coefficients of K and Li in liquid bismuth determined by EMF measurement

6.1. Introduction

Liquid bismuth has broad applications in the nuclear field. Massive studies have been carried out to study the activity and activity coefficients of fission products and actinides in liquid bismuth [73]. However, most of these studies are for infinitely diluted solution cases. Based on the concentration-dependence of activity coefficient [148], the reported data at dilution in the previous studies may not be enough for the practical applications of liquid bismuth in the nuclear industry field. Therefore, it is necessary to find a way to study the variations of activity coefficients with concentrations in liquid bismuth. The present study developed an innovative experiment method to measure in-situ the activity and activity coefficient at different concentrations. By coulometric titrating different quantities of target metal into liquid bismuth and performing EMF measurement followed by each titration, the activity and activity coefficient at different concentrations can be obtained efficiently and accurately. Considering the activity and activity coefficient of K and Li in liquid bismuth also need to be known for identifying whether the target fission products and actinides can be preferentially deposited over K and Li, the present study took K and Li as examples to measure their activity and activity coefficients at different concentrations and temperatures by the developed experiment method. It should be noted that this developed experiment method can also be used for the activity and activity coefficient studies of actinides, fission products, and other metals in liquid metal.

Several relevant experimental studies have been conducted to report the activity and activity coefficient of K in liquid bismuth. A Petric et al [152] investigated the variation of the activity coefficient of K in liquid Bi-K in the composition range of 0~66 mol% K at the temperature of 873 K using electromotive force measurement (EMF). The activity coefficient of K in liquid bismuth at a high concentration (> 20 mol% K) for the temperatures of 848 K and 1023 K are reported by Hultgren et al [153] and Egan et al [154], respectively. The activity and activity coefficient studies of Li in liquid bismuth have been limited to a few concentration points at the temperatures of 800, 850, and 1000 K by Foster et al [155] and Demidov et al [156]. In the present study, by coulometric titrating different quantities of K and Li into liquid bismuth from molten salt electrolyte, the various concentrations of K and Li in liquid bismuth can be acquired and then the EMF measurements were conducted followed by each titration. Thus, the variations of activity and activity coefficient of K and Li in liquid bismuth as a function of concentration were obtained. All measurements were conducted at temperatures of 973 K and 1023 K and concentrations less than 20 mol%.

6.2. Experimental

All experiments and sample preparations were carried out under argon atmosphere in a glovebox (Inert Technology) where the moisture and oxygen levels were maintained under 0.5 ppm and 5 ppm, respectively.

6.2.1. Preparation of the electrolyte

For the investigation of the activity of K in liquid Bi, the LiF-NaF-KF (46.5 mol% LiF, 11.5 mol% NaF, and 42 mol% KF) salt melt was used as electrolyte, which was prepared by mixing lithium fluoride (>99.0% purity, Sigma Aldrich), sodium fluoride (>99.0% purity, Sigma Aldrich) and potassium fluoride (>99.5% purity, Sigma Aldrich). In the salt preparation, the LiF, NaF, and KF salt powder was mixed well before transferred to a nickel crucible and placed in a muffle furnace (Thermofisher Scientific FB1315M) for which the temperature can be maintained within ± 1 ℃ during the experiment. To remove the moisture and oxygen inside the salt powder, the salt mixture was dehydrated at 673 K for 24 hours before melting to the target temperature (973 K and 1023 K). For the activity study of Li in liquid Bi, the LiF-LiCl (52 mol% LiF-48 mol% LiCl) salt melt was used as electrolyte. It was prepared by mixing lithium fluoride (>99.0% purity, Sigma Aldrich) and lithium chloride (>99.0% purity, Sigma Aldrich). In order to do the moisture and oxygen removal, a similar dehydration process as done in LiF-NaF-KF salt was performed in this salt mixture.

6.2.2. Electrochemical apparatus and electrodes

The electrochemical tests were carried out using a Gamry Interface 1000 Potentiostat and a standard three-electrode setup. A 3.05 mm diameter graphite rod (99.9995% purity, Alfa Aesar) was used as the counter electrode for all the electrochemical experiments in this study. To perform the activity measurement of K in liquid Bi, a new reference electrode was designed as shown in Figure 6-1. Considering the low melting and boiling points of K, it is easy for K metal to vaporize away if the Bi-K liquid mixture is simply prepared by mixing K and Bi solid metals and heating up. To solve this issue, a sophisticated preparation procedure was proposed here. Bi (granule, ≥ 99.99 purity, Sigma Aldrich) metal was heated individually to 673 K in a glassy carbon crucible using a muffle furnace. K (ingot, 99.95% purity, Sigma Aldrich) metal was then added into the liquid bismuth and the formed Bi-K melt mixture was kept at 673 K for 2 hours to get Bi and K uniformly mixed. After that, the well mixed Bi-K was cooled down and grounded into granules using mortar and pestle. Thus, the well mixed Bi-K granule was obtained, and the concentration of K was identified to be 3.8 mol% by ICP-MS test. A small amount of the prepared Bi-K granules (~1.5g) was placed at the bottom of the alumina tube (9 mm OD×6 mm ID, LSP Industrial Ceramics, Inc.) which has a hole drilled on the wall. At high temperature, Bi-K granules will melt, and the molten salt electrolyte can contact the Bi-K liquid metal through the drilled hole when the whole equipment in Figure 6-1 is immersed into molten salt. The performed experiment shows the alumina tube works well for this study although it is known alumina would not work for long term operation in molten fluoride salts. An inert material: tungsten which does not have any reaction with Bi or K was chosen as the electrical wire. The tungsten electrical wire was immersed into the Bi-K melt allowing the current to flow through during the electrochemical tests. An alumina insulation tube

(CoorsTek, 2 mm OD×1.02 mm ID) was sheathed on this electrical wire to avoid its contact with molten salt. Two kinds of working electrodes were utilized for the activity study of K in liquid Bi, the first one is a 1 mm diameter tungsten rod (Midwest Tungsten Service, >99.5% purity) while the other one is liquid bismuth which is contained in the same equipment for reference electrode as shown in Figure 6-1. To guarantee the free diffusion of ions from molten salt to liquid Bi working electrode, unlike the only one hole drilled at the bottom of alumina tube shown in Figure 6-1, two holes were drilled for the equipment used to contain liquid Bi. For the activity measurement of Li in liquid Bi, the same procedure and equipment as employed for the study of K were used for the preparation of Bi-Li reference electrode (x(K)=10.5 mol%) and liquid Bi working electrode. In addition, another working electrode: tungsten rod (1 mm D, Midwest Tungsten Service, >99.5% purity) was used for the activity study of Li in liquid Bi.

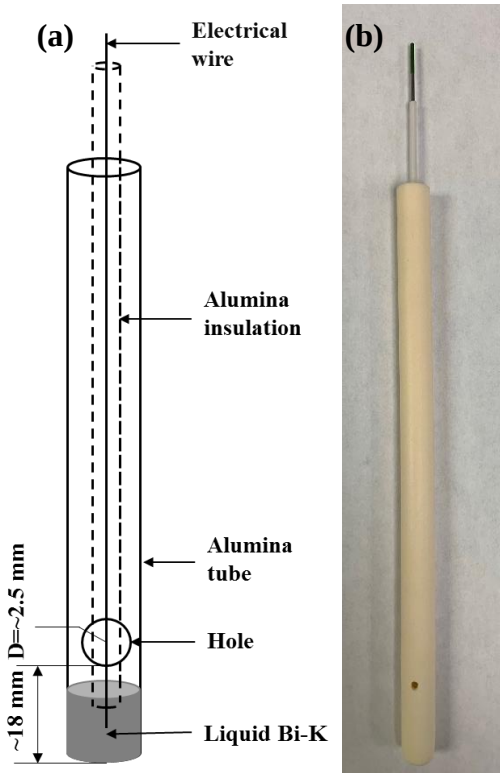

Figure 6-1. Schematic diagram of the designed Bi-K liquid reference electrode.

6.3. Results and Discussions

6.3.1. The Bi-K system

To obtain the information about the activity of K in the reference electrode, EMF measurement was carried out on a tungsten working electrode. The basic cell reaction can be expressed by

K-Bi (reference electrode) || FLiNaK electrolyte || W (working electrode).

During the EMF measurement, a 5-s current pulse was applied between the tungsten working electrode and graphite counter electrode in FLiNaK molten salt system. Figure 6-2 shows the potential evolution of the tungsten working electrode against K-Bi reference electrode over time when different current pulses were applied at the temperatures of 973 K and 1023 K. In the period that 5-s current pulse was applied, the potential of the working electrode dropped to a more negative value sharply because a potassium layer was formed on the tungsten electrode surface due to the reduction of K (I). The formed plateau during the first 5 s period in Figure 6-2 means a potassium layer is fully covered on the tungsten working electrode. A lower potential value for the plateau was observed at a higher pulse current which is attributed to the ohmic drop in the electrolyte between the tungsten working electrode and K-Bi reference electrode [157]. After 5 s, the potential steps up since the ohmic drop associated with the applied current pulse does not exist. This potential value corresponds to the equilibrium potential of K (I)/ K referring to K-Bi reference electrode which can be expressed by

$$EMF = E^{eq}_{K^+/K} - E^{eq}_{K^+/K-Bi(RE)} = \frac{RT}{F}\ln(\alpha_{K\ in\ RE}) \tag{6-1}$$

where $E^{eq}_{K^+/K}$ and $E^{eq}_{K^+/K-Bi(RE)}$ are the equilibrium potential of K(I)/K and K(I)/K-Bi (reference electrode) which are written as

$$E^{eq}_{K^+/K} = E^o + \frac{RT}{F}\ln\left(\frac{\alpha_{K^+\ in\ FLiNaK}}{1}\right) \tag{6-2}$$

$$E^{eq}_{K^+/K-Bi(RE)} = E^o + \frac{RT}{F}\ln\left(\frac{\alpha_{K^+\ in\ FLiNaK}}{\alpha_{K\ in\ RE}}\right) \tag{6-3}$$

in which E^o is the standard reduction potential, α is activity.

It means if the stepped-up potential value after the cease of the applied current pulse is known, the activity $\alpha_{K\ in\ RE}$ can be obtained directly. The activity of K in the reference electrode was calculated and listed in Table 6-1 based on equation (6-1) and the measured stepped-up potential value. The stepped-up potential will stay constant for a while and the duration time depends on the quantity of potassium deposited on the tungsten working electrode. After a certain time, the potential increases back to its initial value because of the dissolution of the deposited potassium layer on the tungsten electrode.

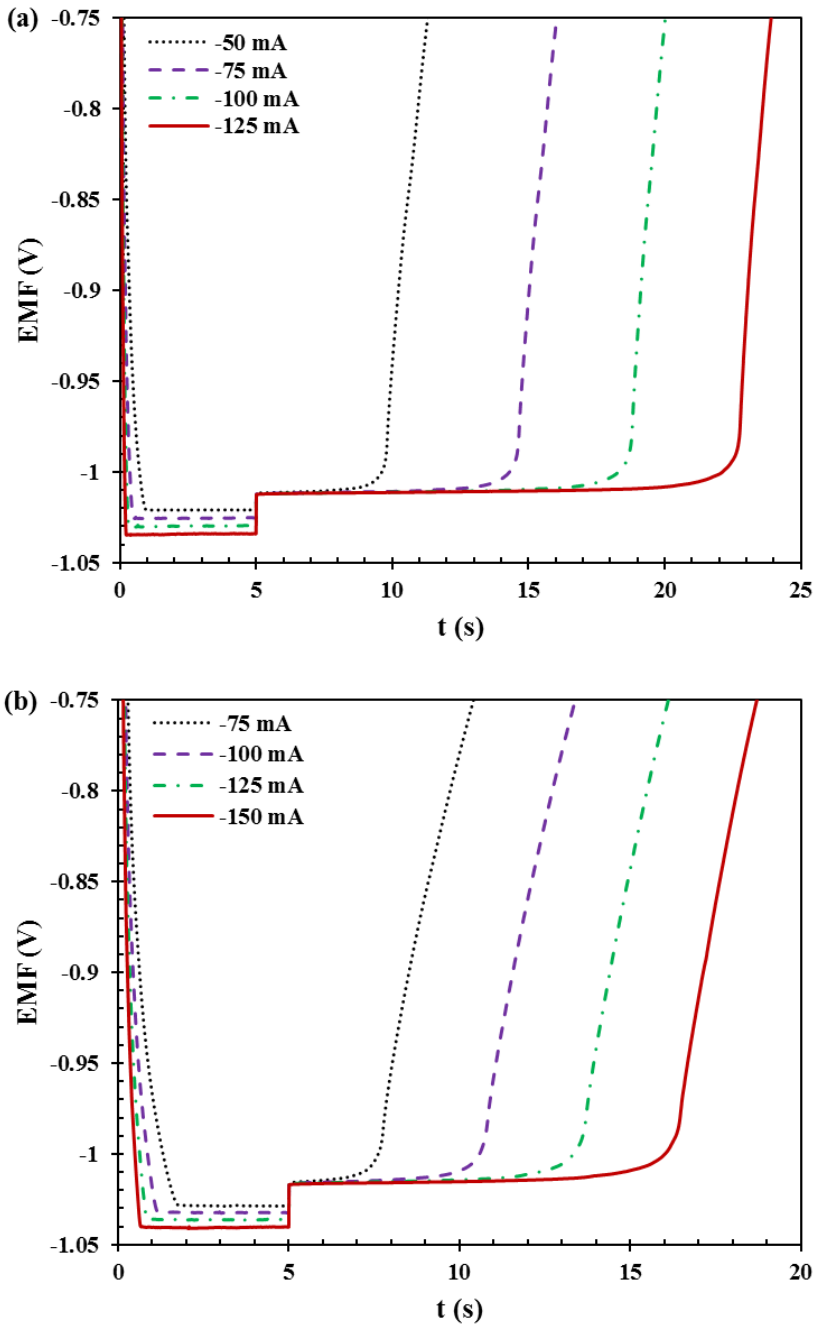

Figure 6-2. Potential evolution of the tungsten working electrode against K-Bi reference electrode over time in FLiNaK molten salt when a 5-s pulse current was applied at (a) 973 K and (b) 1023 K.

Table 6-1. Activity and activity coefficient of K in reference electrode at the temperatures of 973 K and 1023 K.

T (K)	EMF (V)	$\alpha_{K\ in\ RE}$	$x_{K\ in\ Bi}$	$\gamma_{K\ in\ RE}$

973	-1.012	5.73×10^{-6}	0.0379	1.51×10^{-4}
1023	-1.016	9.87×10^{-6}	0.0379	2.60×10^{-4}

Once the activity of K in the reference electrode was known, the working electrode was replaced with liquid Bi. The basic cell reaction then can be expressed as

K-Bi (reference) || FLiNaK electrolyte || liquid Bi (working).

To get different Bi-K ratios, coulometric titration was used to titrate K into the liquid Bi working electrode by applying a constant current during the EMF measurement. The accuracy of the coulometric titration method in molten salt system has been verified in the previous study [158]. Figure 6-3 (a) shows the typical coulometric titration EMF data at the temperature of 973 K in which a constant current of -50 mA was applied for 100 s to titrate K into liquid Bi working electrode (1.745 g) and a subsequent 1800 s open circuit potential was measured following each titration. Similarly, coulometric titration of K into liquid Bi (1.289 g) in FLiNaK molten salt electrolyte at current of -35 mA for 100 s followed by a 3600 s open circuit potential measurement was also performed at the temperature of 1023 K (Figure 6-3 (b)). From the open circuit potential measurement following each titration, the equilibrium electrode potentials as a function of K mole fraction are extracted and shown in Figure 6-4. The equilibrium electrode potential which refers to K-Bi reference electrode (K=3.79 mol%) can be expressed as

$$EMF = E^{eq}_{K^+/K-Bi(WE)} - E^{eq}_{K^+/K-Bi(RE)} = \frac{RT}{F}\ln\frac{\alpha_{K\ in\ RE}}{\alpha_{K\ in\ Bi}} \tag{6-4}$$

where $E^{eq}_{K^+/K-Bi(WE)}$ is the equilibrium potential of K (I) /K-Bi (working electrode) which can be written as

$$E^{eq}_{K^+/K-Bi(WE)} = E^o + \frac{RT}{F}\ln\left(\frac{\alpha_{K^+\ in\ FLiNaK}}{\alpha_{K\ in\ Bi}}\right) \tag{6-5}$$

Combining equation (6-4) and the known $\alpha_{K\ in\ RE}$ listed in Table 6-1, the activity of K in liquid Bi $\alpha_{K\ in\ Bi}$ at different concentrations for the temperatures of 973 K and 1023 K are obtained and shown in Figure 6-5 (a). Figure 6-5 (b) shows the calculated activity coefficient of K in liquid Bi $\gamma_{K\ in\ Bi}$ based on equation (6-6)

$$\gamma_{K\ in\ Bi} = \alpha_{K\ in\ Bi}/x_{K\ in\ Bi} \tag{6-6}$$

where the molar fraction of K in liquid Bi can be derived from the quantity of the titrated K by

$$x_{K\ in\ Bi} = \frac{It/F}{It/F + n_{Bi}} \tag{6-7}$$

in which I is the titration current applied, t is the time duration of the applied current, and n_{Bi} is the mole number of Bi for the working electrode used.

As shown in Figure 6-5, both $\alpha_{K\ in\ Bi}$ and $\gamma_{K\ in\ Bi}$ vary with concentration. It increases with the increasing concentration for $\alpha_{K\ in\ Bi}$ while initially decreases and subsequently increases for $\gamma_{K\ in\ Bi}$. To validate the results obtained in this study, the activity and activity coefficient of K in liquid Bi as a function of concentration at 873 K measured by A Petric et al [152] are also presented in Figure 6-5. Recently, Niu et al [159] performed the thermodynamic assessment of the Bi-K system using the CALculation of PHAse Diagrams (CALPHAD) method. Based on the assessed expression of Gibbs free energy, the activity and activity coefficient of K in liquid Bi in the concentration range of 0 to 18 mol% for the temperatures of 973 K and 1023 K were calculated and shown in Figure 6-5. The comparison exhibited in Figure 6-5 (a) indicates the activity $\alpha_{K\ in\ Bi}$ obtained through the experiment in this study agrees well with the ones attained from model and A Petric et al [152]. Figure 6-5 (b) shows the variation trend of activity coefficient $\gamma_{K\ in\ Bi}$ with concentration at low concentration in our study is a little different with the ones attained from model and A Petric et al [152]. However, considering the values of activity coefficient $\gamma_{K\ in\ Bi}$ shown in Figure 6-5 (b) are all at the same order, the activity coefficient obtained in this study is still reasonable.

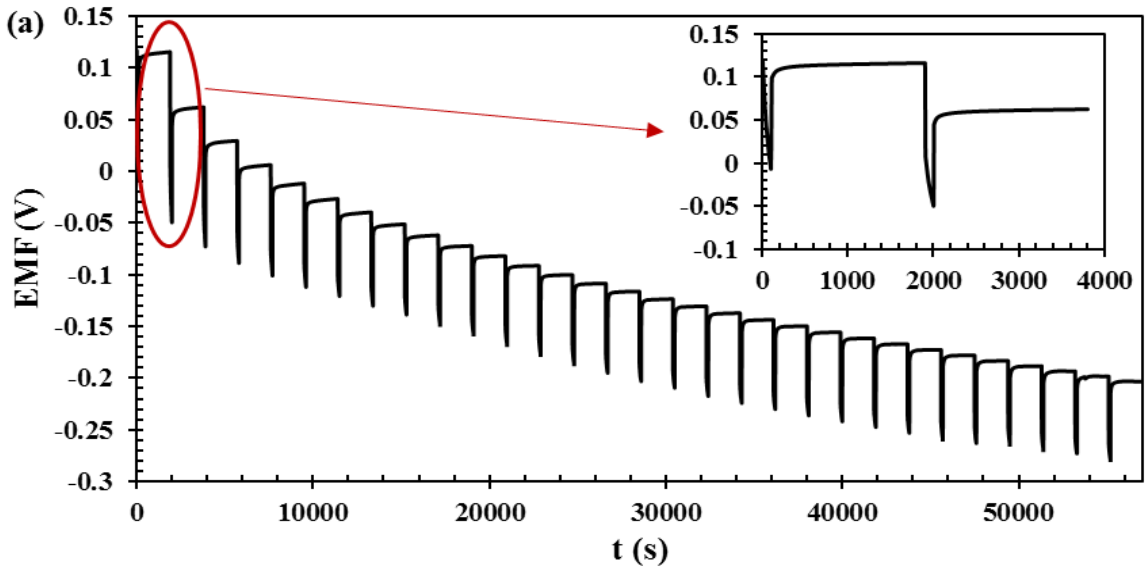

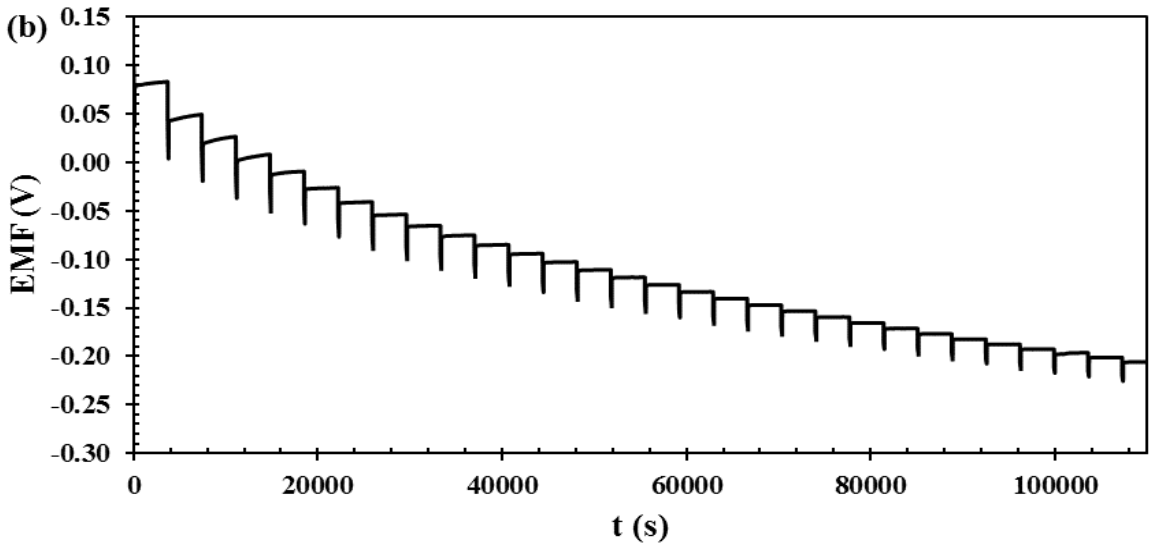

Figure 6-3. Coulometric titration of K into liquid Bi working electrode in FLiNaK electrolyte at (a) 973 K and (b) 1023K.

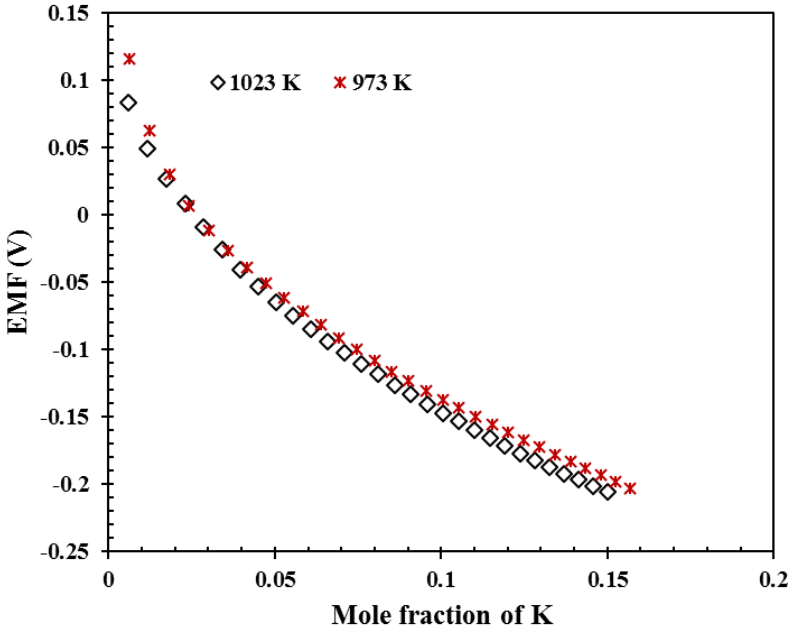

Figure 6-4. Equilibrium electrode potential as a function of K mole fraction upon K deposition at 973 K and 1023K.

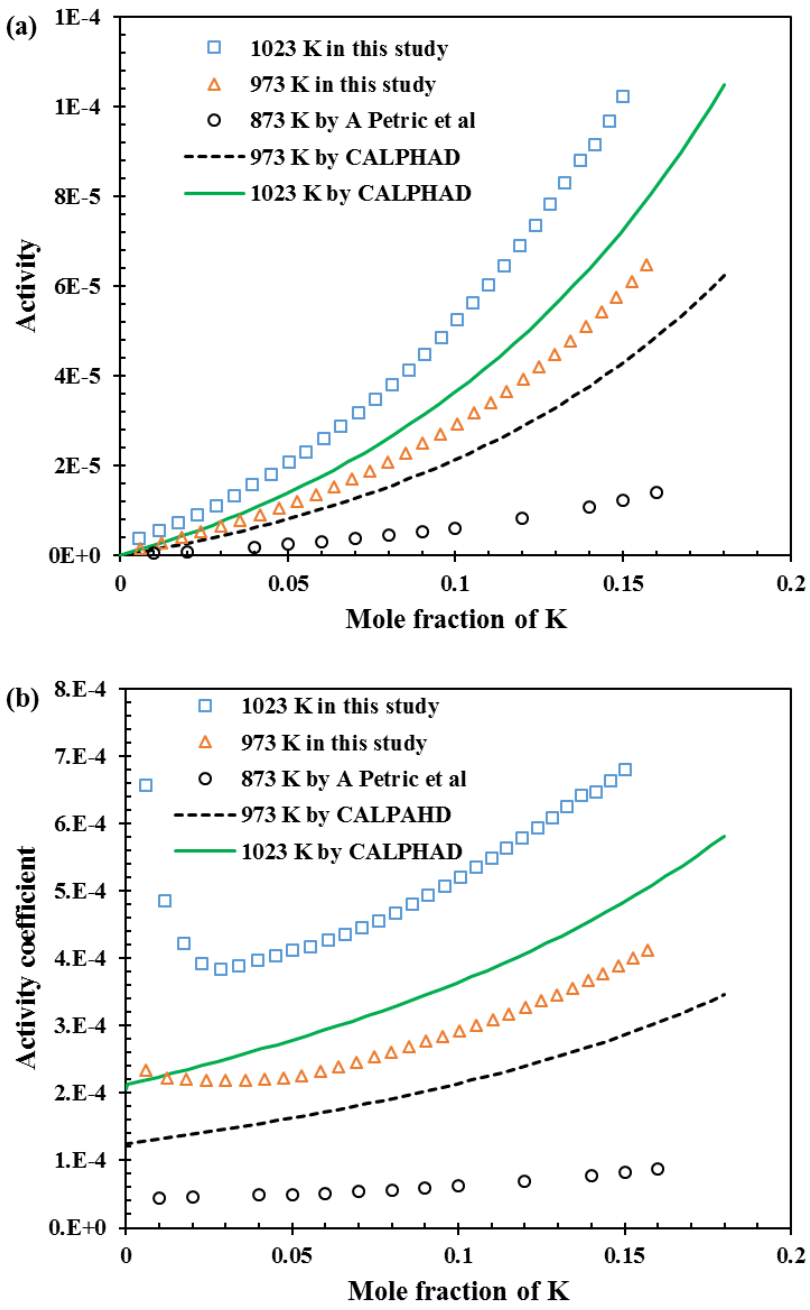

Figure 6-5. Activity and Activity coefficient of K in liquid Bi at different concentrations for the temperatures of 973 K and 1023 K.

6.3.2. The Bi-Li system

To study the activity of Li in liquid Bi, the same experiment procedure as done in Bi-K system was performed in the Bi-Li system. Considering the electrodeposition of Li cannot be achieved in molten FLiNaK salt because of the more cathodic equilibrium reduction potential of Li^+ than K^+ [99], LiF-LiCl molten salt with low evaporation was chosen to

provide the electrodeposition of Li. The test was carried out on a tungsten working electrode initially and the basic cell reaction was expressed as

Li-Bi (reference electrode) || LiF-LiCl electrolyte || W (working electrode).

Figure 6-6 shows the potential evolution of the tungsten working electrode against Li-Bi reference electrode over time in LiF-LiCl molten salt at the temperatures of 973 K and 1023 K. From the measured value of open circuit potential right after the termination of the application of the 5-s current pulse, the activity of Li in the reference electrode was calculated by equation $EMF = \frac{RT}{F}\ln(\alpha_{Li\ in\ RE})$ and listed in Table 6-2.

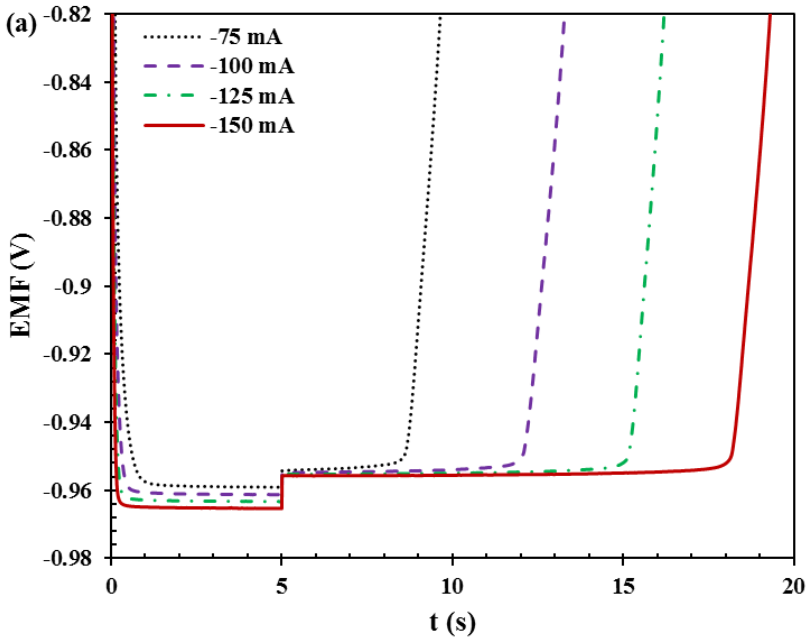

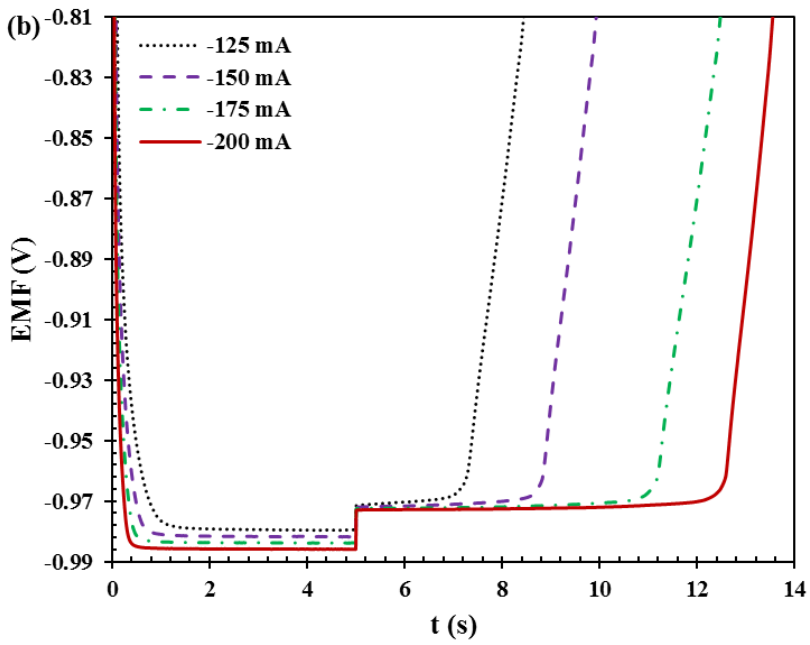

Figure 6-6. Potential evolution of the tungsten working electrode against Li-Bi reference electrode over time in LiF-LiCl molten salt when a 5-s pulse current was applied at (a) 973 K and (b) 1023 K.

Table 6-2. Activity and activity coefficient of Li in reference electrode at the temperatures of 973 K and 1023 K.

T (K)	EMF (V)	$\alpha_{Li\ in\ RE}$	$x_{Li\ in\ Bi}$	$\gamma_{Li\ in\ RE}$
973	-0.955	1.13×10^{-5}	0.1054	1.07×10^{-4}
1023	-0.972	1.62×10^{-5}	0.1054	1.54×10^{-4}

After the activity of Li in reference electrode was known, the working electrode was replaced with liquid Bi and the basic cell reaction then can be expressed as

Li-Bi (reference) || LiF-LiCl electrolyte || liquid Bi (working).

In Figure 6-7 (a), a constant current of -35 mA was applied on the liquid Bi electrode (1.263 g) for 100 s to titrate Li into it at 973 K. Followed by the titration, an open circuit potential measurement was performed for 2000 s to wait for the titrated Li to be uniformly mixed with the liquid Bi. The same process was repeated for 30 times to get the equilibrium electrode potentials at different Li-Bi ratios. Similarly, Figure 6-7 (b) shows the obtained coulometric titration EMF data at the temperature of 1023 K in which a constant current of -35 mA was applied on the liquid Bi electrode (1.241 g) to titrate Li for 100 s and a subsequent 3600 s open circuit potential measurement was conducted after each titration. Based on the measured open circuit potential followed by each titration, the equilibrium electrode potential referring to Li-Bi reference electrode was extracted and shown in Figure 6-8. Given that 3.63×10^{-5} mol Li was pre-deposited (-35 mA for 100 s) into liquid Bi

working electrode before the coulometric titration at 1023 K, the equilibrium electrode potential at 1023 K shown in Figure 6-8 starts from the mole fraction of 1.21 mol%. From the obtained equilibrium electrode potential at different concentrations and $\alpha_{Li\ in\ RE}$ listed in Table 6-2, the variations of activity and activity coefficient of Li in liquid Bi with concentration were acquired and indicated in Figure 6-9. These results are also compared with the ones reported in other literatures [155,156] from which it can be seen our results are reasonable and consistent with them if taking account of the temperature influence on the activity and activity coefficient.

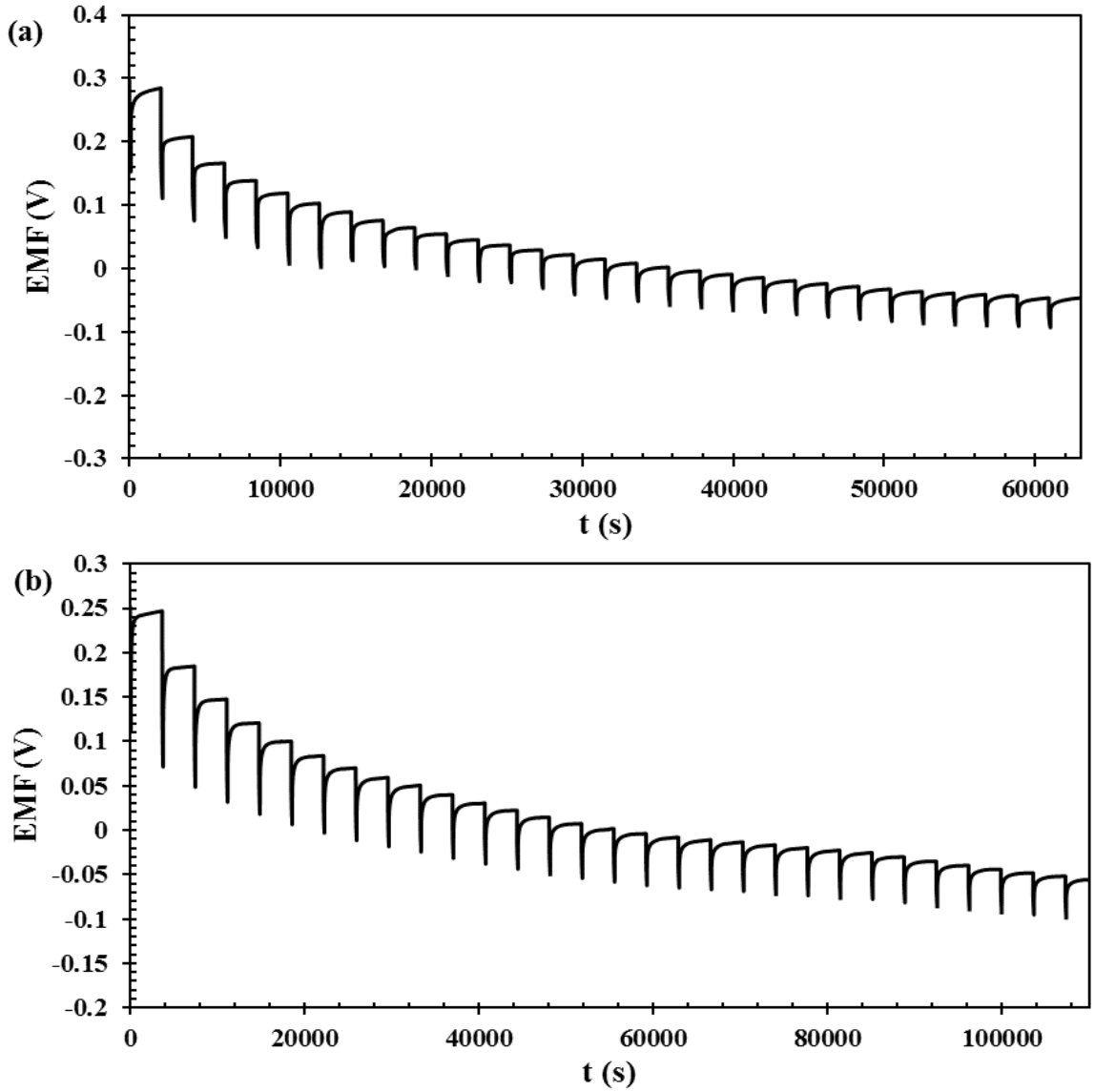

Figure 6-7. Coulometric titration of Li into liquid Bi working electrode in LiF-LiCl electrolyte at (a) 973 K and (b) 1023K.

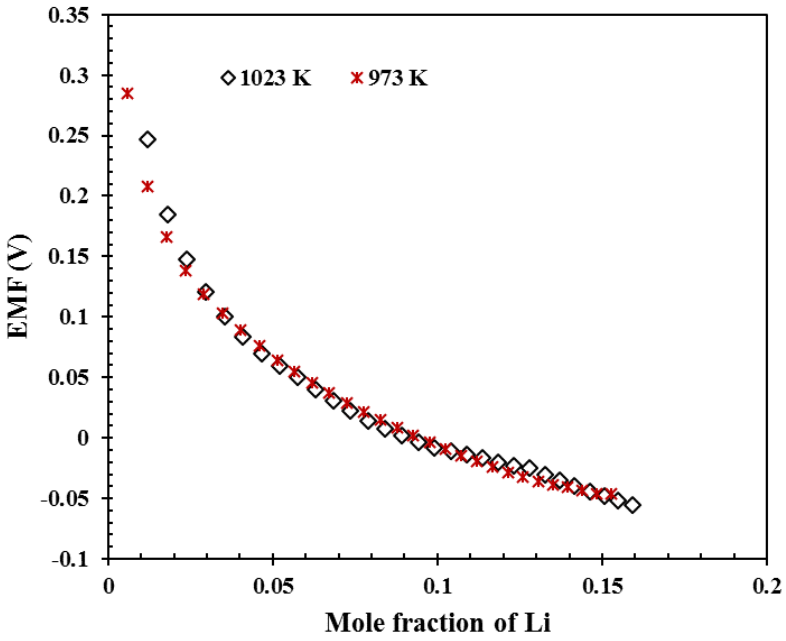

Figure 6-8. Equilibrium electrode potential as a function of Li mole fraction upon Li deposition at 973 K and 1023K.

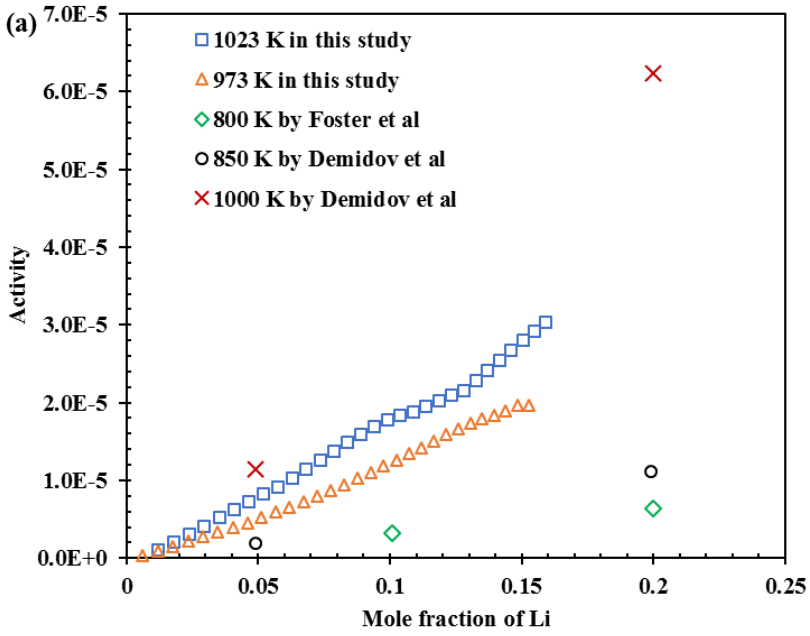

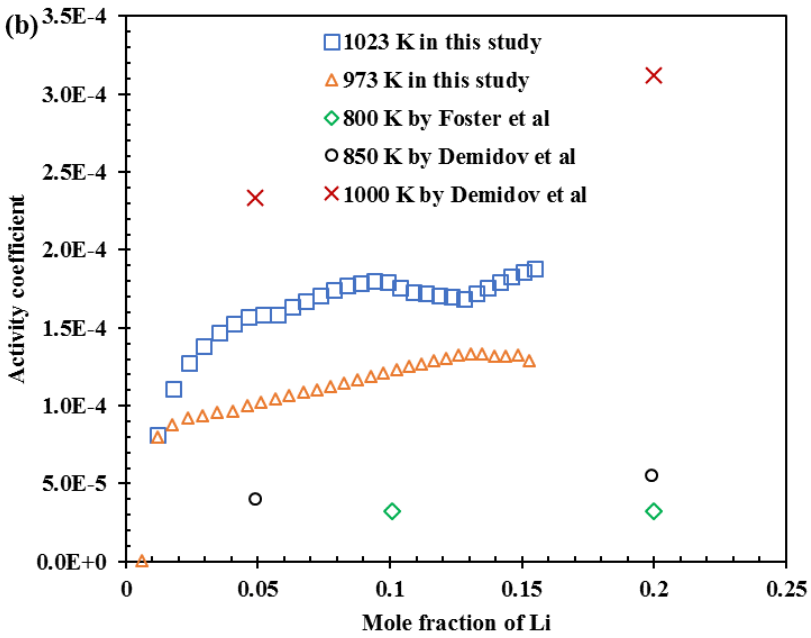

Figure 6-9. Activity and Activity coefficient of Li in liquid Bi at different concentrations for the temperatures of 973 K and 1023 K.

6.4. Conclusion

In this chapter, the activity and activity coefficient of K and Li in liquid bismuth at the temperatures of 973 K and 1023 K were obtained by the EMF measurement for different concentrations. Through coulometric titrating K and Li into liquid bismuth and performing EMF measurement after each titration, the variations of activity and activity coefficient of K and Li in liquid bismuth with concentration in the composition range lower than 20 mol% were obtained. It is found that the activity of both K and Li increases with concentration. For the activity coefficient, it is observed that the activity coefficient of K in liquid bismuth initially decreases and subsequently increases with concentration, while the activity coefficient of Li in liquid bismuth generally increases with concentration. In the present study, Bi-K (or Bi-Li) compositions were obtained by coulometric titrating different quantities of K (or Li) into liquid bismuth from molten salt, which makes it feasible to continuously measure the activity and activity coefficient for different K (or Li) concentrations and will be more accurate comparing with the EMF measurement on the different simply mixed Bi-K (Li) compositions.

7. Cyclic voltammetry modelling based on MOOSE

Cyclic voltammetry is one of the powerful tools to characterize the electrochemical reaction process and has a broad range of applications [160]. For instance, this technique is frequently used for analyzing electroactive species and determining their fundamental properties. Considering the great advantages of cyclic voltammetry, this technique has been widely used to study the electrochemical behaviors and fundamental properties of fission products and corrosion products in FLiNaK molten salt for the aim of FHR coolant clean-up [161,162]. The modelling and simulation of cyclic voltammetry are also good ways for studying the electrochemical processes in FHR coolant clean-up process. It can help enhance the fundamental understanding of the experimental cyclic voltammetry signals and provide the information which cannot be derived from the experiment. For example, the surface concentration variations of species in molten salt on the electrode and the concentration profiles of species along the diffusion layer can be modeled and it will contribute significantly to the investigation of the interface of electrode and electrolyte. In addition, some physical properties such as standard reaction rate and electron transfer coefficient which are not easily determined from experimental cyclic voltammetry signals can be obtained through the modelling.

In the present study, the models dealing with the single-step reversible electrochemical reaction, single-step quasi-reversible electrochemical reaction, single-step irreversible electrochemical reaction, multiple electrochemical reaction, and consecutive electrochemical reaction were developed based on MOOSE [163]. These models can be utilized to perform parametric studies to understand the effects of various parameters on the electrochemical reaction process. Through analyzing the key features of the simulated cyclic voltammetry curves, the fundamental understanding of the experiment results can be enhanced. At the same time, the developed models can be used to fit the experimental cyclic voltammetry curves by adjusting the parameters incorporated in the models to predict the fundamental properties. In addition to the application in FHR coolant clean-up, this study will also greatly contribute to the development in other applications in which the electrochemical processes are involved.

7.1. Single-step electrochemical reaction

7.1.1. Electrochemistry theory

Generally, a single-step electrochemical reaction with n electrons transferred can be expressed by

$$O + ne \rightleftharpoons R \tag{7-1}$$

where O is oxidant while R is reductant.

For a soluble-soluble reaction, the oxidant and reductant concentration profile, $C_o(x,t)$ and $C_R(x,t)$ in the diffusion layer can be expressed by

$$\frac{\partial C_o(x,t)}{\partial t} = D_o \frac{\partial^2 C_o(x,t)}{\partial x^2} \tag{7-2}$$

$$\frac{\partial C_R(x,t)}{\partial t} = D_R \frac{\partial^2 C_R(x,t)}{\partial x^2} \tag{7-3}$$

where D_o and D_R are the diffusion coefficients of *O* and *R* in electrolyte, respectively. If assuming oxidant *O* exists in the electrolyte at the beginning, the initial and boundary conditions constricting equation (7-2) can be expressed by:

$$C_o(x,0) = C_{o,bulk} \tag{7-4}$$

$$C_o(L,t) = C_{o,bulk} \tag{7-5}$$

where L is the thickness of diffusion layer. For reductant R, the initial and boundary conditions for diffusion equation (7-3) are listed by

$$C_R(x,0) = C_{R,bulk} \tag{7-6}$$

$$C_R(L,t) = C_{R,bulk} \tag{7-7}$$

$$D_R \left(\frac{\partial C_R(x,t)}{\partial x}\right)_{x=0} + D_o \left(\frac{\partial C_o(x,t)}{\partial x}\right)_{x=0} = 0 \tag{7-8}$$

To solve a diffusion equation, it is commonly required to have two boundary conditions and one initial condition. Therefore, to solve diffusion equation (7-2), one more boundary condition is needed. For the reversible electrochemical reaction, the charge-transfer kinetics on the electrode are very rapid, therefore, the potential on the electrode surface can be expressed by

$$E = E^f + \frac{RT}{nF} \ln \frac{C_o(0,t)}{C_R(0,t)} \tag{7-9}$$

where E^f is the formal potential, *R* is the gas constant, *T* is the temperature, *F* is the faraday constant. E is the scan potential which is time dependent in cyclic voltammetry and can be expressed by

$$E = E_i + vt \tag{7-10}$$

where E_i is the initial potential, v is the scan rate, t is the scan time. When the direction of the potential scan is switched, the scan potential becomes

$$E = E_s - vt \tag{7-11}$$

where E_s is the potential at the switching point. In reversible reaction, equation (7-9) will be another boundary condition in addition to equation (7-4) for governing diffusion equation (7-2).

For quasi-reversible reaction, the current is governed by both mass transfer and charge-transfer kinetics. Therefore, instead of the equation (7-9) used for reversible reaction, the following equation (7-12) will be one boundary condition for solving equation (7-2).

$$D_o\left(\frac{\partial C_o(x,t)}{\partial x}\right)_{x=0} = K^o\left(C_o(0,t)\,exp\left(\frac{-\alpha nF\left(E-E^f\right)}{RT}\right) - C_R(0,t)\,exp\left(\frac{(1-\alpha)nF\left(E-E^f\right)}{RT}\right)\right) \quad (7\text{-}12)$$

where K^o is the standard reaction rate, α is the electron transfer coefficient.

For the totally irreversible reaction, the backward component of the electrode reaction becomes progressively less important. Thus, the boundary condition in addition to the one shown in equation (7-5) for governing diffusion equation (7-2) can be written as

$$D_o\left(\frac{\partial C_o(x,t)}{\partial x}\right)_{x=0} = K^o C_o(0,t)\,exp\left(\frac{-\alpha nF(E-E^f)}{RT}\right) \quad (7\text{-}13)$$

Once the diffusion equations (7-2) and (7-3) are solved, the current density can be obtained by

$$i = -nFD_o\left(\frac{\partial C_o(x,t)}{\partial x}\right)_{x=0} \quad (7\text{-}14)$$

7.1.2. Implementation of MOOSE

The partial differential equation to be solved in MOOSE needs to be written in weak form. The weak forms of equations (7-2) and (7-3) are written as follows:

$$\left(\frac{\partial C_o(x,t)}{\partial t},\psi_j\right) + \left(D_o\nabla C_o(x,t),\nabla\psi_j\right) - \langle D_O\nabla C_o(x,t)\cdot\hat{n},\psi_j\rangle = 0 \quad (7\text{-}15)$$

$$\left(\frac{\partial C_R(x,t)}{\partial t},\psi_j\right) + \left(D_R\nabla C_R(x,t),\nabla\psi_j\right) - \langle D_R\nabla C_R(x,t)\cdot\hat{n},\psi_j\rangle = 0 \quad (7\text{-}16)$$

where ψ_j is the test function, $\hat{n}$ is the normal vector. $\left(\frac{\partial C_o(x,t)}{\partial t},\psi_j\right)$ and $\left(\frac{\partial C_R(x,t)}{\partial t},\psi_j\right)$ are time derivative kernels while $\left(D_o\nabla C_o(x,t),\nabla\psi_j\right)$ and $\left(D_R\nabla C_R(x,t),\nabla\psi_j\right)$ are diffusion kernels. Both time derivative kernel and diffusion kernel have been developed in MOOSE itself, thus, it can be used directly. $\langle D_O\nabla C_o(0,t)\cdot\hat{n},\psi_j\rangle$ and $\langle D_R\nabla C_R(0,t)\cdot\hat{n},\psi_j\rangle$ are boundary condition kernels. The boundary conditions shown in equations (7-5) and (7-7) are two Dirichlet boundary conditions and were specified using the DirichletBC object provided by MOOSE. For the boundary condition as shown in equation (7-8), it was inherited from IntegratedBC in MOOSE and written in the weak form of $\langle D_O\nabla C_o(0,t)\cdot$

$\hat{n}, \psi_j\rangle$. The boundary condition as shown in equation (7-9) was inherited from NodalBC in MOOSE and written in the weak form of $\frac{C_o(0,t)}{C_R(0,t)} - \exp\left(\frac{nF}{RT}(E - E^f)\right)$. The boundary conditions (7-12) and (7-13) were also inherited from IntegratedBC in MOOSE as done for boundary condition (7-8). Once the kernels and boundary conditions have been defined well in MOOSE, a steady executioner which uses default solving method Preconditioned Jacobian Free Newton Krylov was chosen to carry out the calculation.

7.1.3. Results and discussions

7.1.3.1.Reversible reaction

Cyclic voltammetry curve for soluble-soluble reversible reaction was simulated based on the calculated concentration profile of oxidant in the diffusion layer from MOOSE. Figure 7-1 shows the simulated cyclic voltammetry curve using MOOSE in the potential range of 1.4 V to 0.5 V based on the assumed material properties listed in Table 7-1.

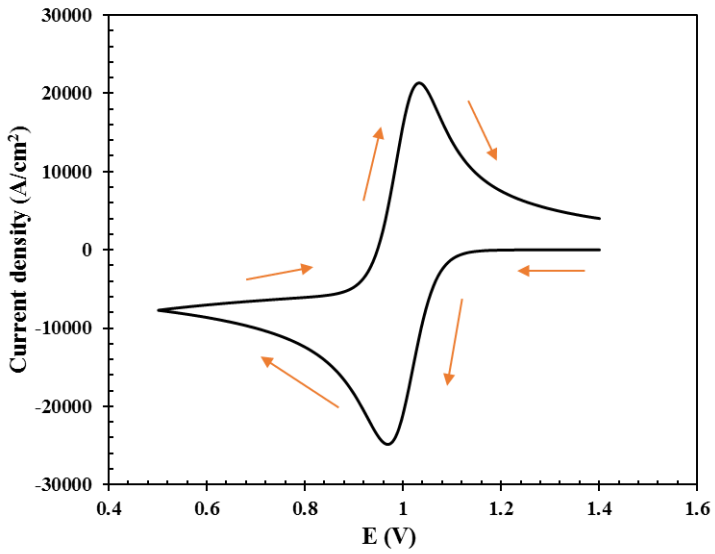

Figure 7-1. Typical simulated cyclic voltammogram for single-step electrochemical reaction based on MOOSE.

Table 7-1. Assumed material properties for the simulated cyclic voltammetry curve in Figure 7-1.

T (K)	D_o (cm^2/s)	D_R (cm^2/s)	v (V/s)	E^f (V)	n	$C_{o,bulk}$(mol/cm^3)	$C_{R,bulk}$(mol/cm^3)
300	0.01	0.01	1	1	1	1	0

In the reversible electrochemical reaction, the analytical solution for the peak current density of cyclic voltammogram has been derived based on the boundary and initial conditions of reversible reaction discussed in the section 7.1.1, which is given by

$$i_{\mathrm{p}} = 0.4463nFAC_{\mathrm{b}}D^{1/2}\left(\frac{nFv}{RT}\right)^{1/2} \tag{7-17}$$

where i_{p} is the peak current density, D is the diffusion coefficient, C_{b} is bulk concentration, n is the number of exchanged electrons of the reaction, and v is the scan rate. It can be seen there is a linear relationship between the peak current density i_{p} and $v^{1/2}$. In order to confirm the accuracy of the developed reversible electrochemical reaction model by MOOSE, the peak current density from the simulated cyclic voltammogram at different scan rates were acquired and shown in Figure 7-2, from which a linear relationship between i_{p} and $v^{1/2}$ can be observed. It is consistent with the analytical solution (7-17) and validates the model developed here by MOOSE.

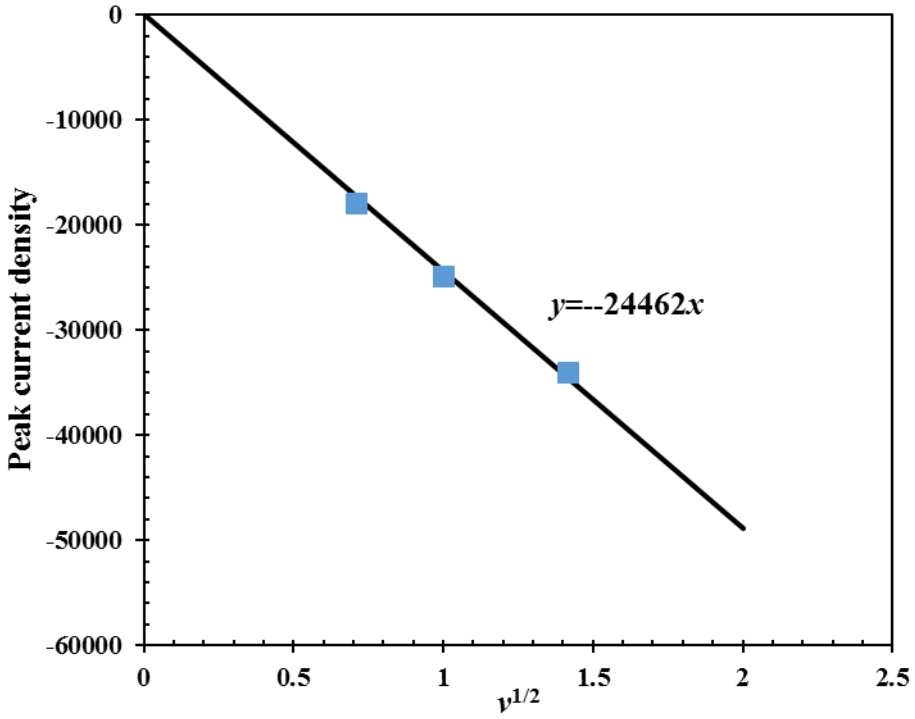

Figure 7-2. Linear relationship of peak current density versus $v^{1/2}$ for simulated CV curves.

In addition to capturing cyclic voltammetry curve, the model developed based on MOOSE can also be used to study some microscopic information which cannot be obtained through the experiment, for example, the surface concentration variations of oxidants and reductants on the electrode. Figure 7-3 shows the variations of the surface concentrations of oxidant C_sO and reductant C_sR with time during the cyclic voltammetry scan shown in Figure 7-1. From Figure 7-3, the information about the materials transport from/to the electrode surface was provided. During the time range of 0 to 0.9 s which corresponds to the cyclic voltammetry scan from 1.4 to 0.5 V, the surface concentrations C_sO and C_sR stay unchanged at the beginning, then, C_sO decreases rapidly while C_sR increases, after that, the variations of C_sO and C_sR keep stable again. When the cyclic voltammetry is scanned back from 0.5 to 1.4 V in the time range of 0.9 to 1.8 s, C_sO and C_sR keep stable

initially, then C_sO increases back rapidly while C_sR decreases, eventually both of them remain unchanged. The change of concentration in the cyclic voltammetry scan is due to the redox reaction occurring.

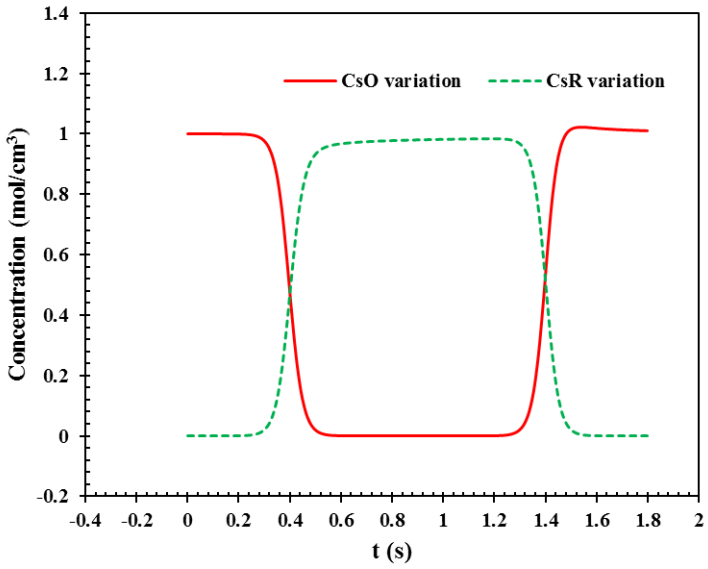

Figure 7-3. The variations of surface concentrations of oxidant C_sO and reductant C_sR with time during the cyclic voltammetry scan shown in Figure 7-1.

The understanding of the effect of scan rate on cyclic voltammetry curves is significant for analyzing qualitative features in the experimentally recorded signals. Therefore, the effect of the scan rate on the simulated cyclic voltammograms was investigated. Figure 7-4 shows the cyclic voltammograms at different scan rates while other material properties are the same as the ones listed in Table 7-1. It is shown that the peak current density in cyclic voltammetry increases with the increasing scan rate. At the same time, the peak potential is also observed to be invariable at different scan rates for reversible electrochemical reaction. This finding can be used to identify the reversibility of one electrochemical reaction.

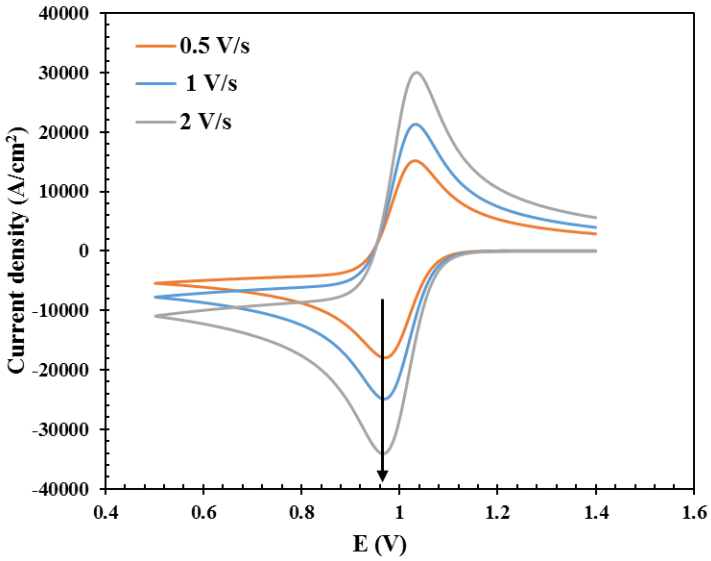

Figure 7-4. Simulated cyclic voltammetry curves at different scan rates.

Temperature is another factor which will affect cyclic voltammetry curve significantly. Considering material properties such as diffusion coefficient will change with temperature, the influence of temperature on cyclic voltammogram in the real experiment study in fact arises from the combination of temperature and material properties. To study the sole effect of temperature on cyclic voltammogram, the simulated cyclic voltammograms by changing the values of temperatures while keeping other material properties the same as the ones as listed in Table 7-1 are carried out and shown in Figure 7-5. Normally, peak current density increases with the increasing temperature. However, the simulated cyclic voltammetry curves in Figure 7-5 in this study indicate that the peak current density at higher temperature has a lower value. The reason for this is that the diffusion coefficients at different temperatures are set to be the same during the simulation. In the real situation, the diffusion coefficient will increase at a higher temperature. The broadening of the cathodic/anodic peaks is also observed at higher temperature from Figure 7-5 and it is attributed to that a higher temperature allows the electron transfer process to occur over a wider potential window since higher temperature supplies more energy to facilitate the surmounting of energy barriers in the electron transfer process [160].

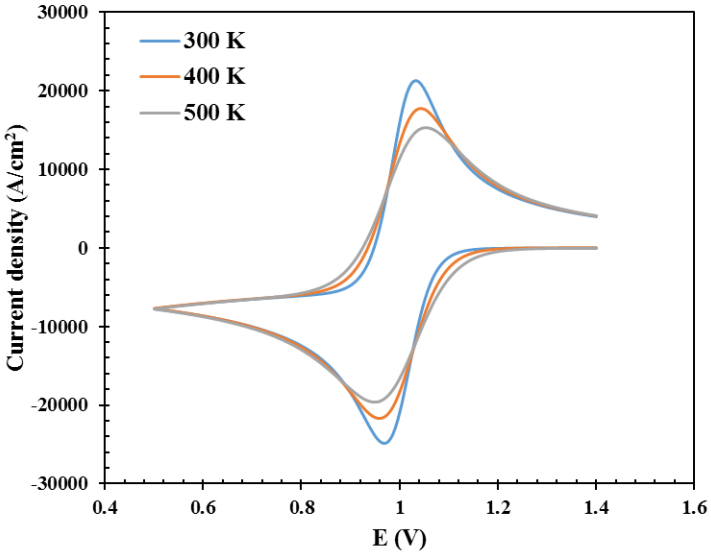

Figure 7-5. Simulated cyclic voltammetry curves at different temperatures.

The effect on cyclic voltammetry curve brought by diffusion coefficient is also carried out in this study. Figure 7-6 shows the cyclic voltammetry curves when different values were set for the diffusion coefficient D_o while other material properties are the same as the ones listed in Table 7-1. It can be shown the peak current increases with the increasing diffusion coefficient of the oxidant.

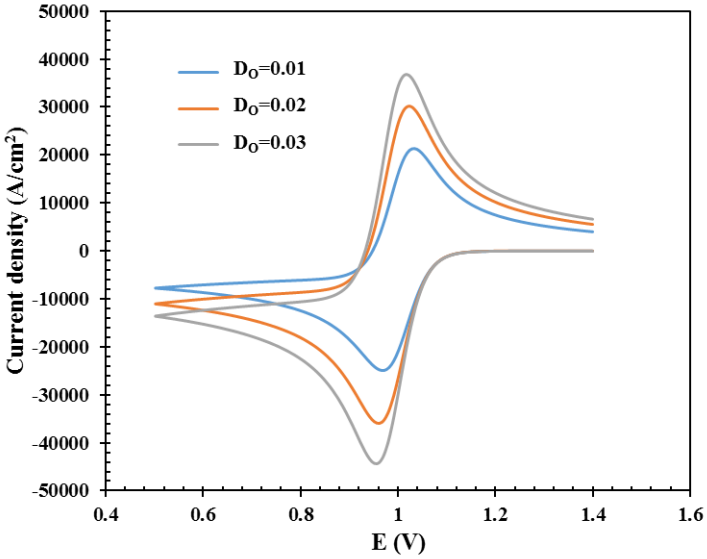

Figure 7-6. Simulated cyclic voltammetry curves at different diffusion coefficients.

The electrochemical reaction process in which only one member (either oxidant or reductant) of a redox couple is present in the electrolyte is widely studied before. However, the investigation on the system containing both members of the redox couple, for example, the presence of both U^{4+} and U^{3+} [164] or presence of both Cr^{3+} and Cr^{2+} [165] in molten salts, is very limited. To study the effect of the presence of both oxidant and reductant on

cyclic voltammogram, the simulations of cyclic voltammetry when setting the bulk concentrations of reductant C_bR and oxidant C_bO by C_bR =0 mol/cm^3; C_bO =1 mol/cm^3, C_bR =1 mol/cm^3; C_bO=1 mol/cm^3, and C_bR =0 mol/cm^3; C_bO =2 mol/cm^3 without changing other material properties (Table 7-1) were performed respectively. Figure 7-7 shows the simulated cyclic voltammetry results. Different from the cyclic voltammetry results obtained when only oxidant presents, the current density drops from an extremely high value at the start point of cyclic voltammetry scan when both oxidant and reductant exist in the system. Comparing with results obtained at the condition of C_bR =0 mol/cm^3; C_bO =1 mol/cm^3, the peak current densities of the obtained cyclic voltammograms for the conditions of C_bR =1 mol/cm^3; C_bO =1 mol/cm^3 and C_bR =0 mol/cm^3; C_bO =2 mol/cm^3 increase a lot. There is slightly different for the cyclic voltammograms achieved at the conditions of C_bR =1 mol/cm^3; C_bO =1 mol/cm^3 and C_bR =0 mol/cm^3; C_bO =2 mol/cm^3. In detailed, the cathodic peak current density is lower while the anodic one is higher for the condition of C_bR =1 mol/cm^3; C_bO =1 mol/cm^3.

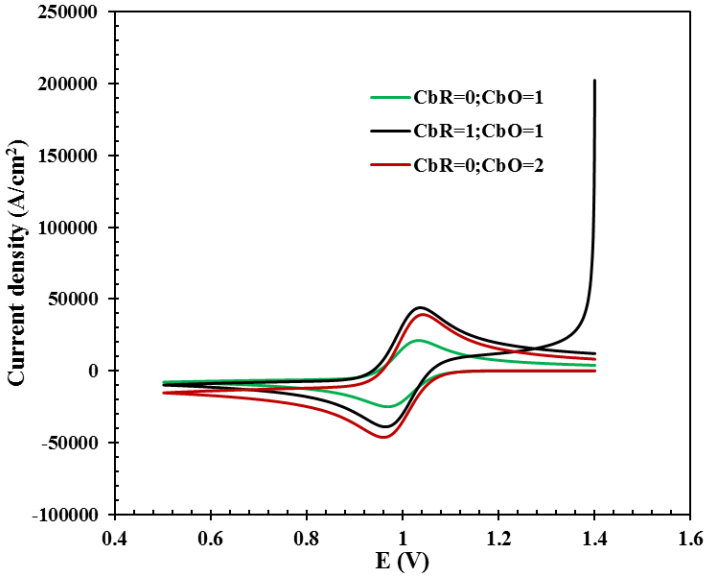

Figure 7-7. Simulated cyclic voltammetry curves for different bulk concentration conditions of oxidant and reductant.

It is also interesting to know the variations of the surface concentration profiles of oxidant and reductant during the cyclic voltammetry scan when both of them exist in the system. Figure 7-8 shows the surface concentration variations for oxidant and reductant at different conditions. It can be observed that C_sR drops sharply from 1 mol/cm^3 to 0 at the start point of cyclic voltammetry scan when both reductant and oxidant exist in the system. For oxidant, although its bulk concentration C_bO is only 1 mol/cm^3, the surface concentration of C_sO drops sharply from an extremely high value to ~2 mol/cm^3 rapidly when cyclic voltammetry scan begins and then stays at a value of about 2 mol/cm^3 until the redox reaction occurs. The reason for this is that almost all the reductant has been converted to oxidant at the start point.

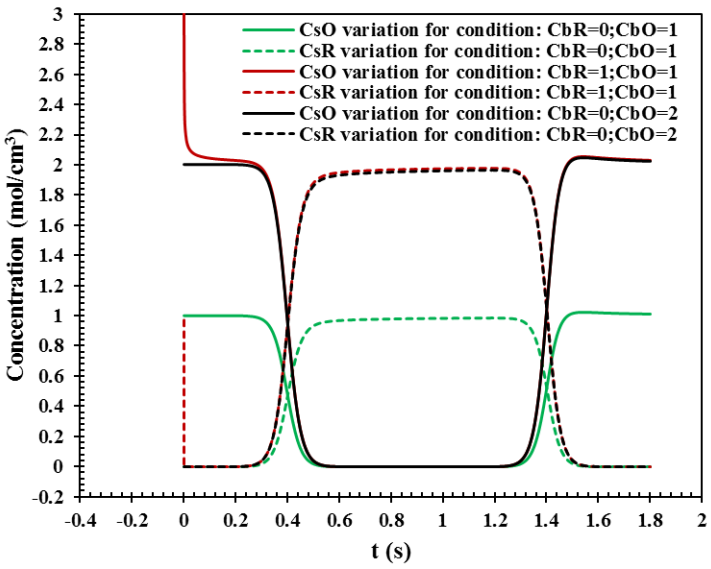

Figure 7-8. The variations of surface concentrations during cyclic voltammetry scan for different bulk concentration conditions of oxidant and reductant.

Multiple reactions in the electrochemical process is another interesting topic. To study the cyclic voltammetry curve overlapped by multiple reactions, three different electrochemical reactions with the formal potential of 0.85 V, 1.00 V, and 1.15 V while other material properties are the same as the ones listed in Table 7-1 are simulated in MOOSE. Figure 7-9 shows the simulated cyclic voltammetry curve for multiple electrochemical reaction processes. The peak current densities are supposed to be the same when all the material properties are set to be the same values. However, the obvious difference on the peak current densities is observed in Figure 7-9 for the three electrochemical reactions. It means the peak current densities for these three different electrochemical reactions are affected by each other. Therefore, in a multiple-electrochemical reaction system, the peak current density cannot be used directly for electroanalysis. Instead, the residual current density resulting from other electrochemical reaction processes should be subtracted out first to obtain an accurate peak current density for the target electrochemical reaction.

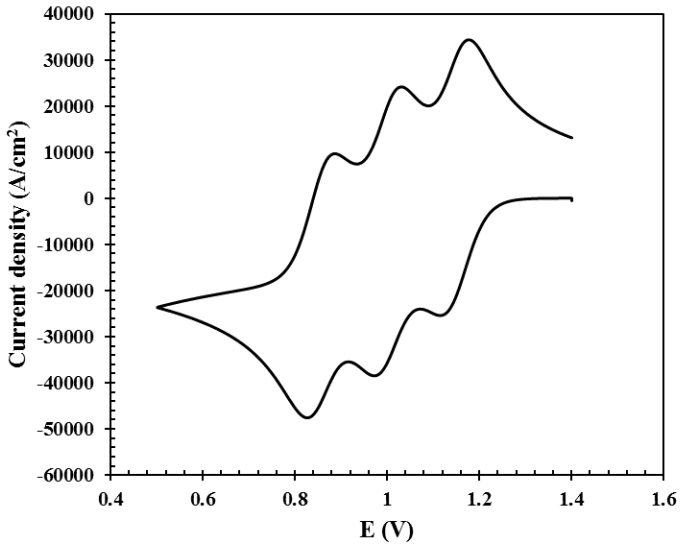

Figure 7-9. Simulated cyclic voltammetry curve for multiple-electrochemical reaction process.

7.1.3.2.Quasi-reversible reaction

In addition to the parameters listed in Table 7-1, two more parameters, standard reaction rate K^o and electron transfer coefficient α, are induced in the quasi-reversible electrochemical reaction. The kinetics of the electron transfer process in one electrochemical reaction can be understood through the study of standard reaction rate K^o. Figure 7-10 shows the simulated cyclic voltammograms for several values of standard reaction rate while other material properties are kept the same as the ones listed in Table 7-1. It is found that the peak current density decreases when K^o decreases. At the same time, a notable increase in the peak-to-peak separation was also observed with the increase of K^o. The larger the value of K^o the faster the electron transfer process. Species diffusion will take control in the electrochemical reaction which has a fast electron transfer process and this reaction will be reversible. From the shapes of curves shown in Figure 7-10, it can be clearly seen that the electrochemical process is more reversible when K^o increases.

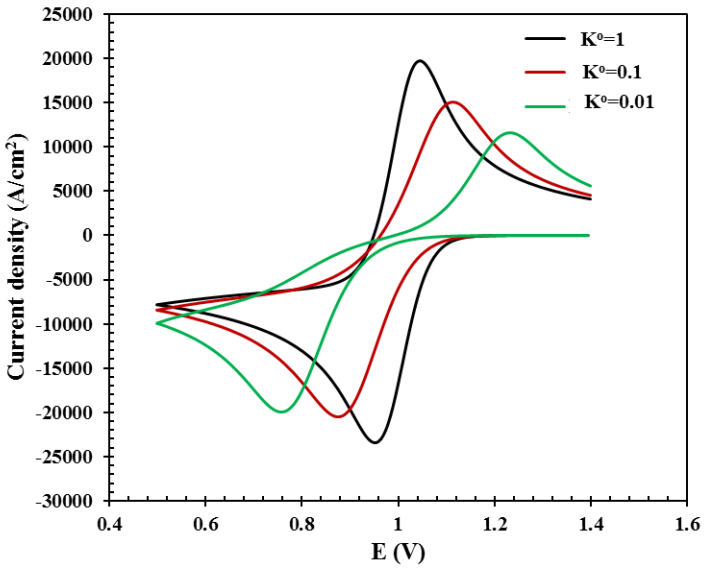

Figure 7-10. Simulated cyclic voltammetry curves at different standard reaction rates.

The symmetry in the energy barrier for the electron transfer process is described by the charge transfer coefficient α. Figure 7-11 shows the effect of the charge transfer coefficient on the simulated cyclic voltammetry curves. Three cases are examined in this study: α=0.5, α=0.3, and α=0.7. The case with α=0.3 is a reactant-like transition state and favors the formation of the oxidized species. Therefore, the cyclic voltammetry curve for α=0.3 shown in Figure 7-11 displays a more intense anodic peak with a less intense cathodic peak. The case with α=0.7 is a product-like transition state in which a more intense cathodic peak with a less intense anodic peak was observed.

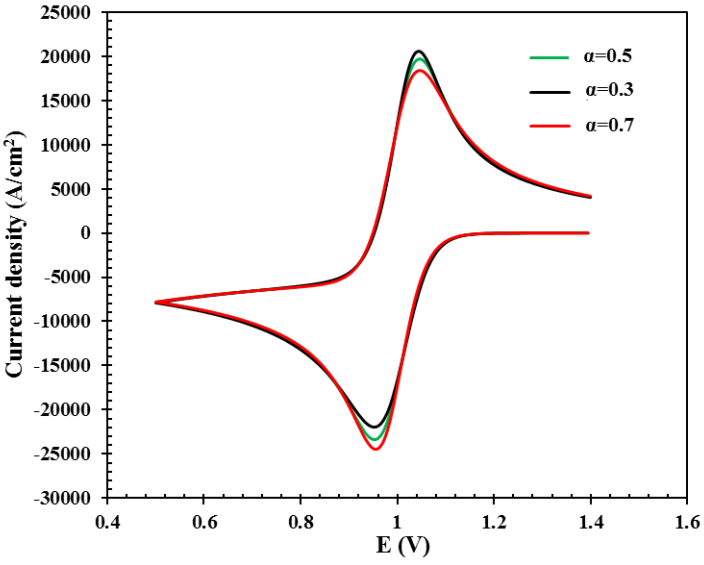

Figure 7-11. The effect of the charge transfer coefficient on the simulated cyclic voltammetry curves.

7.1.3.3.Irreversible reaction

Electron transfer reactions are sluggish when there is a high barrier to electron transfer and then the electrochemical reaction will be irreversible. Figure 7-12 shows the typical simulated cyclic voltammograms for irreversible reaction in which the oxidation electron transfer process is sluggish. Only cathodic peaks were observed in the whole cyclic voltammetry scan from Figure 7-12. This simulated result is the same as the experimental one reported in the previous study for the irreversible reaction [166]. Through keeping other material properties the same as the ones listed in Table 7-1 while changing the value of standard reaction rate, the effect of standard reaction rate on the irreversible cyclic voltammogram was studied and indicated in Figure 7-12 from which a current peak potential shift with the increasing standard reaction rate can be seen. No peak current density variation was observed with the change of standard reaction rate.

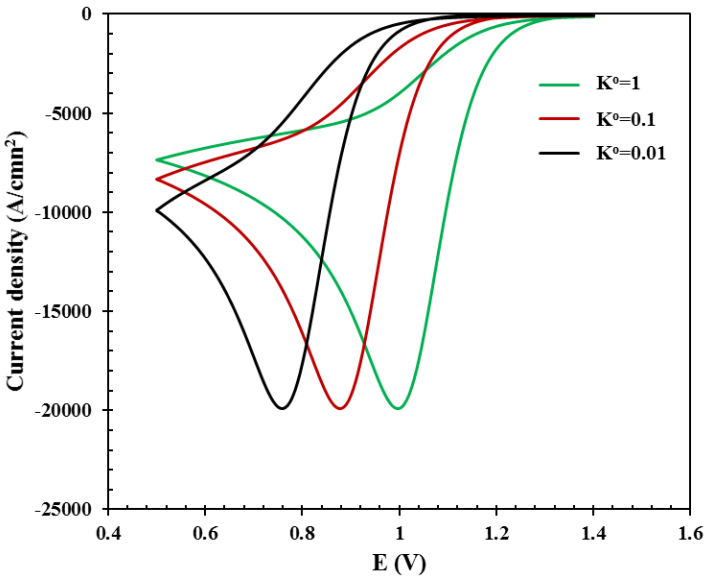

Figure 7-12. The simulated cyclic voltammetry curves at different standard reaction rates for irreversible reaction.

7.2. Consecutive charge transfer reactions

7.2.1. Electrochemistry theory

The details about the electrochemistry theory for consecutive charge transfer reactions are described by Zhang et al [167]. The consecutive charge transfer reactions with n_1 electrons transferred at the first charge transfer process while n_2 electrons transferred at the second charge transfer process can be expressed by equations (7-18) and (7-19) respectively

$$A + n_1 e \leftrightarrow B \tag{7-18}$$

$$B + n_2 e \leftrightarrow C \tag{7-19}$$

If the reactant A, intermediate product B, and final product C obey Fick's law, then the diffusion equations governing equations (7-18) and (7-19) can be expressed by

$$\frac{\partial C_A(x,t)}{\partial t} = D_A\left(\frac{\partial^2 C_A(x,t)}{\partial x^2}\right) \tag{7-20}$$

$$\frac{\partial C_B(x,t)}{\partial t} = D_B\left(\frac{\partial^2 C_B(x,t)}{\partial x^2}\right) \tag{7-21}$$

The current densities due to the reactions at the electrode for the two consecutive charge transfer processes can be expressed by Butler-Volmer equation:

$$i_1 = -n_1 F K_1^o\left(C_A(0,t)\, exp\left(\frac{-\alpha_1 n_1 F(E-E^{f1})}{RT}\right) - C_B(0,t)\, exp\left(\frac{(1-\alpha_1) n_1 F(E-E^{f1})}{RT}\right)\right) \tag{7-22}$$

$$i_2 = -n_2 F K_2^o\left(C_B(0,t)\, exp\left(\frac{-\alpha_2 n_2 F(E-E^{f2})}{RT}\right) - C_C(0,t)\, exp\left(\frac{(1-\alpha_2) n_2 F(E-E^{f2})}{RT}\right)\right) \tag{7-23}$$

If a metal deposition is involved in the consecutive charge transfer reactions, the surface concentration of the deposited metal C, for example, will be expressed by $C_C(0,t)\sigma$. σ in cm^{-1} is introduced to serve as the unit converter to keep the unit of $C_C(0,t)\sigma$ the same as that of $C_B(0,t)$ since the unit of the surface concentration of the deposited metal on the electrode is mol/cm^2 while that for B in electrolyte is mol/cm^3.

Both reaction kinetics and mass transfer of the electrochemical reactions at the electrode surface should be considered. They can be coupled together for modelling the boundary conditions for equations (7-20) and (7-21). For reactant A, the surface concentration change can be calculated by

$$\delta_1 \frac{\partial C_A(0,t)}{\partial t} = -D_A\left(\frac{\partial C_A(x,t)}{\partial x}\right)_{x=0} + \frac{i_1}{n_1 F} \tag{7-24}$$

while for intermediate product B, the surface concentration change can be expressed by

$$\delta_2 \frac{\partial C_B(0,t)}{\partial t} = -D_B\left(\frac{\partial C_B(x,t)}{\partial x}\right)_{x=0} - \frac{i_1}{n_1 F} + \frac{i_2}{n_2 F} \tag{7-25}$$

where δ_1 and δ_2 are the thickness of the surface layer. The surface concentration change of product B can be expressed by

$$\frac{\partial C_C(0,t)}{\partial t} = -\frac{i_2}{n_2 F} \tag{7-26}$$

In addition to the boundary conditions (7-24) and (7-25), the bulk concentrations of A and B will work as another boundary conditions and initial conditions for solving equations (7-20) and (7-21). Once the governing equations (7-20) and (7-21) get solved, the current density i_1 and i_2 can be obtained based on the calculated surface concentration profiles.

7.2.2. Implementation of MOOSE

As performed in single-step electrochemical reactions, the governing equations (7-20) and (7-21) are solved by time derivative kernel and diffusion kernel which have been developed in MOOSE. The boundary conditions in (7-24) and (7-25) are incorporated in MOOSE through inheriting IntegratedBC. In the Inherited IntegratedBC, u_dot was used for the time derivative variable, for example, $\frac{\partial C_A(0,t)}{\partial t}$. A NodalKernel was added to achieve the calculation of equation (7-26). In the calculation process, a steady executioner which uses default solving method Preconditioned Jacobian Free Newton Krylov was chosen.

7.2.3. Results and discussions

Figure 7-13 shows the simulated cyclic voltammetry curves for consecutive charge transfer electrochemical reactions based on the assumed material properties listed in Table 7-2. In Figure 7-13, the redox peaks at the left correspond to the first charge transfer process with 1 electron transferred while the redox peaks at the right correspond to the second charge transfer process with 2 electrons transferred. The shape shown in Figure 7-13 indicates the present model can capture the main features of the cyclic voltammogram for consecutive charge transfer electrochemical reactions.

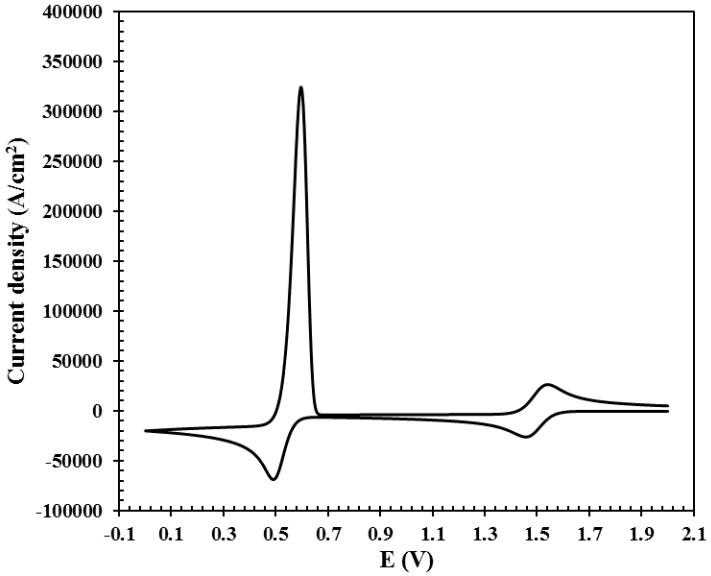

Figure 7-13. Typical simulated cyclic voltammogram for consecutive charge transfer reactions based on MOOSE.

Table 7-2. Assumed material properties for the simulated cyclic voltammetry curve in Figure 7-13.

T (K)	D_A (cm^2/s)	D_B (cm^2/s)	v (V/s)	E^{f1} (V)	E^{f2} (V)	n_1	n_2	$C_{A,bulk}$ (mol/cm^3)	$C_{B,bulk}$ (mol/cm^3)	$C_{C,bulk}$ (mol/cm^3)	δ_1	δ_2
300	0.01	0.01	1	1.5	0.5	1	2	1	0	0	0.001	0.001

The surface concentration profiles of reactant A, intermediate product B, and final product C during the cyclic voltammetry scan are provided in Figure 7-14 from which the materials transport from/to the electrode surface can be known. During the cyclic voltammetry forward scan (0 to 2 s), the surface concentration of A starts to decrease while that of B starts to decrease after some operation time. The change of the surface concentration occurs during this period because of the reaction $A + n_1 e \leftrightarrow B$. The surface concentration of B decreases back to 0 and then the surface concentration of C starts to increase at around 1.5 s, it is attributed to the reaction $B + n_2 e \leftrightarrow C$. In the cyclic voltammetry backward scan (2 to 4 s), the surface concentration of C keeps increasing until around 2.5 s where the surface concentration of B starts to increase sharply while that of C starts to decrease which is due to the reaction of $C \leftrightarrow B + n_2 e$. When the backward scan moves further, the surface concentration of B decreases while that of C increases since the reaction of $B \leftrightarrow A + n_1 e$ occurs.

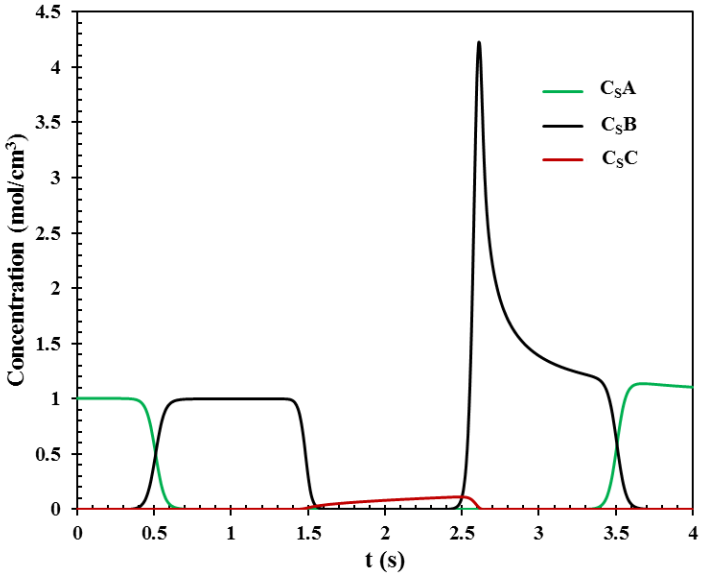

Figure 7-14. The variations of surface concentrations of reactant A, intermediate product B, and final product C with time during the cyclic voltammetry scan shown in Figure 7-13.

The effects of the parameters such as temperature and scan rate on the cyclic voltammetry curve of consecutive charge transfer reaction have been discussed in the previous study [167]. However, the investigation on the system when both reactant A and intermediate product B present was not performed. The understanding of the change of cyclic voltammogram for consecutive charge transfer reaction at different initial conditions is significant in the electrochemical study. By keeping the material properties the same as the

ones listed in Table 7-2, the simulations of cyclic voltammetry when setting the bulk concentrations of reductant C_bA and intermediate product C_bB by C_bA =1 mol/cm^3; C_bB =0 mol/cm^3, C_bA =1 mol/cm^3; C_bB=1 mol/cm^3, and C_bA =2 mol/cm^3; C_bB =0 mol/cm^3 were carried out. Figure 7-15 shows the simulated cyclic voltammograms from which it can be seen that the redox peaks for the condition of C_bA =1 mol/cm^3; C_bB =0 mol/cm^3 are much smaller. When both reactant A and intermediate product B exist in the electrolyte, the current density drops rapidly from an extremely high value when the cyclic voltammetry scan starts. This result is similar to one obtained in Figure 7-7. The redox peaks for the conditions of C_bA =1 mol/cm^3; C_bB=1 mol/cm^3 and C_bA =2 mol/cm^3; C_bB =0 mol/cm^3 are almost the same except for a small difference on the cathodic peak in the first charge transfer process.

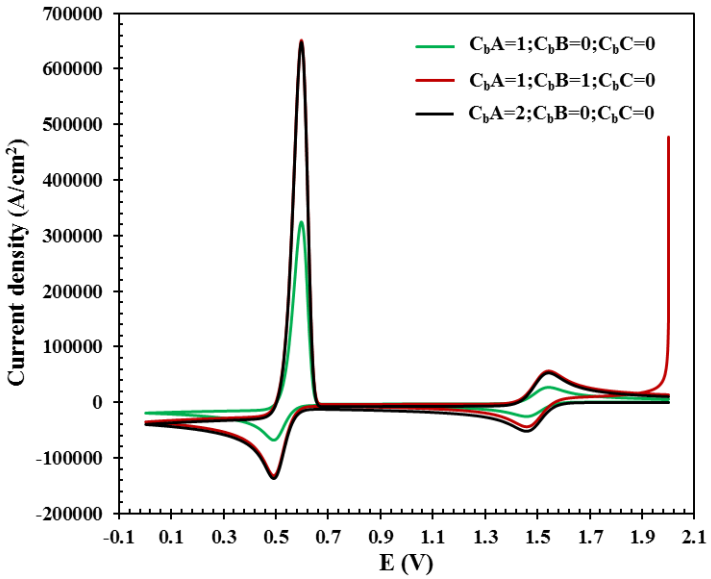

Figure 7-15. Simulated cyclic voltammetry curves for different bulk concentration conditions of reactant A and intermediate product B.

The effect of surface layer thickness δ on cyclic voltammogram is also studied, Figure 7-16 shows the simulated cyclic voltammograms at different surface layer thicknesses. The figure shows the cyclic voltammogram will not change when the surface layer thickness is less than 0.001 cm.

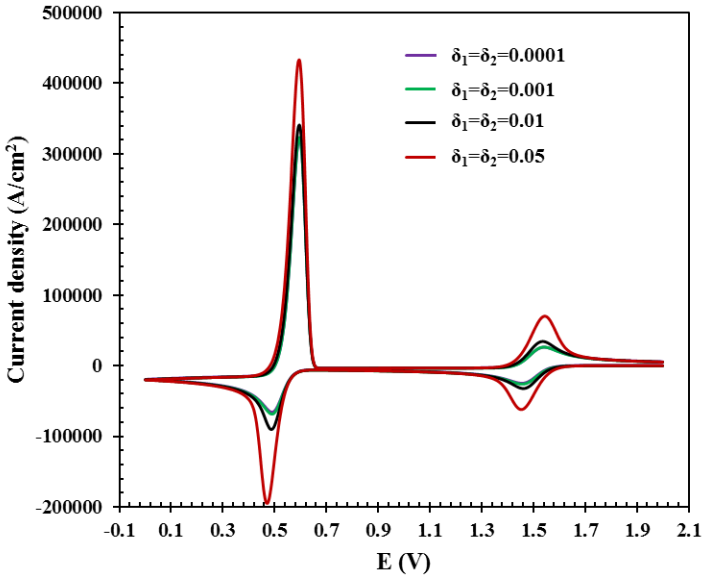

Figure 7-16. Simulated cyclic voltammetry curves when different surface layer thicknesses were set.

7.3. Conclusion

In the present chapter, the single-step reversible, quasi-reversible, irreversible electrochemical reactions and consecutive charge transfer electrochemical reactions were modelled by MOOSE. These models take into account diffusivity, temperature, scan rate, standard reaction rate, and charge transfer coefficient. This study will help enhance the fundamental understanding of the key features in the experimentally recorded cyclic voltammograms. Through fitting the experimentally recorded cyclic voltammograms, this study also has the potential use to get the unknown material properties or measure in-situ the species' concentrations.

8. Summary

In the present study, a series of investigations were carried out for the purpose of molten salt coolant clean-up in FHR. Through the studies on the electrochemical behaviors of LaF_3 in FLiNaK molten salt, it is observed the electrochemical separation of lanthanum from FLiNaK molten salt can be achieved by merely using an inert working electrode although the standard reduction potential of La^{3+} is more negative than that of the main salt constituents. To figure out the reason for this phenomenon, further studies were performed. It is found lanthanum species exist in the form of LaF_6^{3-} instead of La^{3+} in FLiNaK molten salt and it is the formation of LaF_6^{3-} proceeds the electrodeposition of lanthanum. Complex ion LaF_6^{3-} is the present species for LaF_3 in molten fluoride salts where KF or NaF is added. This finding would provide a new method on the electrochemical separation of lanthanum in molten fluoride salts: electrodepositing lanthanum with the aid of KF or NaF. This method will help get pure lanthanum metal in a simpler way and it is anticipated to be applied to extract other actinide metals such as critical materials (rare earth metals) from molten fluoride salts or other kinds of molten salt systems. Electrochemical studies of CeF_3 in FLiNaK molten salt were carried out using both inert and reactive electrodes. Similar phenomenon as observed in FLiNaK-LaF_3 molten salt system was also found in FLiNaK-CeF_3 when using inert electrode. The electrochemical separation of Ce from FLiNaK molten salt can be achieved by inert electrode. Reactive electrodes including Cu and Ni were used to proceed the electrochemical deposition potential of Ce by forming intermetallic compounds. It turned out that only the Ni electrode was feasible for proceeding the electrochemical reduction of Ce ions through forming an intermetallic compound. The formed compound between Ce and Ni was identified to be $CeNi_5$ by XRD and SEM analyses.

The understanding of the fundamental properties of fission products and corrosion products in FLiNaK molten salt is essential for their electrochemical separation. Through conducting chronopotentiometry tests, the diffusion coefficient of LaF_6^{3-} in FLiNaK molten salt at the temperature range of 923 to 1023 K were determined. The obtained diffusion coefficient of LaF_6^{3-} in FLiNaK molten salt is much smaller than that of La^{3+} in chloride salt. The reason for this could be that the complex ion LaF_6^{3-} is “heavier” than La^{3+} and thus the mobility is reduced. Potentiodynamic polarization measurements were also conducted. By employing a non-simplified electrode kinetics equation as the analysis method to nonlinearly fit the obtained potentiodynamic polarization curves, other kinetics parameters including exchange current density, reaction rate constant, and charge transfer coefficient of LaF_6^{3-} in FLiNaK molten salt were also obtained. Chromium is the predominant corrosion product and its fundamental properties are also studied in the present study. Considering the co-existence of Cr divalent ions and Cr trivalent ions in FLiNaK molten salt, new analytical methods for consecutive charge transfer electrochemical reaction with the presence of reactant and product were developed to do the data analysis of the cyclic voltammetry and chronopotentiometry results obtained. The obtained fundamental properties for chromium are expected to be more reliable.

Liquid bismuth is being considered for the FHR primary salt coolant clean-up to separate the fission products. The use of the bismuth requires the understanding of the

thermodynamic properties of fission products in it. Therefore, the activity coefficients of lanthanide fission products in liquid bismuth at different concentrations and temperatures were studied based on the assessed results for Gibbs energy of solution by CALPHAD method. The concentration-dependent activity and activity coefficients of K and Li in liquid bismuth at 973 K and 1023 K were also needed to be known since the activity coefficients of K and Li in liquid bismuth are necessary for identifying whether the target fission products can be preferentially deposited over K and Li when liquid bismuth is used as the electrode. As a result, an experiment was well designed. In which, through coulometric titrating K and Li into liquid bismuth and performing EMF measurement after each titration, the variations of activity and activity coefficient of K and Li in liquid bismuth with concentration in the composition range less than 20 mol% were obtained. The designed method can also be used for the activity and activity coefficient studies of actinides, fission products and other metals in liquid metal.

In order to better understand the electrochemical process, models taking into account diffusivity, temperature, scan rate, standard reaction rate, and charge transfer coefficient were developed based on MOOSE. The parameter studies performed for single-step reversible, quasi-reversible, irreversible electrochemical reactions and consecutive charge transfer electrochemical reactions will help enhance the fundamental understanding of the key features in the experimentally recorded cyclic voltammograms.

The present study supplied some unique contributions for the area of molten salt electrochemical separation. For example, the finding of the feasibility on the electrochemical separations of lanthanum and cerium in FLiNaK molten salt by inert electrode will provide a new insight for the electrochemical separations of stubborn elements. The reported effect of the existing forms of species in molten salt on the electrochemical separation will attract other investigators to focus on the study of molten salt structure. New analytical analysis methods were developed for consecutive charge transfer electrochemical reactions in the presence of reactant and product and can be used for the data analysis of cyclic voltammetry and chronopotentiometry. It will help provide more reliable data for the fundamental properties. The relationship between the activity coefficient and concentration for fission products and alkali metals in liquid bismuth at different temperatures were studied. This filled a research gap in which the activity coefficient was only reported at infinite dilution and will greatly benefit the separations of fission products when liquid bismuth electrode is used as the extraction media. Since the main purpose of this study is to do the electrochemical separations of fission products and corrosion products, it will not only facilitate the development of molten salt coolant clean-up but also the pyroprocessing of spent nuclear fuel.

References

[1] Rosenthal, M. W., P. R. Kasten, and R. B. Briggs. "Molten-salt reactors—history, status, and potential." Nuclear Applications and Technology 8.2 (1970): 107-117.
[2] Uhlíř, Jan. "Chemistry and technology of Molten Salt Reactors–history and perspectives." Journal of nuclear materials 360.1 (2007): 6-11.
[3] MacPherson, H. G. "The molten salt reactor adventure." Nuclear Science and engineering 90.4 (1985): 374-380.
[4] Serp, Jérôme, et al. "The molten salt reactor (MSR) in generation IV: overview and perspectives." Progress in Nuclear Energy 77 (2014): 308-319.
[5] LeBlanc, David. "Molten salt reactors: A new beginning for an old idea." Nuclear Engineering and design 240.6 (2010): 1644-1656.
[6] Rosenthal, Murray W. "An account of Oak Ridge National Laboratory's thirteen nuclear reactors." ORNL/TM-2009/181, August (2009).
[7] Forsberg, C.W., 2006b. Molten Salt Reactor Technology Gaps Proceedings of ICAPP.
[8] K. Furukawa, et al.Summary report: thorium molten-salt nuclear energy synergetics
J. Nucl. Sci. Technol., 27 (1990), pp. 1155-1178.
[9] U. Gat, et al.Molten Salt Reactors for Burning Dismantled Weapons Fuel Nuc. Tech., 100 (3) (1992), pp. 390-394
[10] C. Renault, M. Hron, R. Konings, et al., "The molten salt reactor (MSR) in Generation IV: overview and perspectives,"
in: Generation IV Int. Forum (GIF) Symp. (2009), pp. 191–200.
[11] A. M. Degtyarev, A. K. Kalugin, O. E. Kolyaskin, et al., "Cascade subcritical reactor for incineration of transplutonium
actinides," At. Énerg., 101, No. 2, 116–125 (2006).
[12] Holcomb, David Eugene, Fred J. Peretz, and Arthur L. Qualls. "Advanced high temperature reactor systems and economic analysis." ORNL/TM-2011/364, Oak Ridge National Laboratory (2011).
[13] Williams, David F., Louis M. Toth, and Kevin T. Clarno. Assessment of Candidate Molten Salt Coolants for the Advanced High Temperature Reactor (AHTR). United States. Department of Energy, 2006.
[14] Allen, Todd, et al. "Fluoride-Salt-Cooled High Temperature Reactor (FHR) Materials." Fuels and Components White Paper (2013).
[15] Zhang, Dingkang, and Farzad Rahnema. Integrated Approach to Fluoride High Temperature Reactor Technology and Licensing Challenges (FHR-IRP). No. 14-7829. Georgia Institute of Technology, 2019.
[16] https://doi.org/10.1002/ente.201900016
[17] Yoder Jr, Graydon L., et al. Advanced High Temperature Reactor Thermal Hydraulics Analysis and Salt Clean-up System Description. No. ORNL/TM-2014/499. Oak Ridge National Laboratory (ORNL), 2014.
[18] Gunawan, A. (2015). Thermodynamic considerations in molten salt electrolysis for rare earth metals (Doctoral dissertation, Montana Tech of The University of Montana).
[19] Ambrová, M., Jurišová, J., Danielik, V., & Gabčová, J. (2008). On the solubility of lanthanum oxide in molten alkali fluorides. Journal of Thermal Analysis and Calorimetry, 91(2), 569-573.

[20] Zhang, J., and N. Li. "Analytical solution on the transient corrosion/precipitation in non-isothermal liquid lead bismuth eutectic flow loops." Corrosion 60.4 (2004): 331-341.
[21] Koger, J. W. Alloy compatibility with LiF-BeF_2 salts containing ThF_4 and UF_4. No. ORNL-TM--4286. Oak Ridge National Lab., 1972.
[22] J. R. Engel, et al., Conceptual design characteristics of a denatured molten salt reactor with once through fueling, ORNL-TM-7207, 1980
[23] Chem. Technol. Div. Ann. Progr. Rept. (May 31, 1969), USAEC Rep. ORNL-4422 (1969)
[24] MSR Progr. Semiann. Progr. Rept. (Feb. 28, 1969), USAEC Rep. ORNL-4396 (1969).
[25] Ferris, L. M., et al. "Equilibrium distribution of actinide and lanthanide elements between molten fluoride salts and liquid bismuth solutions." Journal of Inorganic and Nuclear Chemistry 32.6 (1970): 2019-2035.
[26] Ferris, L. M., J. C. Mailen, and F. J. Smith. "Chemistry and thermodynamics of the distribution of lanthanide and actinide elements between molten LiF-BeF_2 and liquid bismuth solutions." Journal of Inorganic and Nuclear Chemistry 33.5 (1971): 1325-1335.
[27] Ferris, L. M., et al. "Distribution of lanthanide and actinide elements between liquid bismuth and molten LiCl-LiF and LiBr-LiF solutions." Journal of Inorganic and Nuclear Chemistry34.1 (1972): 313-320.
[28] Ferris, L. M., M. A. Bredig, and F. J. Smith. Equilibrium distribution of lithium and bismuth between liquid lithium--bismuth alloys and molten lithium chloride at 650 to 680$ sup 0$. Oak Ridge National Lab., TN, 1973.
[29] H. C. Savage, and J. R. Hightower, Jr. Engineering Tests of the Metal Transfer Process for Extraction of Rare-Earth Fission Products from a Molten-Salt Breeder Reactor Fuel Salt, ORNL-5176, Oak Ridge, TN, February 1977
[30] Y. I. Chang, Nucl. Technol., 88, 129–138 (1989).
[31] L. S. Chow, J. K. Basco, J. P. Ackerman, et al., Proc. GLOBAL'93, p. 1080–1085 (1993).
[32] Laidler, J. J., et al, Chemical Technology Division Annual Technical Report 1997, Argonne National Laboratory Report, Report Number ANL-98/13 (1998).
[33] D.E. Holcomb, G.F. Flanagan, G.T. Mays, W.D. Pointer, K.R. Robb, G.L. Yoder Jr, Fluoride Salt-Cooled High-Temperature Reactor Technology Development and Demonstration Roadmap, ORNL/TM-2013/401, ORNL, Oak Ridge, TN, September 2013.
[34] W. Cohen, et al, "Molten fluoride salt and liquid metal multistage extraction model", Progress in Nuclear Energy, 97 (2017): 214-219.
[35] Moriyama, Hirotake, et al. "Reductive extraction of lanthanide and actinide elements from molten LiF-BeF2 salt into liquid bismuth." Journal of Nuclear Science and Technology 21.12 (1984): 949-958.
[36] Ferris, L. M., J. C. Mailen, and F. J. Smith. "Chemistry and thermodynamics of the distribution of lanthanide and actinide elements between molten LiF-BeF_2 and liquid bismuth solutions." Journal of Inorganic and Nuclear Chemistry 33.5 (1971): 1325-1335.
[37] W. R. Grimes, Nucl. Appl. Technol. 8, 611 (1970).
[38] Ferris, L. M., et al. "Equilibrium distribution of actinide and lanthanide elements between molten fluoride salts and liquid bismuth solutions." Journal of Inorganic and Nuclear Chemistry 32.6 (1970): 2019-2035.

[39] Moriyama, Hirotake, et al. "The effect of salt composition on reductive extraction of some typical elements from molten LiF-BeF_2 salt into liquid bismuth." Nuclear Technology 62.2 (1983): 133-138.
[40] Williamson, M. A., and J. L. Willit. "Pyroprocessing flowsheets for recycling used nuclear fuel." Nuclear Engineering and Technology 43.4 (2011): 329-334.
[41] Laidler, James J., et al. "Development of pyroprocessing technology." Progress in Nuclear Energy 31.1-2 (1997): 131-140.
[42] Grimes, W. R. "Molten-salt reactor chemistry." Nuclear Applications and Technology 8.2 (1970): 137-155.
[43] Delpech, S., et al. "Reactor physic and reprocessing scheme for innovative molten salt reactor system." Journal of fluorine chemistry 130.1 (2009): 11-17.
[44] http://www.hsc-chemistry.com/
[45] Guo, Shaoqiang, et al. "Measurement of europium (III)/europium (II) couple in fluoride molten salt for redox control in a molten salt reactor concept." Journal of Nuclear Materials 496 (2017): 197-206.
[46] Chamelot, Pierre, et al. "Feasibility of the electrochemical way in molten fluorides for separating thorium and lanthanides and extracting lanthanides from the solvent." Journal of Nuclear Materials 360.1 (2007): 64-74.
[47] Y. Castrillejo, et al., Electrocehmical extraction of samarium from molten chlorides in pyrochemical processes, Electrocehimica Acta, 56, 8638-8644, 2011
[48] Ya-Lan Liu, et al., Electrochemical extraction of samarium form LiCl-KCl melt by forming Sm-Zn alloys, electrochimica Acta, 120, 369-378, 2014.
[49] M. Gibilaro, et al., Electrochemical extraction of europium from molten fluoride media, electrochimica Acta, 55, 281-287, 2009.
[50] M. Straka, L. Szatmary, Electrochemistry of selected lanthanides in FLiBe and possibilities of their recovery on reactive electrode, Procedia Chemistry 804-813, 2012.
[51] Du, Z., Wang, D., & Zhang, W. (1998). Thermodynamic assessment of the La-Ni system. Journal of alloys and compounds, 264(1-2), 209-213.
[52] Palumbo, Mauro, et al. "Thermodynamic analysis and assessment of the Ce–Ni system." Intermetallics 12.12 (2004): 1367-1372.
[53] Du, Z., Wang, D., & Zhang, W. (1999). Thermodynamic assessment of the Co–Pr, Er–Ni and Ni–Pr systems. Journal of alloys and compounds, 284(1-2), 206-212.
[54] Huang, Mianliang, R. William McCallum, and Thomas A. Lograsso. "Experimental investigation and thermodynamic modeling of the Nd–Ni system." Journal of alloys and compounds 398.1-2 (2005): 127-132.
[55] Su, X., Zhang, W., & Du, Z. (1998). A thermodynamic assessment of the Ni–Sm system. Journal of alloys and compounds, 278(1-2), 182-184.
[56] Kardellass, S., Servant, C., & Selhaoui, N. (2016). Thermodynamic description of the Ni–Yb and Ni–Eu binary systems. Journal of Thermal Analysis and Calorimetry, 125(1), 255-269.
[57] Li, Mei, and Wei Han. "Thermodynamic description of the Dy–Ni system." Calphad 33.3 (2009): 517-520.
[58] Kardellass, S., C. Servant, and N. Selhaoui. "Thermodynamic description of the holmium–nickel system." Journal of Thermal Analysis and Calorimetry 119.2 (2015): 1225-1234.

[59] Du, Zhenmin, Yunhua Xu, and Weijing Zhang. "Thermodynamic assessment of the Cu–La system." Journal of alloys and compounds 289.1-2 (1999): 88-95.
[60] Zhuang, W., et al. "Thermodynamic Evaluation of the Cu-R (R: Ce, Pr, Nd, Sm) Binary Systems." Journal of phase equilibria17.6 (1996): 508-521.
[61] Zhang, L. G., et al. "Thermodynamic assessment of Cu–Eu and Cu–Yb system." Calphad 31.2 (2007): 264-268.
[62] Zhang, L. G., et al. "Thermodynamic assessment of the Al–Cu–Gd system." Calphad 33.4 (2009): 664-672.
[63] Zhang, L. G., et al. "Thermodynamic assessment of the Cu–Dy binary system." Journal of Alloys and Compounds 470.1-2 (2009): 214-217.
[64] Wang, C. P., et al. "Thermodynamic assessments of the Ho–X (X: Cu, Mo, V) systems." Journal of Alloys and Compounds487.1-2 (2009): 173-178.
[65] Zhang, L. G., et al. "Thermodynamic assessment of the Al–Cu–Er system." Calphad 32.3 (2008): 527-534.
[66] Wang, C. P., et al. "Thermodynamic assessments of the Cu–B and Cu–Tm systems." Journal of Alloys and Compounds482.1-2 (2009): 67-72.
[67] Kim, H., Smith, N., Kumar, K., & Lichtenstein, T. (2016). Electrochemical separation of barium into liquid bismuth by controlling deposition potentials. Electrochimica Acta, 220, 237-244.
[68] Grimes, W. R. "Molten-salt reactor chemistry." Nuclear Applications and Technology 8.2 (1970): 137-155.
[69] Yamana, Hajimu, et al. "Thermodynamic properties of lanthanide metals in liquid bismuth." Journal of nuclear materials 294.3 (2001): 232-240.
[70] Gschneidner, K. A., and F. W. Calderwood. "The bismuth-rare earth systems." Bulletin of Alloy Phase Diagrams 10.4 (1989): 419-427.
[71] Castrillejo, Y., et al. "Application of electrochemical techniques in pyrochemical processes–Electrochemical behaviour of rare earths at W, Cd, Bi and Al electrodes." Journal of nuclear materials 360.1 (2007): 32-42.
[72] Kurata, Masaki, Yoshiharu Sakamura, and Tsuneo Matsui. "Thermodynamic quantities of actinides and rare earth elements in liquid bismuth and cadmium." Journal of alloys and compounds 234.1 (1996): 83-92.
[73] Zhang, J., E. A. Lahti, and E. Wu. "Thermodynamic properties of actinides and fission products in liquid bismuth." Progress in Nuclear Energy 81 (2015): 67-77.
[74] Yamana, Hajimu, Jiawei Sheng, and Osamu Shirai. "Non-monotonic systematic variation of the thermodynamic properties of lanthanide metals in liquid bismuth." Journal of nuclear materials 344.1-3 (2005): 146-151.
[75] Lebedev, VA, Effemov, M.V., Kober, V.I., 1975. In: Special Physical and Chemical Characteristics of Dilute Alloys Nauka, Moscow, pp. 96–99 (in Russian).
[76] Lebedev, V. A. "Selectivity of the liquid-metal electrodes in molten halides." Metallurgiya, Chelyabinsk 21 (1993).
[77] Sheng, Jiawei, Hajimu Yamana, and Hirotake Moriyama. "Thermodynamics of dilute solution of Gd in Bi." PhysChemComm 4.9 (2001): 40-43.
[78] Kober, V.I., Nichkov, I.F., Raspopin, S.E., Kuziminyx, V.M., 1983. In: Special Physical Characteristics of Dilute Alloys. Nauka, Moscow, pp. 132–135 (in Russian).
[79] Sheng, Jiawei, Hajimu Yamana, and Hirotake Moriyama. "Activity coefficients of Dy dissolved in liquid Bi." Journal of nuclear materials 301.2-3 (2002): 220-222.

[80] Yamana, Hajimu, Jiawei Sheng, and Osamu Shirai. "Non-monotonic systematic variation of the thermodynamic properties of lanthanide metals in liquid bismuth." Journal of nuclear materials 344.1-3 (2005): 146-151.
[81] Sheng, Jiawei. "Thermodynamic properties of dilute holmium in liquid bismuth." Journal of materials science 40.23 (2005): 6333-6336.
[82] Delahay, Paul. New Instrumental Methods in Electrochemistry: Theory, Instrumentation, and Applications to Analytical and Physical Chemistry. With a Chapter on High-frequency Methods. Interscience Publishers, 1954.
[83] Berzins, Talivaldis, and Paul Delahay. "Oscillographic polarographic waves for the reversible deposition of metals on solid electrodes." Journal of the American Chemical Society 75.3 (1953): 555-559.
[84] Wu, Evan. Integrated Study of Rare Earth Drawdown by Electrolysis for Molten Salt Recycle. Diss. The Ohio State University, 2017.
[85] Sand, Henry JS. "III. On the concentration at the electrodes in a solution, with special reference to the liberation of hydrogen by electrolysis of a mixture of copper sulphate and sulphuric acid." The London, Edinburgh, and Dublin Philosophical Magazine and Journal of Science 1.1 (1901): 45-79.
[86] Guo, Shaoqiang, Evan Wu, and Jinsuo Zhang. "Exchange current density of Gd (III)/Gd reaction in LiCl-KCl eutectic and analysis of errors caused by various methods." Electrochimica Acta 259 (2018): 253-261.
[87] A.J. Bard, L.R. Faulkner, Electrochemical Methods, Fundamental and Applications, Wiley, New York, 2001.
[88] Kaufman, Larry, and Harold Bernstein. "Computer calculation of phase diagrams. With special reference to refractory metals." (1970).
[89] Campbell, F. C. "Phase Diagram Applications." (2012).
[90] D.A. Knoll, D.E. Keyes, Journal of Computational Physics 193 (2) (2004) 357–397.
[91] Derek Gaston, Chris Newman, Glen Hansen, Damien Lebrun-Grandié, MOOSE: A parallel computational framework for coupled systems of nonlinear equations, Nuclear Engineering and Design 239 (2009) 1768–1778
[92] Ackerman, John P. Industrial & Engineering Chemistry Research 30.1 (1991): 141-145.
[93] Qiao, Huan, Toshiyuki Nohira, and Yasuhiko Ito. "Electrochemical formation of Pd–La alloy films in a LiF–NaF–KF–LaF3 melt." Journal of alloys and compounds 359.1-2 (2003): 230-235.
[94] Chesser, Ryan, Shaoqiang Guo, and Jinsuo Zhang. "Electrochemical behavior of dysprosium and lanthanum in molten LiF-NaF-KF (Flinak) salt." Annals of Nuclear Energy120 (2018): 246-252.
[95] http://www.hsc-chemistry.com/
[96] Massot, Laurent, et al. "Electrochemical study of the Eu (III)/Eu (II) system in molten fluoride media." Electrochimica Acta 54.26 (2009): 6361-6366.
[97] Masset, Patrick, et al. "Electrochemistry of uranium in molten LiCl-KCl eutectic." Journal of The Electrochemical Society152.6 (2005): A1109-A1115.
[98] http://www.egmont.com.pl/gamry/katalog/PHE200.pdf
[99] Qiao, Huan, Toshiyuki Nohira, and Yasuhiko Ito. "Electrochemical formation of Au2Na alloy and the characteristics of (Au2Na+Au) reference electrode in a LiF–NaF–KF eutectic melt." Electrochimica acta 47.28 (2002): 4543-4549.

[100] Chuchvalcova Bimova, K., et al. "Study of electrochemical separation in molten fluoride salt media." Atalante, Montpellier (France) (2008).
[101] Dracopoulos, V., Gilbert, B., & Papatheodorou, G. N. (1998). Vibrational modes and structure of lanthanide fluoride–potassium fluoride binary melts LnF_3–KF (Ln= La, Ce, Nd, Sm, Dy, Yb). Journal of the Chemical Society, Faraday Transactions, 94(17), 2601-2604.
[102] Sokol'skii, V. E., Roik, A. S., Kazimirov, V. P., Faidyuk, N. V., & Savchuk, R. N. (2012). X-ray diffraction study of the NaF-LiF-LaF3 eutectic in the liquid and solid states. Inorganic Materials, 48(4), 416-422.
[103] Beneš, O., & Konings, R. J. M. (2008). Thermodynamic evaluation of the MF–LaF_3 (M= Li, Na, K, Rb, Cs) systems. Calphad, 32(1), 121-128.
[104] Ambrová, M., Jurišová, J., & Danielik, V. (2008). Electrochemical behaviour of lanthanum fluoride in molten fluorides. Chemical Papers, 62(6), 559-565.
[105] Gonzalez, Mario, et al. "Identification, measurement, and mitigation of key impurities in LiCl-Li_2O used for direct electrolytic reduction of UO_2." Journal of Nuclear Materials510 (2018): 513-523.
[106] Saïla, Abdelkader, et al. "Electrochemical behaviour of dysprosium (III) in LiF–CaF_2 on Mo, Ni and Cu electrodes." Journal of Electroanalytical Chemistry 642.2 (2010): 150-156.
[107] Massalski, Thaddeus B., et al., eds. Binary alloy phase diagrams. Vol. 2, 2nd ed., 1990.
[108] Yoon, D., and S. Phongikaroon. "Electrochemical properties and analyses of $CeCl_3$ in LiCl-KCl eutectic salt." Journal of The Electrochemical Society 162.10 (2015): E237-E243.
[109] Chandra, Manish, et al. "Redox behaviour of cerium (III) in LiF–CaF_2 eutectic melt." Electrochimica Acta 58 (2011): 150-156.
[110] Ackerman, John P. "Chemical basis for pyrochemical reprocessing of nuclear fuel." Industrial & Engineering Chemistry Research 30.1 (1991): 141-145.
[111] Tang, Hao, and Batric Pesic. "Electrochemical behavior of LaCl3 and morphology of La deposit on molybdenum substrate in molten LiCl–KCl eutectic salt." Electrochimica Acta 119 (2014): 120-130.
[112] Samin, Adib, et al. "Estimation of key physical properties for $LaCl_3$ in molten eutectic LiCl–KCl by fitting cyclic voltammetry data to a BET-based electrode reaction kinetics model." Journal of Nuclear Materials 475 (2016): 149-155.
[113] Fabian, Cesimiro P., et al. "Experimental and simulation study of the electrode reaction mechanism of La^{3+} in LiCl-KCl eutectic molten salt." Journal of The Electrochemical Society159.4 (2012): F63-F67.
[114] Guo, Shaoqiang, Evan Wu, and Jinsuo Zhang. "Exchange current density of Gd (III)/Gd reaction in LiCl-KCl eutectic and analysis of errors caused by various methods." Electrochimica Acta 259 (2018): 253-261.
[115] Laity, Richard W., and James DE McIntyre. "Chronopotentiometric Diffusion Coefficients in Fused Salts I. Theory1a." Journal of the American Chemical Society 87.17 (1965): 3806-3812.
[116] A.J. Bard, L.R. Faulkner, Electrochemical Methods, Fundamental and Applications, Wiley, New York, 2001.

[117] Samin, Adib, et al. "Estimation of key physical properties for $LaCl_3$ in molten eutectic LiCl–KCl by fitting cyclic voltammetry data to a BET-based electrode reaction kinetics model." Journal of Nuclear Materials 475 (2016): 149-155.
[118] Wang, Yafei, Wentao Zhou, and Jinsuo Zhang. "Investigation of concentration-dependence of thermodynamic properties of lanthanum, yttrium, scandium and terbium in eutectic LiCl-KCl molten salt." Journal of Nuclear Materials 478 (2016): 61-73.
[119] Guo, Shaoqiang, Evan Wu, and Jinsuo Zhang. "Investigation of electrochemical kinetics for La (III)/La reaction in molten LiCl-KCl eutectic salt using potentiometric polarization." Journal of Nuclear Materials 510 (2018): 414-420.
[120] Guo, Shaoqiang, Evan Wu, and Jinsuo Zhang. "Exchange current density of Gd (III)/Gd reaction in LiCl-KCl eutectic and analysis of errors caused by various methods." Electrochimica Acta 259 (2018): 253-261.
[121] Ludwig, D., et al. "High temperature electrochemistry of molten fluoride salt for measurement of dissolved chromium." Corrosion Engineering, Science and Technology 46.4 (2011): 360-364.
[122] Yoko, Toshinobu, and Ronald A. Bailey. "Electrochemical Studies of Chromium in Molten LiF-NaF-KF (FLINAK)." Journal of the electrochemical society 131.11 (1984): 2590-2595.
[123] Wang, Yan Li, et al. "Effects of the oxidants H_2O and CrF_3 on the corrosion of pure metals in molten (Li, Na, K) F." Corrosion Science 103 (2016): 268-282.
[124] Wu, Wei, Shaoqiang Guo, and Jinsuo Zhang. "Electrochemical Behaviors of Cr (III) in Molten LiF-NaF-KF Eutectic." Int. J. Electrochem. Sci 13 (2018): 225-234.
[125] Berzins, Talivaldis, and Paul Delahay. "Oscillographic polarographic waves for the reversible deposition of metals on solid electrodes." Journal of the American Chemical Society75.3 (1953): 555-559.
[126] H. G. MacPherson, "Molten-salt reactor program quarterly progress report: October 1958," ORNL 2626.
[127] G. W. Mellors and S. Senderoff, Applications of Fundamental Thermodynamics to Metallurgical Processes, Gordon and Breach Science Publishers, New York, 1967
[128] Doniger, William H., and Kumar Sridharan. "Application of voltammetry for quantitative analysis of chromium in molten 2LiF-BeF_2 (FLiBe) salt." Journal of Electroanalytical Chemistry 838 (2019): 73-81.
[129] Peng, Hao, et al. "Electrochemical investigation of the stable chromium species in molten FLINAK." RSC Advances 5.94 (2015): 76689-76695.
[130] Randles, John EB. "A cathode ray polarograph. Part II.—The current-voltage curves." Transactions of the Faraday Society44 (1948): 327-338.
[131] A.J. Bard, L.R. Faulkner, Electrochemical Methods, Fundamental and Applications, Wiley, New York, 2001.
[132] Heinze, J. (1984). Cyclic voltammetry—"electrochemical spectroscopy". New analytical methods (25). Angewandte Chemie International Edition in English, 23(11), 831-847.
[133] Keightley, Angela M., et al. "Reversible cyclic voltammetry in the presence of product." Journal of Electroanalytical Chemistry 322.1-2 (1992): 25-54.
[134] Guo, Shaoqiang, et al. "Measurement of europium (III)/europium (II) couple in fluoride molten salt for redox control in a molten salt reactor concept." Journal of Nuclear Materials 496 (2017): 197-206.

[135] Laity, Richard W., and James DE McIntyre. "Chronopotentiometric Diffusion Coefficients in Fused Salts I. Theory1a." Journal of the American Chemical Society 87.17 (1965): 3806-3812.
[136] Macdonald, Digby D. "Chronopotentiometry." Transient Techniques in Electrochemistry. Springer, Boston, MA, 1977. 119-184.
[137] Testa, A. C., and W. H. Reinmuth. "Stepwise reactions in chronopotentiometry." Analytical Chemistry 33.10 (1961): 1320-1324.
[138] Wang, Jinsan, et al. "Thermodynamic assessment of the Bi–Er and the Bi–Dy systems." Thermochimica Acta 566 (2013): 44-49.
[139] Wang, Jinsan, et al. "Thermodynamic assessment of the Gd–Bi and the Ho–Bi systems." Calphad 41 (2013): 1-5.
[140] Tang, Ying, et al. "Thermodynamic Modeling of the La-B and La-Bi Systems Supported by First-Principles Calculations." Journal of Phase Equilibria and Diffusion 34.4 (2013): 297-306.
[141] Wang, S. L., et al. "Thermodynamic assessments of the Bi–Lu and Lu–Sb systems." Calphad 35.3 (2011): 421-426.
[142] Wang, C. P., et al. "Thermodynamic assessments of the Bi–Nd and Bi–Tm systems." Journal of Alloys and Compounds 502.1 (2010): 43-48.
[143] Wang, S. L., et al. "Thermodynamic Assessments of the Bi-Tb and Bi-Y Systems." Journal of phase equilibria and diffusion 32.5 (2011): 441.
[144] Redlich, Otto, and A. T. Kister. "Algebraic representation of thermodynamic properties and the classification of solutions." Industrial & Engineering Chemistry 40.2 (1948): 345-348.
[145] Zhou, Wentao, and Jinsuo Zhang. "Direct calculation of concentration-dependent activity coefficient of UCl_3 in molten LiCl-KCl." Journal of The Electrochemical Society 162.10 (2015): E199-E204.
[146] Wang, Yafei, Wentao Zhou, and Jinsuo Zhang. "Investigation of concentration-dependence of thermodynamic properties of lanthanum, yttrium, scandium and terbium in eutectic LiCl-KCl molten salt." Journal of Nuclear Materials 478 (2016): 61-73.
[147] Kaptay, George. "A new equation for the temperature dependence of the excess Gibbs energy of solution phases." Calphad 28.2 (2004): 115-124.
[148] Wang, Yafei, et al. "Thermodynamic properties of fission products (Pr, Ce, Er) in liquid bismuth by thermodynamic assessment." Journal of Nuclear Materials 495 (2017): 181-191.
[149] Raoult, Francois-Marie. "Loi générale des tensions de vapeur des dissolvants." CR Hebd, Seances Acad. Sci 104 (1887): 1430-1433.
[150] Staverman, A. J., and J. H. Van Santen. "The Entropy of Liquid Mixtures: I. The Theory of Raoult's Law." Recueil des Travaux Chimiques des Pays-Bas 60.2 (1941): 76-84.
[151] Henry, William. "Experiments on the Quantity of Gases Absorbed by Water, at Different Temperatures, and Under Different Pressures." Philosophical Transactions of the Royal Society of London 93 (1803): 29-276.
[152] Petric, A., A. D. Pelton, and M. L. Saboungi. "Thermodynamic properties of liquid K-Bi alloys by electromotive force measurements." Journal of Physics F: Metal Physics 18.7 (1988): 1473.

[153] R. Hultgren, P.D. Desai, D.T. Hawkins, M. Gleiser, K.K. Kelley, Selected Values of the Thermodynamic Properties of Binary Alloys, ASM, Metals Park, OH, 1973, pp. 421–423.
[154] Egan, J. J. "Coulometric titrations using calcium fluoride solid electrolytes to study some ionic alloys." High temperature science 19.2 (1985): 111-125.
[155] Foster, Melvin S., Scott E. Wood, and Carl E. Crouthamel. "Thermodynamics of binary alloys. I. The lithium-bismuth system." Inorganic Chemistry 3.10 (1964): 1428-1431.
[156] Demidov, A. I., and A. G. Morachevsky. "Thermodynamic Properties of Liquid Li-Bi Alloys." Elektrokhimiya 9.9 (1973): 1393-1394.
[157] Durán-Klie, Gabriela, Davide Rodrigues, and Sylvie Delpech. "Dynamic Reference Electrode development for redox potential measurements in fluoride molten salt at high temperature." Electrochimica Acta 195 (2016): 19-26.
[158] Kim, Hojong, et al. "Thermodynamic properties of calcium–bismuth alloys determined by emf measurements." Electrochimica Acta 60 (2012): 154-162.
[159] Niu, Chunju, et al. "Thermodynamic assessment of the Bi–K binary system." Thermochimica acta 528 (2012): 9-14.
[160] Samin, Adib J. "A one-dimensional stochastic approach to the study of cyclic voltammetry with adsorption effects." AIP Advances 6.5 (2016): 055101.
[161] Yoko, Toshinobu, and Ronald A. Bailey. "Electrochemical Studies of Chromium in Molten LiF-NaF-KF (FLINAK)." Journal of the electrochemical society 131.11 (1984): 2590-2595.
[162] Huang, W., Tian, L., She, C., Jiang, F., Zheng, H., Li, W., ... & Li, Q. (2014). Electrochemical behavior of europium (III)-europium (II) in LiF-NaF-KF molten salt. Electrochimica Acta, 147, 114-120.
[163] https://mooseframework.org/getting_started/installation/mint.html.
[164] Reddy, B. Prabhakara, et al. "Electrochemical studies on the redox mechanism of uranium chloride in molten LiCl–KCl eutectic." Electrochimica Acta 49.15 (2004): 2471-2478.
[165] Peng, Hao, et al. "Electrochemical investigation of the stable chromium species in molten FLINAK." RSC Advances 5.94 (2015): 76689-76695.
[166] Klingler, R. J., and J. K. Kochi. "Heterogeneous rates of electron transfer. Application of cyclic voltammetric techniques to irreversible electrochemical processes." Journal of the American Chemical Society 102.14 (1980): 4790-4798.
[167] Zhang, Jinsuo. "Parametric studies of uranium deposition and dissolution at solid electrodes." Journal of Applied Electrochemistry 44.3 (2014): 383-390.